ICRP ref: 4930-4407-4441

Annals of the ICRP

ICRP PUBLICATION XXX

Reference Organ Absorbed and Effective Dose Coefficients for Computed Tomographic Examinations

Editor-in-Chief
C.H. CLEMENT

Associate Editor
Q. FAN

Authors on behalf of ICRP
D.G. Sutton, J.T.M. Jansen, C. Lee, H. Schlattl, Y.S. Yeom, Y. Lee, N. Petoussi-Henss

PUBLISHED FOR

The International Commission on Radiological Protection

by

SAGE

Please cite this issue as 'ICRP, 20xx. Title of the publication. ICRP Publication XXX. Ann. ICRP xx(x).'

CONTENTS

REFERENCE ORGAN ABSORBED AND EFFECTIVE DOSE COEFFICIENTS FOR COMPUTED TOMOGRAPHY

ICRP PUBLICATION XXX

Approved by the Commission in MMMMM 20XX

Abstract – For many years, ICRP has produced reference dose coefficients for common diagnostic nuclear medicine procedures. Until recently ICRP has not provided reference dose coefficients for x-ray imaging procedures. However, x-ray imaging procedures make the largest contribution to human exposure to ionising radiation from artificial sources. One of the reasons for this is the well documented increase in the use of computed tomography as an imaging modality, resulting in a year-on-year increase in imaging dose per capita associated with such examinations. ICRP has recently published reference dose coefficients for common radiographic examinations, and this publication extends that work to computed tomography. The availability of ICRP reference organ and effective dose coefficients in computed tomography is expected to standardise CT dose assessments internationally and facilitate the work of national and international authorities responsible for the estimation of patient doses. It will also benefit practitioners working in the field. This publication describes the development and implementation of a virtual, representative scanner, the ICRP reference scanner, that incorporates a theoretical, non-manufacturer-specific model of Automatic Tube Current Modulation (ATCM). The reference scanner was developed using detailed data from a series of CT scanners. The ATCM implementation is based on a simple mathematical model and is provided as an educational tool / aid to optimisation only. The reference scanner was used to derive a library of dose coefficients for the adult and paediatric male (M) and female (F) ICRP reference voxel phantoms. The normalisation quantity is $CTDI_{free\text{-}in\text{-}air}$ and the body and head $CTDI_w$ to $CTDI_{free\text{-}in\text{-}air}$ coefficients are also provided. For each phantom slice, coefficients were determined for organ absorbed doses and for the coefficients of either $\sum w_T \times H_T^M$ or $\sum w_T \times H_T^F$, where H_T^M and H_T^F are the equivalent doses to the tissues or organs T, and w_T is the tissue weighting factor for target tissue. The coefficients were derived using the Monte Carlo codes MCNP 6.1 and MCNPX 2.7 and verified using the Monte Carlo code Geant4. Users can use the data themselves with a set of equations provided in the text, or they can make use of a calculator accessible via a graphical user interface that accompanies the publication. No attempt has been made to define specific clinical protocols. The scope of this publication is confined to 'conventional' CT; it does not, per se, consider technologies such as photon counting CT or spectral CT, whether using dual detectors or kV switching. The dose coefficients are not intended to be used for individual patient dosimetry.

Keywords: Computed tomography; Reference phantoms; CT scanners; Organ absorbed dose; Effective dose; Monte Carlo; ATCM

MAIN POINTS

- **ICRP has recently provided reference dose coefficients for common radiographic examinations, and this publication extends that work to computed tomography. The availability of ICRP reference organ and effective dose coefficients in CT will facilitate the work of national and international authorities responsible for estimation of patient doses and will also be of benefit to practitioners working in the field.**

- **As part of the work the Task Group has developed a virtual, representative scanner—the ICRP reference scanner—that incorporates a theoretical, non-manufacturer-specific model of Automatic Tube Current Modulation.**

- **The ICRP reference scanner has been used in Monte Carlo radiation transport simulations employing the family of ICRP reference male and female voxel computational phantoms to derive a library of dose coefficients. The dose coefficients are provided per phantom slice for the male and female newborn, 1-year-old, 5-year-old, 10-year-old, 15-year-old, and adult phantoms.**

- **All relevant data can be found in the electronic supplement accompanying this publication in the form of spreadsheets and open-source files.**

- **Users can manipulate the data themselves using the equations provided, or they can make use of a calculator accessible via a graphical user interface that accompanies the publication. Worked examples are provided to help users who wish to manipulate the data themselves.**

- **The underlying concepts and uncertainties associated with the organ and effective dose coefficients presented in this publication must always be taken into account when evaluating and reporting patient doses.**

- **This publication is not intended to be used for the purpose of individual patient dose or risk assessment.**

1. INTRODUCTION

(1) X-ray imaging procedures make the largest contribution to human exposure to ionising radiation from artificial sources. One of the reasons for this is the well documented increase in the use of computed tomography (CT) as an imaging modality resulting in a year-on-year increase in imaging dose per capita associated with CT examinations. The 2022 United Nations Scientific Committee on the Effects of Atomic Radiation (UNSCEAR) report estimates that whilst only 9.6% of global radiological procedures involve the use of CT examinations, 61.6% of the collective dose resulting from medical exposures, excluding radiotherapy, results from CT (UNSCEAR, 2022). The number of CT procedures has increased by about 80% since the 2008 UNSCEAR report and the resulting collective dose by about 70% (UNSCEAR, 2008, 2022).

(2) X-ray examinations of all types may carry an associated radiation risk that, although not large, must be considered when patients are imaged. The benefits to the patient undergoing a properly justified and optimised radiological procedure should outweigh the risk resulting from the radiation exposure. In clinical practice, the radiation dose to the patient must be managed in such a way as to be commensurate with the medical purpose. The goal is to use the appropriate dose to obtain the image quality required to achieve the desired medical objective (ICRP, 2023b). Thus, an important component of the justification and optimisation process is the availability of information on the doses that patients are receiving, together with an understanding of whether these doses are reasonable in the context of the examination being performed (ICRP, 2007a). The production of an internationally accepted and standardised tool to derive doses in computed tomography would be of great value in this process.

(3) One way to obtain information on patient doses in CT is to use metrics that are easily measurable such as Computed Tomographic Dose Index (CTDI) or Dose Length Product (DLP). However, there are many occasions in day-to-day practice in which the availability of prior estimates of doses based on simulations of the examination employing human computational phantoms (i.e. models) and computer codes simulating the transport of radiation in different media are useful. Daily decisions for justifying patient imaging exposures, or for optimising protection through selecting the most appropriate imaging technique, can require approximate estimates of dose that can be used to judge risks to health. Generic values of organ absorbed dose and effective dose provide a straightforward tool with enough information about general radiation exposure levels linked to detriment for the purpose of making these everyday decisions (ICRP, 2021). One example, as pointed out in *Publication 147* (ICRP, 2021), is that when two different x-ray imaging modalities are considered, the primary factor determining the choice will be the potential benefit to the patient, but comparison of effective or organ doses can be a secondary factor in guiding a referral test selection. Comparison between directly measured quantities in different modalities is meaningless; for example, kerma-area product (KAP) as used in radiography and fluoroscopy cannot be compared to DLP, routinely used in CT.

(4) Unintended exposures and overexposures of patients in CT examinations can be assessed using effective and organ doses derived from simulations employing numerical methods. These can provide sufficient information for the incident investigation and report and inform decisions on requirements for more detailed assessments (ICRP, 2021).

(5) Before a research proposal involving the use of ionising radiation is approved, an evaluation of possible detriment for the individuals involved must be made and recorded. The availability of a standardised approach to the estimation of patient organ and effective doses will ensure that a consistent approach can be taken to dose estimation, bearing in mind of course that when considering potential radiation-related risks in research subjects, allowance should be made for age, sex, and health status.

(6) There are growing demands from patients, families, medical professionals, and relevant regulatory agencies to document patient-specific exposures to diagnostic medical imaging procedures (e.g. Council of the European Union, 2014; Ukkola et al., 2016; IAEA, 2018). Ethical and professional considerations around accountability, transparency, and patient-centredness emphasise the importance of these requirements (ICRP, 2024c). For over 40 years there have been several efforts by different organisations to estimate patient doses in CT. As a result, various tables and software tools have been developed by different authors. These are based on extensive libraries of pre-calculated dose coefficients generated using computational phantoms and Monte Carlo radiation transport codes. Lee (2021) provides some examples of such software tools, which are summarised in Table 1.1 together with some more recent developments. Note that this list is not exhaustive. A standardised methodology, however, will aid national and international assessments of such doses.

(7) In the early 1990s, coefficients relating organ doses to a measurement of air kerma free-in-air on the scanner axis of rotation were developed at Helmholtz Zentrum München (formerly GSF, National Research Centre for Environment and Health) for the male and female adult phantoms Adam and Eva (Kramer et al., 1982) and three radiation qualities (Zankl et al., 1991, 1992). These first data sets were later extended by including paediatric sets based on voxel phantoms of a Baby and a Child (Zankl, 2010). The software tools WinDose (Kalender et al., 1999b) and CTexpo (Stamm and Nagel, 2002) are based on these datasets.

(8) In the same period the National Radiological Protection Board (NRPB), now known as the United Kingdom Health Security Agency (UKHSA), conducted a UK wide survey that provided the first systematic assessment of typical organ and effective doses from CT (Shrimpton et al., 1991). Dosimetry for this study was based on normalised organ doses (relative to free-in-air axial doses) derived from Monte Carlo calculations that modelled 27 types of CT scanner then in common use, using modified Cristy and Eckerman (1987) mathematical MIRD-type stylised phantoms (Jones and Wall, 1985). The dose coefficients data were published electronically as software report NRPB-SR250 (Jones and Shrimpton, 1993). Le Heron (1993) produced a software tool, CTDOSE, that could be used to interrogate the datasets. Shrimpton and Edyvean (1998) used the data to show variations of up to a factor of 3 between normalised values of effective dose for similar standard examinations over the range of scanners modelled, reflecting differences in design and therefore reinforcing the need for accurate modelling. Khursheed et al. (2002) extended the work to paediatric phantoms, using the Cristy and Eckerman (1987) paediatric phantoms with some modifications.

(9) The datasets were subsequently used as the platform on which the widely used calculation program IMPACT-CT was developed by the UK ImPACT (Image Performance of CT scanners) group from 2000 onwards (http://www.impactscan.org/ctdosimetry.htm). The tool is spreadsheet-based. In order to allow convenient estimates of dose for more modern CT scanners not specifically included in NRPB-SR250, the ImPACT group devised a method for matching contemporary scanners to the old data sets and continued to add scanners until the last release of the software in 2011 (ImpaCT, 2011). It is therefore possible for users to match their own scanner to the data sets, although this is not a trivial task. The ImPACT software can only be used in conjunction with the NRPB datasets available at ImPACT (2011) but continues to be widely used. Jansen and Shrimpton (2016) report that whilst there have been several more recent Monte Carlo simulations for a few specific CT scanner models, report NRPB-SR250 (Jones and Shrimpton, 1993) remains the most comprehensive, covering a whole range of scanners and exposure conditions and widely used set of normalised organ doses for CT, although these data stem from the early 1990s.

(10) In 2022 the UK Chemicals and Environmental Hazards Directorate of the UKHSA undertook a new series of Monte Carlo simulations to provide organ dose coefficients for a range of contemporary CT scanners to reflect changes in technology, and also ICRP

recommendations concerning the use of the reference computational adult male and adult female phantoms (ICRP, 2009). A series of 102 new Monte Carlo simulations were performed covering the range of operating conditions for 12 contemporary models of CT scanners from 4 manufacturers (Jansen et al., 2022).

(11) Another tool currently in use is the NCICT—National Cancer Institute dosimetry system for CT (https://github.com/ncidosimetry/ncidosetools). This tool was introduced by Lee et al. (2015). The developers used the ICRP reference paediatric and adult phantoms combined with the Monte Carlo simulation of a Siemens Sensation 16 CT scanner to establish comprehensive organ dose coefficients, expressed as organ absorbed dose per unit volumetric CT Dose Index ($CTDI_{vol}$) (mGy mGy^{-1}). NCICT is based on two assumptions. The first assumption is that organ doses calculated for one type of CT scanner can be converted to organ doses for another type of scanner using the ratio of the $CTDI_{vol}$ of the two scanners. Turner et al. (2010) were the first to validate this assumption and showed its feasibility. The second assumption is that organ doses in helical mode can be estimated by summing up the contributions from axial slices. Whereas the first version of the software employed reference phantoms only, NCICT 2.0 (Lee et al., 2022) implements a library of 351 paediatric and adult hybrid phantoms of non-reference individuals (Geyer et al., 2014) with a range of height and weight. NCICT 3.0 adds phantoms of the pregnant patient.

(12) The software CTVoxDos uses the results of Schlattl et al. (2010, 2012) in a free, standalone Windows and Linux-based software and is available upon request from the Federal Office for Radiation Protection in Germany, where it is used extensively for regulatory purposes. It employs dose coefficients calculated with Monte Carlo methods for the ICRP reference adult male and female phantoms (ICRP, 2009), 4 adult non-reference phantoms (3 female and 1 male) (Zankl, 2010), a non-reference female phantom at the 24th week of pregnancy (Becker et al., 2008), and 3 paediatric non-reference-phantoms (8 weeks, 7 and 8 years) (Zankl, 2010). The reference scanner used to calculate dose coefficients was a Siemens Sensation 16.

(13) VirtualDoseCT is a commercial simulation web-based software (https://www.virtualphantoms.com/our-products/virtualdose/) for estimating patient organ doses for pre-defined standard and custom scan ranges for selectable kV, collimation, and beam shaping filters. The phantoms used in the product include the University of Florida/National Cancer Institute (UF/NCI) paediatric hybrid phantoms of 0-, 1-, 5-, 10-, 15-year-old, male, female (Lee et al., 2007; Lee et al., 2010); and a large number of adult phantoms developed at the Rensselaer Polytechnic Institute, including reference adults (Zhang et al., 2009; Na et al., 2010), adults of various body sizes (Ding et al., 2012, overweight and obese adults), and pregnant patients at three gestational stages (Xu et al., 2007).

(14) Other CT dose evaluation programs include the WAZA-ARIv2 (Ban et al., 2011; Takahashi et al., 2015) software which is a web-based system to calculate dose from CT by entering information such as the model of CT scanner, the scanning range, the age, body shape, and gender of the patient. It is based on Monte Carlo calculations on the University of Florida paediatric reference voxel phantoms (Lee et al., 2007; Lee et al., 2010) and the Japanese adult reference voxel phantoms (Sato et al., 2007).

(15) MIRDct is an organ level dosimetry excel-based software tool released in 2025 (Ocampo Ramos et al., 2026), developed as part of the MIRDsoft.org community software project. It is based on dose coefficients pre-calculated with Monte Carlo methods and the mesh format of the ICRP reference adult and paediatric phantoms (ICRP, 2020a, 2024a). The reference scanner used to calculate dose coefficients was a Canon Aquilion One Genesis scanner. Organ absorbed dose estimation and other metrics are calculated based on user selection appropriate input. Additionally, as an optional output, the software calculates risk evaluation quantities such as detriment weighted dose, lifetime attributable risk, and risk index.

(16) Recent work also includes the estimation of CT doses to Chinese reference paediatric phantoms using the GE LightSpeed 16 CT scanner (Ma et al., 2021). Further recent efforts include deep learning-guided approaches to generate voxel-based absorbed dose maps from whole-body CT acquisitions of individual patients (Maier et al., 2022; Tzanis and Damilakis, 2022; Salimi et al., 2023; Berris et al., 2024).

(17) Despite the availability of a large selection of tools that can be used for evaluating organ doses in computed tomography, no single internationally accepted methodology exists for estimating organ or effective doses in CT. Such a methodology would improve the comparability of doses reported in national and international surveys. For example, comparison between the results of the National Council on Radiation Protection and Measurements (NCRP) in the US presented in report 184 and the UK Health Security Agency (UKHSA, then PHE) survey of UK doses suggests that effective doses from CT examinations in the UK are higher than those in the US whilst in fact UK DLPs are lower than those in the US (Hart et al., 2010; NCRP, 2019). This apparent contradiction arises because NCRP used hermaphrodite type stylised phantoms to generate their results whilst UKHSA used the ICRP reference voxel phantom suite. Were a standardised approach to be adopted, such contradictions would not arise, and like-for-like comparisons could be made. ICRP has noted that there are differences of up to 25% in some data caused by the use of different phantoms and dose coefficients (ICRP, 2010, 2021).

(18) For many years, ICRP has produced reference dose coefficients for common diagnostic nuclear medicine procedures (ICRP, 1987, 1991b, 1998, 2015b). Until recently ICRP has not provided reference dose coefficients for x-ray imaging procedures and consequently different methodologies have been used to convert measurements to estimates of effective dose or some surrogate of effective dose. These calculations necessarily rely on disparate published data based on the use of phantoms that are not in alignment with the most recent ICRP reference phantoms. In addition, different computational methods for radiation transport have been used to report organ doses from which the effective dose is computed. In 2019, ICRP established Task Group 113 to provide dose coefficients for diagnostic paediatric and adult radiography, paediatric fluoroscopy, adult interventional fluoroscopic procedures, and CT imaging. To date ICRP has now provided reference dose coefficients for common radiographic examinations (ICRP, 2025), and this publication extends that work to computed tomography. The availability of ICRP reference organ and effective dose coefficients in CT will facilitate the work of national and international authorities responsible for such calculations.

(19) In recent years a range of dose coefficients using the ICRP reference voxel computational phantoms (or models) have become available (ICRP, 2010, 2013, 2015a, 2016a); ICRP (2017); (ICRP, 2019); ICRP (2020c); (ICRP, 2020b, 2022, 2023a); ICRP (2024b); (ICRP, 2025). These voxel models, constructed with high resolution medical images, present a significant advance towards more realistic representation of the human body. Previous studies have shown that, for some examinations, differences do occur between the different types of models (voxel or stylised) and can be attributed to the different amount of shielding of an organ, depending on the topology of these organs (Zankl et al., 1989; Zankl et al., 2002; ICRP, 2010). Computations of dose coefficients for routine examinations have shown significant differences for individual organs between the ICRP reference computational phantoms and the MIRD-type reference models used previously, and also between different voxel models—see, for example, Petoussi-Henss et al. (2006). Moreover, Lee et al. (2005, 2013) compared organ doses for paediatric CT examinations with voxel and stylised phantoms and found significant dose discrepancies in some organs, especially small and irregularly shaped ones such as thyroid and stomach. Voxel phantoms yield more accurate doses, especially in small organs whereas stylised phantoms may underestimate dose in regions near

bone or lung interfaces; authors concluded that dose differences between phantom types could reach up to 30% in some organs.

(20) This publication describes the ICRP approach to providing organ absorbed and effective dose coefficients for CT imaging. Note that the scope of this publication is confined to 'conventional' CT; it does not consider technologies such as photon counting CT or spectral CT, whether using dual detectors or kV switching. The coefficients have been produced for the adult male and female ICRP reference voxel phantoms (ICRP, 2009) and the suite of ICRP reference paediatric voxel phantoms (ICRP, 2020b) . The phantoms are briefly described in Section 2 of the companion publication to this publication on dose coefficients for radiographic imaging (ICRP, 2025).

(21) Confusion might arise because ICRP has also developed in parallel the next generation of reference phantoms, the mesh-type reference phantoms, based on the male and female voxel reference phantoms. These were introduced in *Publication 145* (ICRP, 2020a) for the reference adults and in *Publication 156* for the reference paediatric ages (ICRP, 2024a). The mesh-type phantoms will be used for future calculations of ICRP reference dose coefficients. Within the framework of CT dosimetry, the use of the mesh phantoms is not expected to result in significantly different dose coefficients from those estimated using the voxel phantoms.

(22) Rather than develop a tool that is specific to any one CT scanner or to a pre-determined set of scanners, as is the case with, for example, the UK Impact CT calculation tool (ImpaCT, 2011), we have developed a virtual, representative scanner, referred to hereafter as the ICRP reference scanner. The ICRP reference scanner is based on the characteristics of 13 CT scanners (and 102 different operating conditions) simulated using the approach described by Jansen and Shrimpton (2016). The ICRP reference scanner is used as the basis for the estimates of organ absorbed and effective doses, for all adult and paediatric phantoms across a range of tube voltages. For simplicity in the following, organ absorbed doses will be referred as organ doses. The development of the ICRP reference scanner is described in Section 3 of this publication. The underlying assumptions are similar to those used in NCICT, CTVoxDos, and MIRDct, and are as outlined in Paragraph (11) above. As with these tools, the ICRP reference scanner is only valid with current technologies. Its validity as a tool is further discussed in Section 5 of this publication. The detail of the Monte Carlo photon transport calculations used to determine organ and effective dose coefficients is presented in Section 3 of this publication.

(23) Given the widespread use of Automatic Tube Current Modulation (ATCM) in clinical practice, we have developed a theoretical ATCM model to allow for tube current modulation along the z-axis or height of the phantom and total tube current modulation around the height, z, and angle, φ. The z-axis modulation can be simulated by applying different weighting factors along the slices of the phantom. The angular modulation can be approximated by using a cosine transformed tube current for each phantom slice. The total modulation can then be represented by combining the z-axis modulation and the angular modulation for each slice, using appropriate weighting factors. The dose coefficients resulting from this model should not be taken as being representative of any manufacturer or scanner. They should be considered as being for educational purposes only and will give some idea of the impact on organ and effective doses when ATCM techniques are employed. The development of the ATCM model is described in Section 4 of this publication.

(24) Effective dose, E, is defined in *Publication 103* (ICRP, 2007b) using the equation:

$$E = \sum_{\mathrm{T}} w_{\mathrm{T}} \left[\frac{H_{\mathrm{T}}^{\mathrm{F}} + H_{\mathrm{T}}^{\mathrm{M}}}{2}\right], \tag{1.1}$$

where $H_{\mathrm{T}}^{\mathrm{M}}$ and $H_{\mathrm{T}}^{\mathrm{F}}$ are the equivalent doses to the tissues or organs T of the Reference Male and Female, respectively, and w_{T} is the tissue weighting factor for target tissue T, with $\sum w_{\mathrm{T}} = 1$. Effective dose is thus a sex-averaged quantity. This definition is valid for all ICRP reference ages. This publication provides organ absorbed dose coefficients for both male and female

phantoms. It also provides, for each examination, a value of the coefficient for either $\sum_T w_T \times H_T^M$ or $\sum_T w_T \times H_T^F$, depending on whether the examination is performed on the male or female phantom. The effective dose coefficient for an examination can be obtained by taking the average of the two. For ease of reproduction and to avoid possible confusion, the two quantities are given the nomenclature $E_{103,\#\#M}$ or, $E_{103,\#\#F}$ where ## refers to the age of the phantom being used and M or F signify male or female. For example, $E_{103,AM}$ refers to the coefficient of the quantity $\sum_T w_T \times H_T^M$ resulting from an examination on an adult male phantom and $E_{103,01F}$ refers to the coefficient of the quantity $\sum_T w_T \times H_T^F$ resulting from an examination on a 1-year-old female phantom. The '103' indicates that for all ages and respective sums, the organ and tissue weighting factors of *Publication 103* have been used which are sex and age averaged.

(25) The dose coefficients of this publication were calculated for the ICRP reference scanner, using the reference phantoms of reference ages (newborn, 1-, 5-, 10-, 15-year-old, and adult) (ICRP, 1995), in accordance with the methodology and definitions of *Publication 103* (ICRP, 2007b). Therefore, these coefficients are termed 'reference dose coefficients', refer to the reference persons and should not be used for individual patient dosimetry.

(26) The intended audience for the publication includes all those who have an interest in patient dosimetry and optimisation, such as national authorities responsible for dose calculations, medical physicists, research scientists, radiologists, radiographers, and other radiological practitioners.

(27) Results from the ICRP scanner can be accessed using a purpose designed graphical user interface (GUI)-based calculator hosted at https://icrpct-temp.ncidosetools.com/ (current location). The calculator is described in Section 6 of this publication. All coefficients are also provided in the electronic annex to this publication, as described in Section 5 and Annex D.

Table 1.1. List of CT Tools currently available as per 2025. The list is an extended version of Lee (2021) and might not be exhaustive. Programs are listed in alphabetical order.

Program name	Phantoms used				User interface platforms	Availability	Reference
	Reference, paediatric	Reference, adult	Non-reference	Pregnant patient, reference			
CT-Expo		GSF stylised ADAM, EVA (Kramer et al., 1982)	GSF** voxel, 8-wk, 7-year-old (Zankl, 2010)	–	Standalone Excel	Commercial	(Stamm and Nagel, 2002)
CTVoxDos		ICRP adult voxel (ICRP 2009)	GSF voxel Irene, Donna, Helga, Visible Human (Zankl, 2010) GSF voxel 8-wk, 7-year, 8-year-old (Zankl, 2010)	(Becker et al., 2008)	Standalone Windows, Linux	Free	(Schlattl et al., 2010; Schlattl et al., 2012)
DoseWatch		XCAT§ hybrid (n = 150)			PACS#-embedded	Commercial	(GEHealthcare.)
ImPACT	–	(Jones and Wall, 1985)	–	–	Standalone Excel	Free	(ImpaCT, 2011) (NRPB-SR250, 1993, dataset) https://www.ukhsa-protectionservices.org.uk/mdg/patientdosimetry/patientdoseestimationtool/
ImpactDose	ORNL* stylised 0-, 1-, 5-, 10-, 15-year-old, male, female (Cristy and Eckerman, 1987)	ORNL stylised male, female (Snyder et al., 1969); ICRP voxel male, female (ICRP, 2009)	–	–	Standalone Windows	Commercial	(ImpaCT, 2011)
MIRDct	ICRP† mesh 0-, 1-, 5-, 10-, 15-year-old, male, female (ICRP, 2024a)	ICRP male, female			Standalone Windows Excel	Free	https://mirdsoft.org/mirdct-2 (Ocampo Ramos et al., 2026)

Program name	Phantoms used				User interface platforms	Availability	Reference
	Reference, paediatric	Reference, adult	Non-reference	Pregnant patient, reference			
NCICT	ICRP† voxel 0-, 1-, 5-, 10-, 15-year-old, male, female (ICRP, 2020b)	ICRP male, female (ICRP, 2009)	NCI†† hybrid paediatric and adult (n = 351)(Geyer et al., 2014)	UF‡ hybrid (n = 8)	Standalone Windows, Mac, Linux	Free	(Lee et al., 2015; Lee et al., 2022)
Radimetrics	ORNL stylised 0-, 1-, 5-, 10-, 15-year-old, male, female (Cristy and Eckerman, 1987)	ORNL stylised male, female (Snyder et al., 1969)	–	ORNL stylised (n = 3)	PACS-embedded	Commercial	(Peng et al., 2020)
SINFONIA			Patient specific CT images, AI tools				http://idose.med.uoc.gr/links (Damilakis and Stratakis, 2024)
VirtualDose CT	UF‡ hybrid 0-, 1-, 5-, 10-, 15-year-old, male, female (Lee et al., 2007; Lee et al., 2010)	RPI¶ hybrid male, female (Zhang et al., 2009; Na et al., 2010)	RPI hybrid adult (n = 10) (Ding et al., 2012)	RPI hybrid (n = 3) (Xu et al., 2007)	Web application https://www.virtualphantoms.com/our-products/virtualdose/	Commercial	(Ding et al., 2015)
WAZA-ARIv2	UF reference voxel 0-, 1-, 5-, 10-, 15-year-old, male and female (Lee et al., 2007; Lee et al., 2010)	Japanese reference voxel male, female (Sato et al., 2007)	Adult voxel, male, female Thin, fat (Sato et al., 2007)		Web application https://waza-ari.nirs.qst.go.jp/en/index.html		(Ban et al., 2011; Takahashi et al., 2015)
WinDose	–	GSF stylised ADAM, EVA (Kramer et al., 1982)	–	–	Windows, Mac, Linux	Commercial	(Kalender et al., 1999b)

*Oak Ridge National Laboratory.
†International Commission on Radiological Protection.
‡University of Florida.

[§]eXtended CArdiac-Torso. From the website, it is not disclosed how many phantoms are included in different phantom categories.
[¶]Rensselaer Polytechnic Institute.
[**]GSF, National Research Center for Environment and Health (currently Helmholtz Zentrum München).
[††]National Cancer Institute.
[#]Picture Archiving and Communication System.

2. THE ICRP REFERENCE PHANTOMS

2.1. Adult and paediatric reference computational phantoms

(28) In this publication, reference dose coefficients for computed tomography (CT) exposures were calculated using the series of the ICRP reference computational phantoms (or models) for adults released via *Publication 110* (ICRP, 2009) and children (0-, 1-, 5-, 10-, and 15-year-old) released via *Publication 143* (ICRP, 2020b). The ICRP-110 and ICRP-143 reference phantoms were adopted by the Commission following the 2007 General Recommendations (ICRP (2007b) which required that the computation of ICRP reference dose coefficients for both external and internal exposures should be performed using sex- and age-dependent reference computational phantoms developed by ICRP. These reference phantoms are voxel models constructed based on CT data of real individuals, thereby representing the human anatomy much more realistically than the legacy stylised-type (or mathematical) computational phantoms whose shape of the body and organs/tissues is described using combination of quadric equations such as cylinder and ellipsoid (Snyder et al. (1969); (Snyder et al., 1978; Kramer et al., 1982; Cristy and Eckerman, 1987). It should be noted that prior to the 2007 General Recommendations, various stylised phantoms had been used for the computation of the previous reference dose coefficients. The adult and paediatric reference voxel phantoms are illustrated in Fig. 2.1.

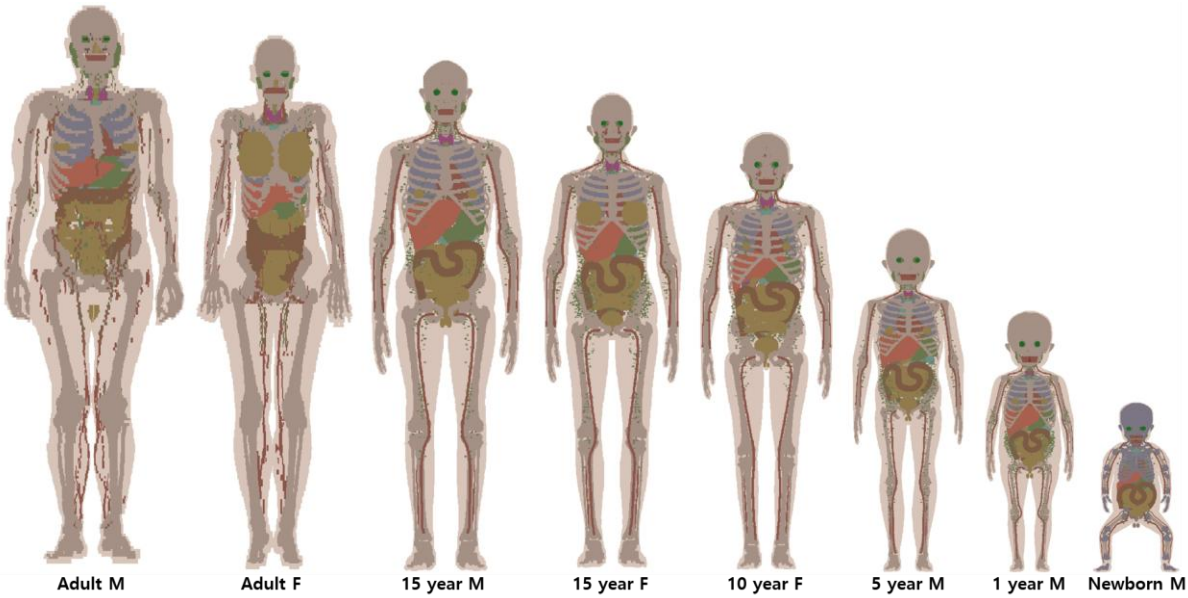

Fig. 2.1. Series of adult and paediatric reference voxel phantoms of *Publications 110* (ICRP, 2009) and *Publication 143* (ICRP, 2020b). The newborn, 1-, 5-, and 10-year-old phantoms are illustrated only for males but they are anatomically identical with the female phantoms, with the exception of the gonads and urinary bladder. M, male; F, female.

(29) The ICRP-110 adult reference phantoms were constructed by modifying the voxel models 'Golem' and 'Laura' (Zankl and Wittmann, 2001; Zankl et al., 2005) of two individuals whose standing height and body mass closely resembled the reference data given in *Publication 89* (ICRP, 2002) on the reference adult male and reference adult female. The ICRP-143 paediatric reference phantoms were derived from the voxelised version of the hybrid phantom series developed originally at the University of Florida (UF) and later in collaboration with the

National Cancer Institute (NCI)—known as the UF/NCI phantom series (Lee et al., 2010). The ICRP-110 and ICRP-143 reference phantoms were matched to *Publication* 89 (ICRP, 2002) reference values for standing heights and body masses shown in Table 2.1. The organ/tissue masses of the reference phantoms were also adjusted to the reference data in *Publication* 89 with high precision, without significantly altering their realistic anatomy. There are 136 individually identified structures in each phantom, and 53 different tissue compositions have been assigned to them. The various tissue compositions reflect both the elemental composition of the tissue parenchyma (ICRU, 1992) and each organ's blood content (ICRP, 2002) (i.e. organ composition inclusive of blood). The phantoms contain all target regions relevant to the assessment of human exposure to ionising radiation for radiological protection purposes, including all tissues and organs that contribute to effective dose, as defined in *Publication 103* (ICRP, 2007b). Table 2.2 shows the voxel resolution, array size, and matrix size (total number of voxels) for each of the adult and paediatric reference phantoms.

(30) Since the voxels have a size of the order of mm^3 (as shown in Table 2.2) some very small source and target regions of the phantoms cannot be explicitly represented. In the skeleton, for example, the target tissues of interest are the haematopoietically active bone marrow cells located within the marrow cavities of spongiosa, as well as the endosteal layer lining the surfaces of the bone trabeculae and the inner surfaces of the medullary cavities of the long bones (currently assumed to be 50 μm thick). Due to their small dimensions, these two target tissues are incorporated as homogeneous constituents of spongiosa within the reference phantoms. At lower energies of photons and neutrons, secondary charged-particle equilibrium is not fully established in these tissue regions over certain energy ranges. Consequently, more refined techniques for accounting for these effects in skeletal dosimetry are used as described in detail in *Publications 116*, *153*, and *163* (ICRP, 2010, 2022, 2025). These techniques are based on work of Hough et al. (2011), Johnson et al. (2011), and Pafundi (2009).

(31) Following the 2007 General Recommendations (ICRP, 2007b), the ICRP reference voxel phantoms have been used for the computation of an entirely new generation of reference dose coefficients for external (ICRP, 2010, 2013); ICRP (2020c); (ICRP, 2025) and internal exposures (ICRP, 2015a, 2016a, b); ICRP (2017, 2019, 2022, 2024b) and this process is still ongoing.

Table 2.1. Reference values for standing height and body mass for the ICRP reference individuals (ICRP, 2002).

	Height (cm)		Mass (kg)	
	Male	Female	Male	Female
Newborn	51	51	3.5	3.5
1-year-old	76	76	10	10
5-year-old	109	109	19	19
10-year-old	138	138	32	32
15-year-old	167	161	56	53
Adult	176	163	73	60

Table 2.2. Voxel resolution, array size, and matrix size (total number of voxels) for each of the ICRP adult and paediatric reference phantom series.

	Voxel resolution (mm)			Array size			Matrix size
Phantom	x	y	z	x	y	z	(million)
Newborn, male and female	0.663	0.663	0.663	345	211	716	52.1
1-year-old, male and female	0.663	0.663	1.400	393	248	546	53.2
5-year-old, male and female	0.850	0.850	1.928	419	230	572	55.1
10-year-old, male and female	0.990	0.990	2.425	419	226	576	54.5
15-year-old, male	1.250	1.250	2.832	407	225	586	53.7
15-year-old, female	1.200	1.100	2.828	401	236	571	54.0
Adult, male	2.137	2.137	8.000	254	127	222	7.2
Adult, female	1.775	1.775	4.840	299	137	348	14.3

2.2. Phantom modification for arm removal

(32) The adult and paediatric reference phantoms were modified to consider the typical posture of patients during CT scans in the Monte Carlo dose calculations. To achieve better quality of acquired CT images, patients generally raise their arms for CT scans of a torso region but lower the arms for CT scans of a head region. However, the adult and paediatric reference phantoms have their arms alongside the body and it is not technically easy to move the arms due to the low deformability of the voxel geometry (Kainz et al., 2019). Following the practical approach commonly used to resolve the issue (Lee et al., 2022; ICRP, 2025), for the calculations presented in this publication, the arms of the reference phantoms were removed noting that the shoulder tissues remain in order to simulate the arms being held in front of the chest or up above the chest (see Fig. 2.2). The tissues of the arms involved are skin, adipose tissue, muscle, lymph nodes, blood, cartilage, and bones. This approach was also applied for the computation of the reference dose coefficients for radiography examinations (ICRP, 2025). Studies of organ dose coefficients due to CT examinations by Jansen et al. (2022) revealed that the presence or absence of the arms resulted in a deviation of up to 10%, except for the region of the hand to lower arm and near the wrist. It should be noted that for calculating the respective dose coefficients, the original masses of all organs of the phantoms were used, i.e. inclusive of arms. This is to allow for the fact that the arms of the phantom, although removed for the Monte Carlo simulations, are in reality present and the risk, for example, of the skin, is associated with the tissue weighting factor, w_T, which corresponds to the whole organ, i.e. the skin over the whole body.

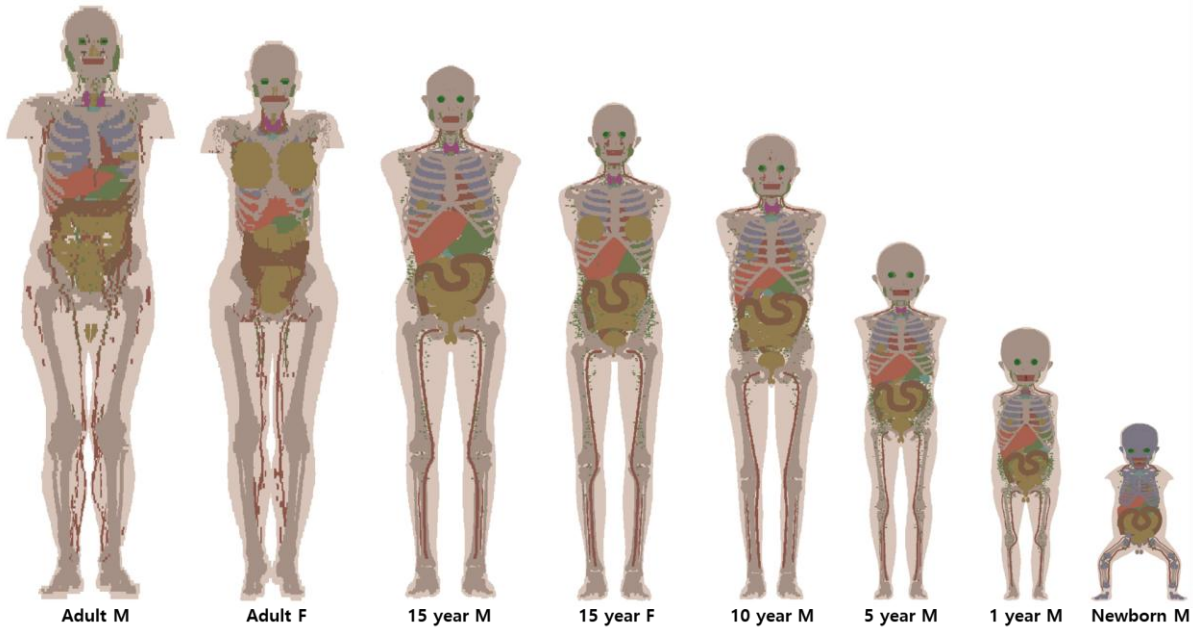

Fig. 2.2. Series of the adult and paediatric reference voxel phantoms with their arms removed. For the newborn, 1-,5-, and 10-year-old, only the male phantoms are shown. M, male; F, female.

3. DEVELOPMENT OF THE ICRP REFERENCE SCANNER AND DETERMINATION OF ORGAN ABSORBED DOSES

3.1. Overview

(33) The aim of the work described in this Section was to simulate a virtual CT scanner that can be used in Monte Carlo calculations to approximate the dosimetric behaviour of modern scanners without being specific to the design of any one manufacturer.

(34) This scanner, referred to in this publication as the 'ICRP reference scanner' has been developed using detailed data from a series of CT scanners as described by Jansen et al. (2022). Because the precise detail of each of the scanners used was subject to a Non-Disclosure Agreement (NDA), all calculations described in the development of the ICRP reference scanner were performed by one of the authors of this publication who was authorised under the agreement.

(35) To derive the characteristics of the ICRP reference scanner, a four-step process was adopted:

- *Geometric parameters:* In the first step a representative focus-to-isocentre (centre of rotation) distance was chosen from the set of CT scanners, along with a convenient focus to beam shaping filter distance.
- *Dose profiles:* Secondly, for each CT scanner, a dose profile was calculated along the axis perpendicular to the rotation axis and perpendicular to the central beam axis, through the isocentre, with the source in a fixed position (profile axis, see Fig. 3.1). These dose profiles were then averaged to produce an ICRP representative dose profile.
- *Beam shaping filters:* In the third step aluminium was chosen as the beam shaping filter material for the ICRP reference scanner since it was not possible to use any proprietary information about individual CT scanners. The averaged dose profile was used to derive Head and Body beam shaping filters for the ICRP reference scanner.
- *Homogenous x-ray filter:* Finally, aluminium was selected as the homogeneous x-ray filter material for the ICRP reference scanner. For each of the simulated scanners, the ratio of central dose to the free-in-air dose ($CTDI_{centre,32}$ / $CTDI_{free\text{-}in\text{-}air}$) was determined at 120 kV. Note that '32' indicates the CT cylindrical dosimetry phantom with a 32 cm diameter. The same procedure was applied to the ICRP reference scanner using theoretical spectra with different beam qualities generated at 120 kV. Interpolation was used to derive the amount of filtration that resulted in the best match for ($CTDI_{centre,32}$ / $CTDI_{free\text{-}in\text{-}air}$). All four steps are described in further detail below.

(36) Using the ICRP reference scanner, organ dose calculations were performed for the ICRP adult male and female reference phantoms (ICRP, 2009).

(37) Validation was carried out by comparing the dose coefficients for the adult phantoms determined using the ICRP reference scanner with coefficients calculated using the individual CT scanner models.

(38) Finally, organ doses dose coefficients for the suite of ICRP paediatric phantoms were generated by a different dose calculation group using a different simulation method applied to the ICRP reference scanner.

3.2. Scanners used in the derivation of the ICRP reference scanner

(39) Table 3.1 lists the CT scanner set used to derive the ICRP reference scanner. It includes manufacturer and CT model name as well as the operating conditions applied (tube voltage in kV, beam shaping filter type, and fan beam name). Details of these CT scanners were provided to a member of the Task Group by the manufacturers under a Non-Disclosure Agreement. In total 13 CT scanner models from 4 manufacturers were included, resulting in a total of 102 CT distinct scanner operating conditions being modelled.

3.3. Derivation of focus to isocentre distance

(40) The focus to isocentre distance for the ICRP reference scanner was derived by considering the corresponding distances for all the CT scanner models and selecting a representative rounding average distance that lay within one standard deviation of the whole distribution. This ensured that the focus to isocentre distance of the ICRP reference scanner was constrained to be within the main cluster of values for the scanners listed in Table 3.1 while avoiding an unjustifiable precision that would arise from quoting a strict numerical average. The focus to isocentre distance was determined to be 57 cm.

3.4. Monte Carlo simulations to develop the beam shaping filters for the ICRP reference scanner

(41) For each of the scanners listed in Table 3.1, the Monte Carlo N-Particle code MCNP6.1 (Pelowitz, 2013) was used as radiation transport program to simulate the dose profile perpendicular to the central beam axis and perpendicular to the CT scanner rotation axis and through the isocentre (see Fig. 3.1). These dose profiles were used to derive the beam shaping filters for the ICRP reference scanner as outlined below. The ICRP reference scanner has two beam shaping filters, Body and Head. Thus, for each of the scanners shown in Table 3.1, the filter that was the most appropriate for each of these designations was selected. If the CT scanner model being used had no selectable beam shaping filter, the filter provided on the scanner was employed in the derivation of the ICRP reference scanner filters. Note that each filter in the ICRP reference scanner includes data from effectively 13 different CT models since the Siemens Definition scanner has both Full and Small fan beams (Table 3.1) and can therefore be considered to represent two devices.

Table 3.1. CT scanners and their operating conditions used for the derivation of the ICRP reference scanner. Scanners are listed alphabetically by manufacturer and model name along with the operating conditions.

Manufacturer	CT model	Tube voltages (kV)	Beam shaping filter	Fan beam
General Electric	Brightspeed 16 Elite	80, 100, 120, 140	Large, Small	
	Discovery CT 750 HD	80, 100, 120, 140	Large, Med, Small	
	Optima CT660	80, 100, 120, 140	Large, Small	
	Lightspeed VCT	80, 100, 120, 140	Large, Med, Small	
Philips	Brilliance 64	80, 120, 140		
	iCT 256	80, 100, 120, 140	Body, Head, Baby	
Siemens	Definition	80, 100, 120, 140	Body, Head	Full, Small
	Emotion 6	80, 110, 130		
	Sensation 16	80, 100, 120, 140	Body, Head	
	Sensation 64	80, 100, 120, 140		
	Sensation Open	80, 100, 120, 140		
Toshiba	Aquilion 16	80, 100, 120, 135	DR-, L-, S-Wedge	

Med, Medium; DR-, Dose Reduction-Wedge; L-, Large-Wedge; S-Wedge, Small-Wedge (Jansen et al. (2022).

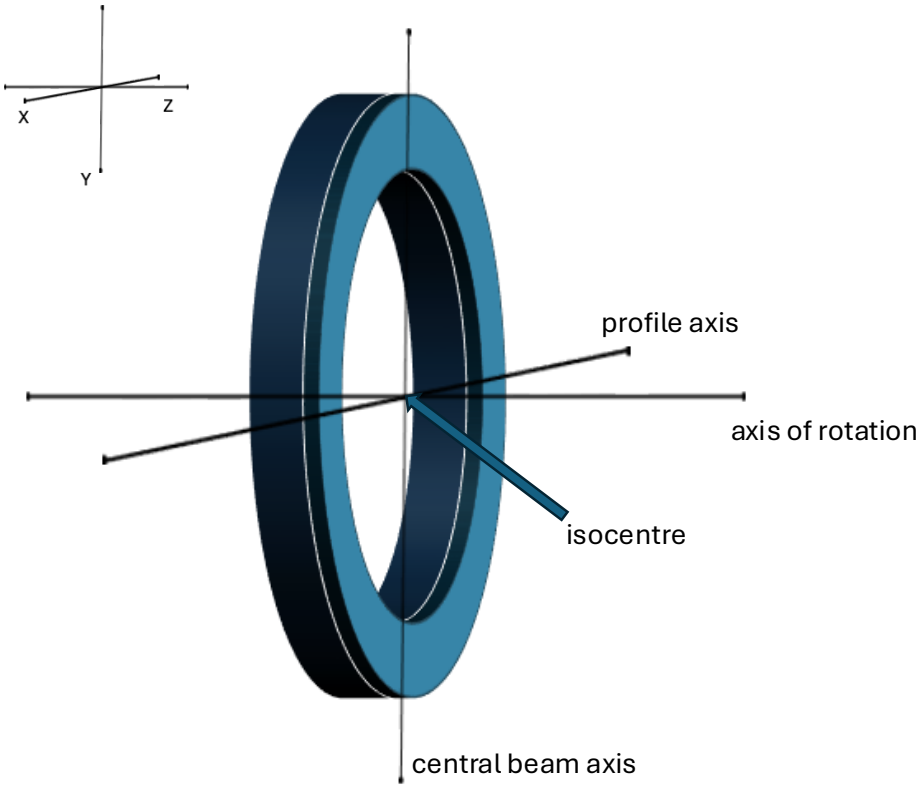

Fig. 3.1. Axis of rotation, central beam axis, profile axis, and isocentre. The dose profiles were generated along the profile axis, which is the line perpendicular to the axis of rotation and central beam axis.

(42) The dose profile simulations were performed with the x-ray focus in a fixed position on the positive Y-axis. The central beam axis was on and towards the negative Y-axis (see Fig. 3.1). The axis of rotation of the CT scanner was the Z-axis, and the point detectors were on the positive and negative X-axis along the profile axis. On the positive X-axis, the detectors were positioned from $X = 0$ cm to $X = 37$ cm in steps of 1 cm. On the negative X-axis, the detectors were positioned from $X = -0.5$ cm to $X = -37.5$ cm in steps of 1 cm, resulting in a total of 76 point detectors along the dose profile. The Monte Carlo simulations were performed in photon transport only mode i.e. no secondary electrons were considered. The photon energy simulated was 60 keV (monoenergetic) rather than an x-ray spectrum; neutral (photon) particle transport was disabled so only pseudoparticles (Kulesza et al., 2022) from the source to the point detector were transported for the attenuation calculation. Note that pseudoparticles (photons) are defined as the next event deterministic photons, transported from the simulated photon source (or collision) location to the detector. Further details of the Monte Carlo simulations are provided in Table 3.2.

Table 3.2. Details of the methodology used for the Monte Carlo calculations in the derivation of the dose profiles.

Radiation transport code	MCNP6.1 (Pelowitz, 2013)
Cross section libraries	Photon library: MCPLIB84 (White, 2012) Electron library: EL03 (X-5 Monte Carlo Team, 2003)
Particles considered Particles transported	Photons pseudoparticles only
Energy range considered	Monoenergetic, 60 keV
Source Collimation Surrounding medium	Idealised, isotropic point source, collimated beams Idealised Air
Quantity determined	Air kerma
Normalisation quantity	The dose profiles are normalised to a central value of unity (air kerma / air kerma)
Purpose of dose simulations	To determine dose profiles

(43) The result of each of the Monte Carlo simulations was a dose profile that represents the contribution to the detector (expressed as air kerma) from the source (focus) per starting source photon. In effect, each dose profile represents the transmission of x-rays through the material between the focus and each of the 76 point detectors in a straight line without taking into account any contribution from scatter.

(44) The calculations described above were performed for both Body and Head beam shaping filters across all 13 scanner models. The dose profiles for each simulated scanner were then normalised to a central value of unity by dividing all dose profiles values by the central dose profile value. For each of the 76 point detectors, the 13 normalised profiles were then averaged to define the Body and Head filter dose profiles of the ICRP reference scanner.

(45) The dose profiles are bell-shaped, i.e. they are highest in the centre and lower towards both edges. An example is shown in Fig. 3.2. This shape results not only from the increased attenuation due to the beam shaping filter but also from the increased distance between the focus and the detectors. Distance corrections were therefore applied to ensure that the shape of the profile was solely dependent on attenuation. Further, the thickness of the beam shaping filter is measured parallel to the Y-axis. However, except for the detector at the isocentre the photon beams are incident at an angle, thus increasing the apparent beam shaping filter thickness with the inverse cosine of the angle. Consequently, an angle correction was also required. Application of the distance and angle corrections resulted in beam shaping attenuation profiles, $A_{\mathrm{Body}}(X)$ and $A_{\mathrm{Head}}(X)$ (note that attenuation A is simply 1 minus transmission). Using the mass attenuation coefficient (Greening, 1985), μ/ρ, of aluminium at 60 keV (White, 2012) and the density, ρ, of aluminium (Lide, 2005), each attenuation profile was converted to a thickness profile $T_{\mathrm{i}}(X)$ using the equation:

$$T_{\mathrm{i}}(X) = \frac{-\ln(A_{\mathrm{i}}(X))}{(\mu/\rho)\rho}, \tag{3.1}$$

where *i* represents Head or Body shaping filter.

(46) These thickness profiles are valid on the line parallel to the profile axis going through the isocentre ($Y = 0$). However, the beam shaping filter will actually be located at a different position on the Y-axis, termed Y_{filter}, (i.e. not on the axis of rotation shown in Fig 3.1). The isocentre is at $Y = 0$ and the focus is at Y_{focus}. The variable X in the thickness profile $T_{\mathrm{i}}(X)$, is for location $Y = 0$ (the isocentre), so for a location $Y = Y_{\mathrm{filter}}$ it should be linearly scaled with the distances to the focus (using the principle of similar triangles). Consequently, it is necessary

to define the variable X_{filter} which, at filter location Y_{filter}, is related to the variable X on the profile axis by:

$$X_{\text{filter}} = \frac{X(Y_{\text{focus}} - Y_{\text{filter}})}{Y_{\text{focus}}}. \quad (3.2)$$

(47) The beam shaping filter is symmetrical around Y_{filter}. In addition, since the ICRP reference scanner dose profiles are symmetric around the $X = 0$ plane, the beam shaping filters were implemented symmetrically around the same plane. For convenience, the beam shaping filter is assigned a thickness of zero (i.e. very small) for the $X = 0$ profile point. The beam shaping filter position Y_{filter} is dependent on the normalised thickness profile $T_i(X_{\text{filter}})$ thus:

$$Y_{\text{filter}}(X) = Y_{\text{filter}} \pm \frac{\ln(A_i(X_{\text{filter}}))}{2(\mu/\rho)\rho}. \quad (3.3)$$

(48) This results in 76 profile thickness combinations (X_{filter}, Y_{filter}), for each of the beam shaping filters on each side of the origin. The beam shaping filter is implemented symmetrically around the $Y = Y_{\text{filter}}$ plane.

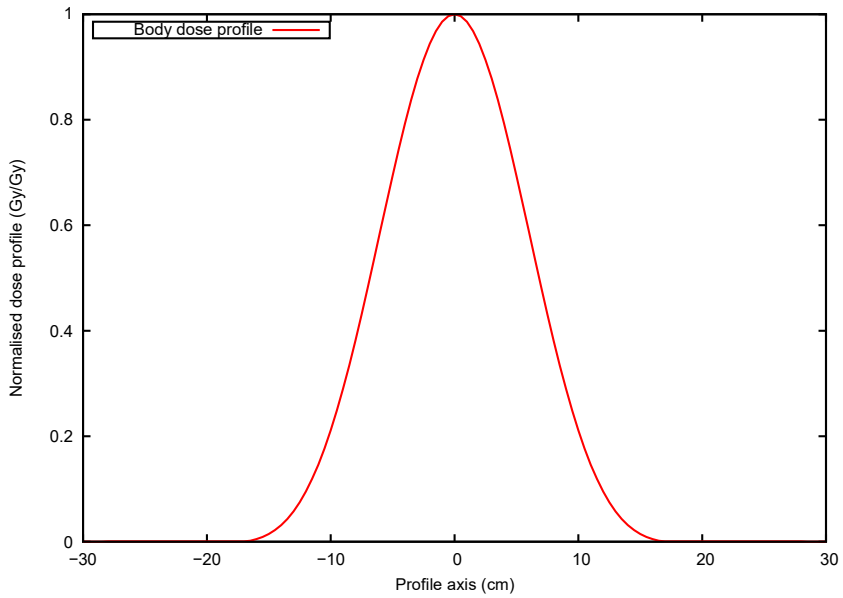

Fig. 3.2. Dose (transmission) profile for a typical Body beam shaping filter along the distance of the profile axis. This dose profile is calculated with MCNP6.1 based on the 32-cm-diameter CT dosimetry phantom, with the assumption of constant detector values, for mono-energetic photon energy of 60 keV normalised to a central value of unity by dividing all dose profiles values by the central dose profile value.

(49) The maximum thickness of the Body filter is 34.5 mm Al and of the Head filter 36.4 mm Al. Fig. 3.3(a) shows a rendered view of the Body beam shaping filter, while Fig. 3.3(b) provides a lateral view of the filter within the ICRP reference scanner's geometric configuration.

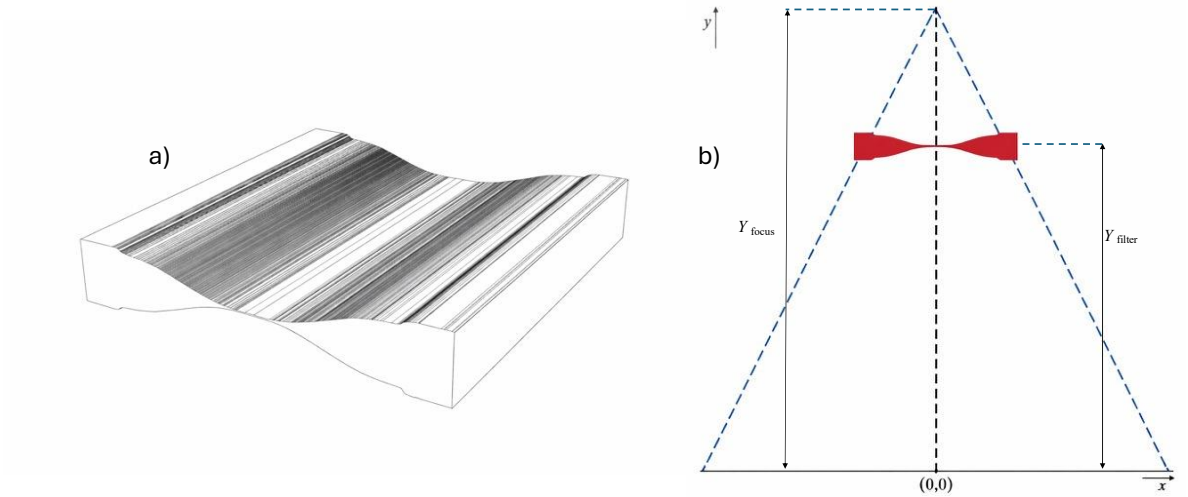

Fig. 3.3. (a) Rendered view of the aluminium Body beam shaping filter of the ICRP reference scanner giving a three-dimensional view of its shape. (b) Lateral view of the Body beam shaping filter showing geometry. Y_{focus} is the focus to isocentre distance (57 cm) and Y_{filter} is the distance from the beam shaping filter to the isocentre. The maximum thickness of the filter, i.e. at its outermost edge, is 34.5 mm. Y_{filter} is 40 cm at $X = 0$.

3.5. Homogenous x-ray filter

(50) The scanners listed in Table 3.1 incorporate homogenous beam hardening x-ray filters made of various materials and thicknesses. To determine the thickness of aluminium required for the beam hardening filter of the ICRP reference scanner, it was necessary to identify an equivalent thickness of aluminium that best represents the simulated scanners. To do so, a series of x-ray spectra were generated at 120 kV with a 7 degree target angle with filter thicknesses of 3, 5, 7, 9, and 11 mm aluminium using the IPEM Report 78 software (Sutton et al., 2015). For all five spectra, the free-in-air dose ($CTDI_{free\text{-}in\text{-}air}$) and the central dose ($CTDI_{centre,32}$) in the 32-cm-diameter CT dosimetry phantom (IEC, 2016) were calculated using the Head filter; the ratio of $CTDI_{centre,32}$ / $CTDI_{free\text{-}in\text{-}air}$ was then determined. (See Annex C for detail of dosimetric quantities) The same ratio was also calculated for each simulated CT scanner operating at 120 kV using the same beam shaping filter, and the average over all the CT scanners was determined. Interpolation of the results obtained for the five spectra indicated that a homogenous beam shaping thickness of 8.2 mm Al resulted in a ratio closest to this average. Note that the Siemens Emotion 6 scanner was excluded since it cannot operate at 120 kV. It should also be noted that the Head beam shaping filter was used because it narrows the beam compared to the Body beam shaping filter and is therefore more akin to the ICRU recommended HVL measurement geometry (ICRU, 1964) which excludes scatter contribution. Moreover, the 32-cm-diameter phantom provides more attenuation than the 16 cm phantom, thus making the calculation uncertainty smaller.

3.6. Tube voltages and beam shaping filters used in the reference scanner

(51) Each of the simulated CT scanners and operating conditions shown in Table 3.1 was matched to the ICRP reference scanner by selecting a tube voltage, i.e., 80, 100, 120, or 140 kV and a beam shaping filter Body or Head. So, for example, it was considered that the GE Lightspeed VCT operating at 100 kV with the Body filter should be best approximated by the ICRP reference scanner operating at 100 kV with a Body filter.

(52) The free-in-air dose ($CTDI_{free\text{-}in\text{-}air}$) and the central and peripheral doses in the 32 and 16-cm-diameter CT dosimetry phantoms were calculated for all tube voltages and both beam shaping filters for all the scanners listed in Table 3.1. The peripheral dose was calculated as the average of the dose at the four peripheral positions for each operating condition. For both dosimetry phantoms, the normalised CTDI was derived at the centre and periphery by dividing by the $CTDI_{free\text{-}in\text{-}air}$ (resulting in values of normalised $CTDI_{periphery,32}$, normalised $CTDI_{periphery,16}$, normalised $CTDI_{centre,32}$, and normalised $CTDI_{centre,16}$). All values of normalised $CTDI_w$ were also calculated as was the effective dose E_{103} per normalised $CTDI_{w,16}$ and normalised $CTDI_{w,32}$.

(53) The same normalised CTDI parameters described above were calculated for the ICRP reference scanner—using the beam shaping filters and homogenous filter—at tube voltages of 80, 100, 120, and 140 kV, with an anode angle of 7 degrees, as generated by the IPEM report 78 spectrum software (Sutton et al., 2015). The root mean squared deviation of the normalised CTDI values for each set of matched scanners (biased standard deviation) from those of the reference scanner was also calculated.

(54) Since the normalised CTDI pairs characterise the dosimetric performance of a scanner, plots of normalised $CTDI_{periphery,32}$ vs normalised $CTDI_{centre,32}$ and normalised $CTDI_{periphery,16}$ vs normalised $CTDI_{centre,16}$ were generated for each group of matched scanners and the associated reference scanner operating condition (i.e. tube voltage and filter).

(55) These plots confirm the validity of the ICRP scanner as a surrogate for all scanners, provided that a range of tube voltages and two beam shaping filters are employed. An example is given in Fig 3.4 which shows normalised $CTDI_{periphery,32}$ vs normalised $CTDI_{centre,32}$ for every CT scanner model, colour coded according to the match with the ICRP reference scanner tube voltage. The same ratio is shown for each reference scanner operating condition with the biased standard deviations shown as error bars.

(56) Fig. 3.4 demonstrates a statistically significant difference between the centre normalised CTDIs for the ICRP reference scanner at the highest and lowest tube voltages (based on the biased standard deviations). For the intermediate tube voltages, the differences are reduced but still evident. Similarly, for both normalised CTDIs, the Head beam shaping filter values are lower than the Body beam shaping filter values at all values of tube voltage. Using four tube voltages and two beam shaping filters in the ICRP reference scanner clearly reduces the uncertainty in the normalised central and peripheral CTDI values compared to the option of combining all tube voltages and beam filters, by for example simply averaging all of the 102 operating conditions available (see also Section 7.3).

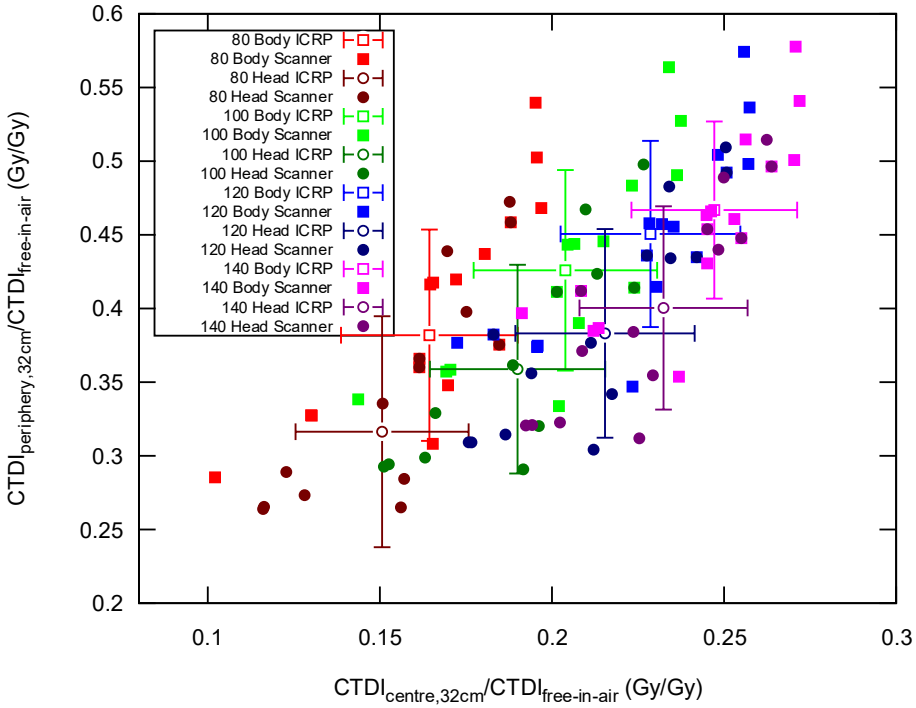

Fig. 3.4. Normalised $CTDI_{periphery,32}$ vs normalised $CTDI_{centre,32}$ for each CT scanner model, colour coded according to the match with the ICRP reference scanner operating condition. The same ratio is shown for each reference scanner operating condition with the biased standard deviations shown as error bars.

3.7. Monte Carlo simulations to derive dose coefficients for the ICRP adult reference phantoms

(57) Monte Carlo calculations were performed to determine the organ absorbed dose coefficients and $\sum w_T \times H_T^M$ or $\sum w_T \times H_T^F$ (termed $E_{103,AM}$ or $E_{103,AF}$, as described previously) normalised to $CTDI_{free\text{-}in\text{-}air}$, for the adult phantoms exposed to the ICRP reference scanner. Additionally, in order to facilitate comparison of the ICRP reference scanner with each of the specific simulated CT scanner models, dose coefficients were also calculated for each scanner used in the generation of the reference scanner.

(58) For both the ICRP reference scanner and the scanners listed in Table 3.1, simulations were performed using the ICRP reference voxel adult male and adult female phantoms (ICRP, 2009) positioned in the supine position (face-up) with the arms removed to represent a patient in the 'arms up' position for a body examination and in the 'arms down' position for a head or neck examination. Calculations carried out for the scanners listed in Table 3.1 were performed for each slice—347 for the female and 222 for the male (see Table 3.7), using the methodology reported in Jansen et al. (2022). A summary of the details of the current calculations for the simulated CT scanners and the ICRP reference scanner is given in Table 3.3. Table 3.4 summarises the differences between the methodology reported in Jansen et al. (2022) and the current calculations.

Table 3.3. Details of the methodology used for the current Monte Carlo calculations using the scanners listed in Table 3.1 and the ICRP reference scanner.

Method	Step 1: Simulate the CT scanner with the focus in a fixed position using the Monte Carlo technique and write the photons hitting the cylindrical surface along the rotation axis to a phase-space file Step 2: Rotate the photons in the phase-space file from Step 1 over a random angle, or for the cos distribution for the angular tube current modulation, using an in-house program Step 3: Using the rotated phase-space file from Step 2 as the source, simulate the anthropomorphic phantoms, CT dosimetry phantoms, and the free-in-air geometry using the Monte Carlo technique
Radiation transport code	MCNP6.1 (Pelowitz, 2013)
Cross section libraries	Photon library: MCPLIB84 (White, 2012) Electron library: EL03 (X-5 Monte Carlo Team, 2003)
Anthropomorphic phantoms	ICRP reference adult phantoms (ICRP, 2009)
Surrounding medium	Air
Particles considered	Photons using the thick-target bremsstrahlung model
Energy range considered	1 keV – 100 MeV
Source	Step 1: Photon, from a truncated isotropic point source which is idealised i.e. fully collimated and phantoms placed in air Step 2: Phase-space file from Step 1 Step 3: Phase-space file from Step 2
Dose	Step 1: None Step 2: None Step 3: Organ absorbed doses; for skeletal tissues, dose enhancement factors were applied (ICRP, 2010, 2023a, 2025); $E_{103,AM}$ and $E_{103,AF}$, termed male and female contribution to effective dose, respectively Air kerma in the free-in-air geometry and in the 16 and 32-cm-diameter CT dosimetry phantoms
Normalisation quantity	Step 3: Air kerma in the free-in-air geometry or CTDI in the free-in-air geometry
Purpose of dose simulations	To determine the organ dose coefficients

Table 3.4. Differences in the methodology used for the Monte Carlo calculations reported by Jansen et al. (2022) versus the current calculations.

Radiation transport code	MCNPX2.7.0 (Pelowitz, 2011) versus MCNP6.1 (Pelowitz, 2013)
Anthropomorphic phantoms	ICRP reference adult phantoms with arms versus without arms
Target organ	Lymph nodes, except the lymph nodes in the extra thoracic region and the thoracic region, as in *Publication 110* (ICRP, 2009), versus all lymph nodes, as in *Publication 144* (ICRP (2020c)
Dose enhancement factor	The dose enhancement factor for endosteum in the medullary cavity according to Jansen et al. (2018) versus dose enhancement factor of 1.0 (ICRP, 2025).

3.8. Comparison of dose coefficients calculated for the ICRP reference scanner with those calculated for the individual scanners

(59) Comparisons of dose coefficients determined using the ICRP reference scanner and coefficients calculated using the individual CT scanner models were conducted to benchmark the performance of the ICRP reference scanner and identify how representative it is. To do so, the dose coefficients for the individual CT scanner models at the appropriate operating conditions were summarised in terms of the average and the average plus or minus the standard deviation along the length of the male and female phantoms. Since all the dose coefficients for the ICRP reference scanner remained within upper and lower standard deviation boundaries, this virtual scanner behaves as a representative approximation of the simulated CT scanner models.

(60) An example is given in Fig. 3.5 which shows, for 1-cm slice thicknesses, $E_{103,AF}$ normalised to $CTDI_{free\text{-}in\text{-}air}$, plotted against distance in cm along the adult female phantom [phantom is without arms, as explained in Paragraphs (32) and (58)], for the ICRP reference scanner operated at 140 kV (black solid line). The figure also depicts the average result of this quantity (dashed grey line) for all simulated CT scanners (operating at or near 140kV) with the beam shaping filter chosen to be equivalent to the Body beam shaping filter of the ICRP scanner, along with lines showing one standard deviation above and below the average (orange and blue lines, respectively).

(61) The figure clearly shows that the curve for the ICRP reference scanner follows the average curve closely, indicating that the ICRP reference scanner is behaving as an average CT scanner for this group of CT scanners at these operating conditions.

(62) In the same way, Fig. 3.6 shows the normalised $E_{103,AM}$, for the adult male phantom and the CT scanner models operated at 80 kV, with the beam shaping filter equivalent to the Body filter of the ICRP reference scanner. Analysis shows that the dose coefficients of the ICRP reference scanner are within one standard deviation of the averaged dose coefficients of the CT scanner models but some difference between these curves can be observed for the abdominal and chest region i.e. at distances from 10 cm to 50 cm along the phantom.

(63) Similar behaviour to that shown by $E_{103,AF}$ and $E_{103,AM}$, is observed for all organ absorbed dose coefficients contributing to the effective dose. Two examples are given in Figs 3.7 and 3.8. Fig. 3.7 shows $D_{Colon,AF}$ normalised to $CTDI_{free\text{-}in\text{-}air}$, plotted against the height along the adult female phantom in cm, operated at or near 120 kV, with the beam shaping filter chosen to be equivalent to the Body filter of the ICRP reference scanner. Fig. 3.8 shows similar data for $D_{Colon,AM}$ plotted against the height of the male adult phantom. In both figures the relevant dose coefficients for the ICRP reference scanner are shown as a black line. A more detailed analysis can be found in Annex A. Figures for both phantoms and all organs contributing to the effective dose can be found in the electronic supplement.

(64) As a result of these comparisons, it was concluded that the ICRP reference scanner can be used for the calculation of dose coefficients.

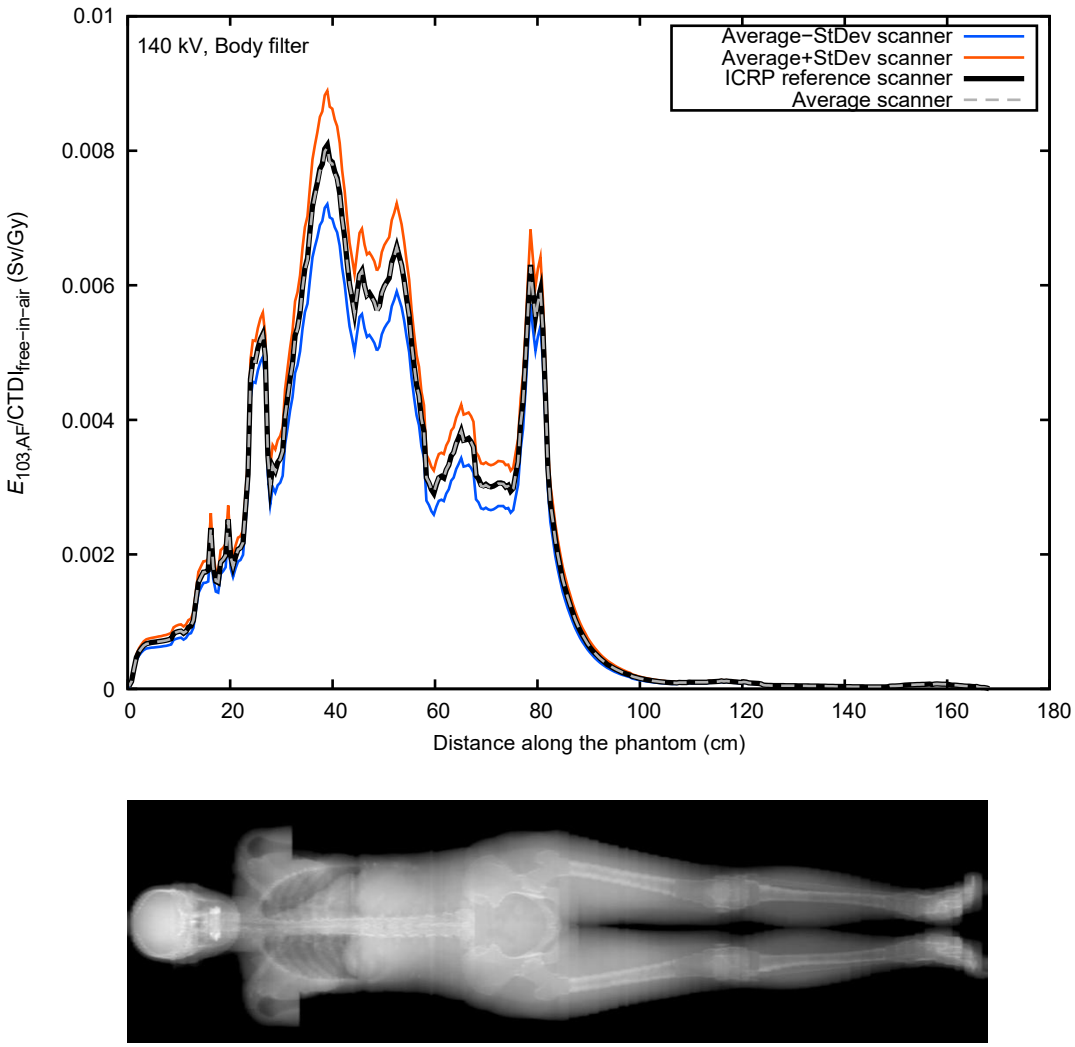

Fig. 3.5. $E_{103,AF}$ normalised to $CTDI_{free\text{-}in\text{-}air}$ corrected to a 1-cm slice thickness shown for every slice along the long axis of the adult reference female phantom, for the ICRP reference scanner (black thick line) operating at 140 kV. Also shown are the average values of all simulated scanners (dashed grey line) and one standard deviation above and below the average (orange and blue lines, respectively). The filter used for each simulated scanner is that selected to be equivalent to the Body filter of the ICRP reference scanner for these operational conditions. The top of the head of the phantom is at position of 0 cm and the X coordinates increase towards the bottom of the feet. For convenience, the adult female phantom without arms, is shown at the bottom of the figure to help visualising the distance along the phantom. Note, that the pixel intensities are scaled with the logarithm of the attenuation.

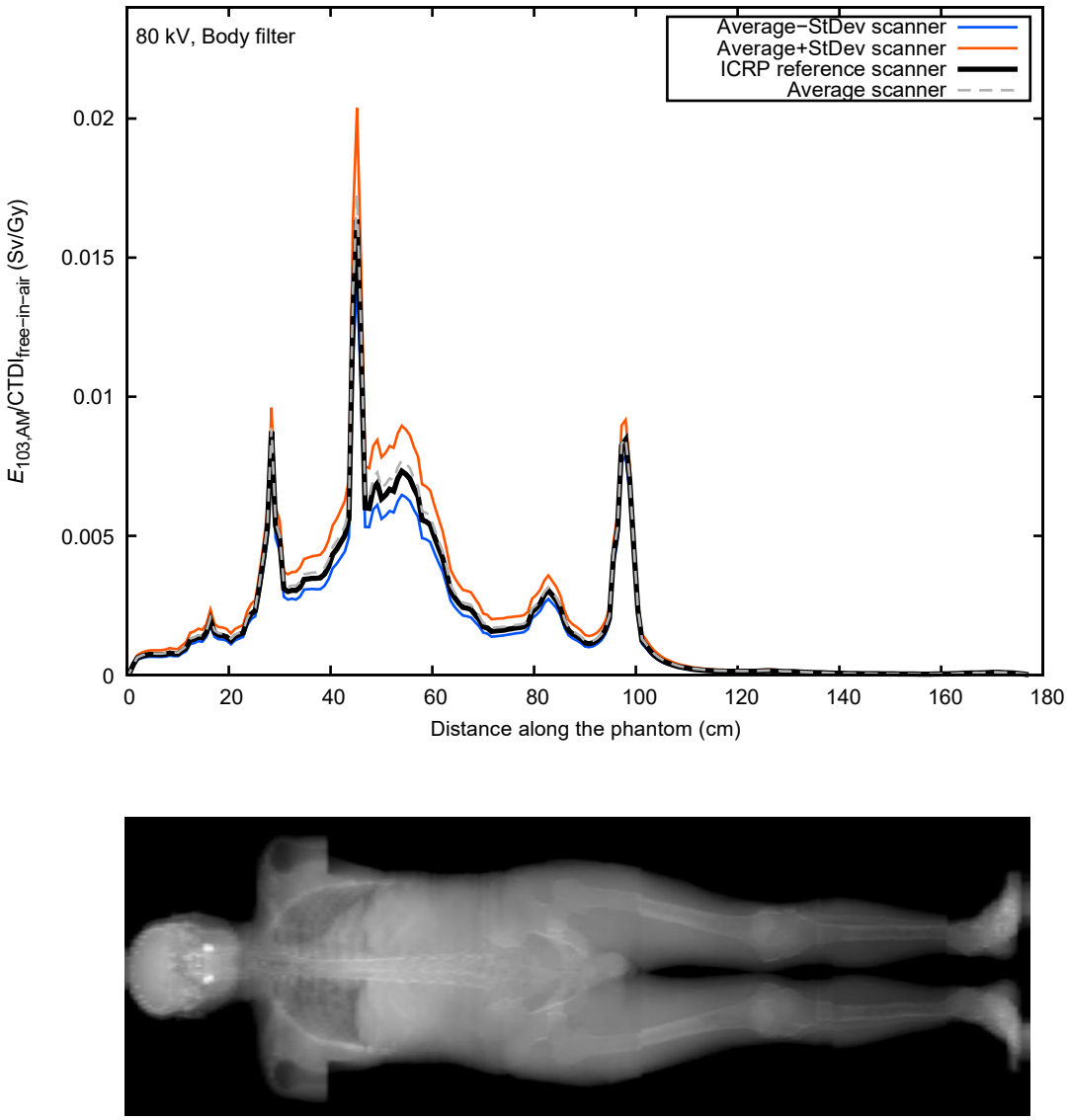

Fig. 3.6. $E_{103,AM}$ normalised to CTDI$_{free-in-air}$ corrected to a 1-cm slice thickness shown for every slice along the long axis of the adult male phantom, without arms, for each simulated CT scanner as average minus standard deviation (blue line), average (dashed grey line), average plus standard deviation (orange line) at 80 kV. The filter used in each is that selected to be equivalent to the Body filter and the values obtained for the ICRP reference scanner (black thick line) for these operational conditions. The top of the head of the phantom is at position of 0 cm and the X coordinates increase towards the bottom of the feet. For convenience, the adult male phantom, without arms, is shown at the bottom of the figure to help visualising the distance along the phantom. Note that the pixel intensities are scaled with the logarithm of the attenuation.

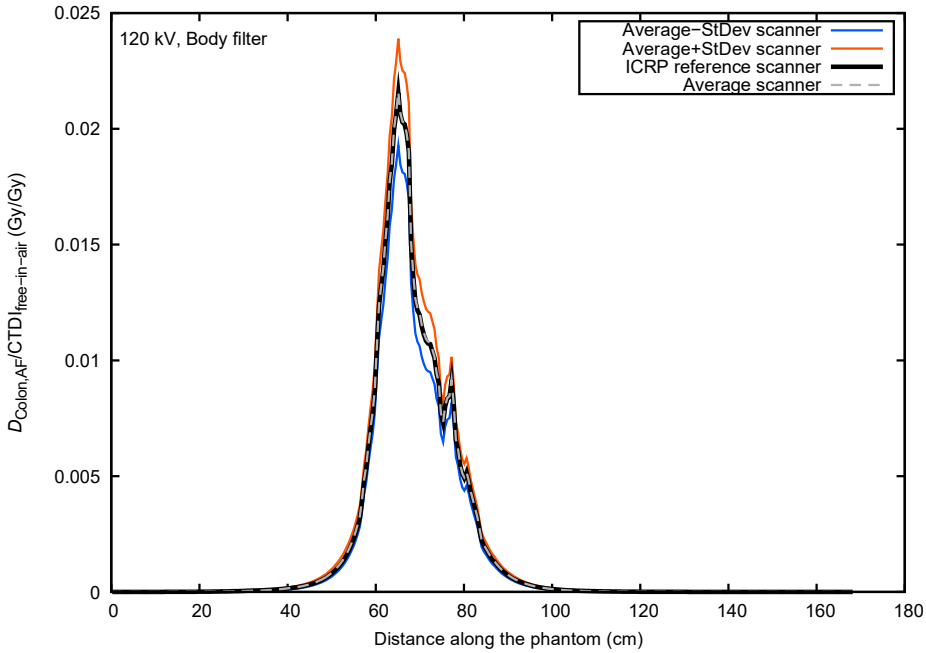

Fig. 3.7. $D_{Colon,AF}$ normalised to $CTDI_{free-in-air}$ corrected to a 1-cm slice thickness shown for every slice along the long axis of the adult female phantom, without arms, for each simulated CT scanner as average minus standard deviation (blue line), average (dashed grey line), average plus standard deviation (orange line) at 120 kV. The filter used in each is that selected to be equivalent to the Body filter and the values obtained for the ICRP reference scanner (black thick line) for these operational conditions. The top of the head of the phantom is at position of 0 cm and the X coordinates increase towards the bottom of the feet, as in Fig. 3.5.

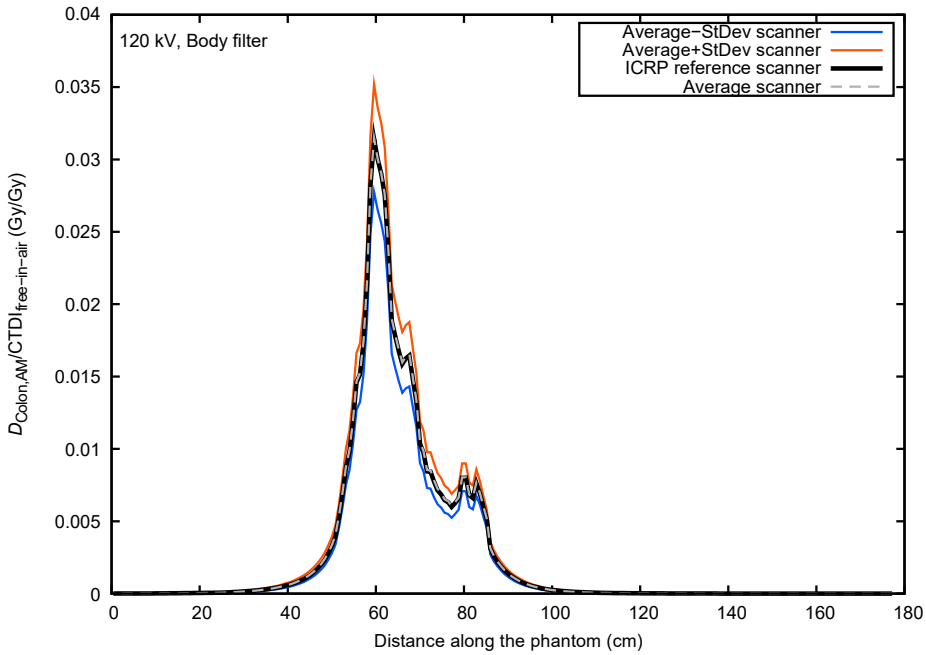

Fig. 3.8. $D_{Colon,AM}$ normalised to $CTDI_{free-in-air}$ corrected to a 1-cm slice thickness shown for every slice along the long axis of the adult male phantom, without arms, for each simulated CT scanner as average minus standard deviation (blue line), average (dashed grey line), average plus standard deviation (orange line) at or near 120 kV. The filter used in each is that selected to be equivalent to the Body filter and the values obtained for the ICRP reference scanner (black thick line) for these operational conditions. The top of the head of the phantom is at position of 0 cm, and the X coordinates increase towards the bottom of the feet, as in Fig. 3.6.

3.9. Monte Carlo simulations to derive paediatric dose coefficients using the ICRP reference scanner

(65) Once the ICRP reference scanner had been developed and tested, dose coefficients for the paediatric phantoms were generated by a different dose calculation group using a different CT simulation method and employing the Monte Carlo radiation transport code MCNPX2.7. The method used will be described below.

(66) A general-purpose Monte Carlo transport code, MCNPX2.7 (Pelowitz, 2011), was employed to calculate organ and effective dose coefficients. The MCNPX2.7 source definition code previously developed for a Siemens Sensation 16 scanner (Lee et al., 2015) was adopted as a template. The source routine includes x-ray spectra, random sampling of particle starting positions, and directions within the fan beam in both vertical and horizontal planes. To improve computational performance, beam shaping (bowtie) flattening filters were not explicitly modelled in the Monte Carlo simulations but were accounted for using attenuation-based statistical weighting factors. Additionally, to further increase efficiency, source sampling was confined to the fan beam angle, eliminating the need for a point source with explicit collimators. Since MCNPX2.7 lacks built-in support for such customised sampling, a user-defined source routine was developed in FORTRAN90 and integrated with MCNPX2.7 code to produce the executable. The ICRP reference scanner data described above were incorporated into the user source code through the following steps.

(67) First, x-ray spectra were generated using IPEM Report 78 software (Sutton et al., 2015), based on the tube voltages of 80, 100, and 120 kV and 8.2 mm aluminium filtration thickness. An anode angle of 7 degree and 0% ripple were assumed. The x-ray spectra were implemented into the MCNPX2.7 user source routine.

(68) Next, attenuation weighting factors for the beam shaping filters were created using the input files describing the ICRP reference scanner. For this purpose, a virtual CTDI ionisation chamber was placed on the patient table to calculate a $CTDI_{free\text{-}in\text{-}air}$ profile at the angle ranging from 0 to 26 degrees with reference to the x-ray source location. The angles correspond to the distance from the beam centre of 0 to 27.80 cm.

(69) The attenuation profiles were derived for the Head and Body beam shaping filters separately. The profiles were fitted to exponential curves (Fig. 3.9), which were then implemented into the MCNPX2.7 user source routine.

(70) The ICRP reference voxel paediatric phantoms (ICRP, 2020) were then implemented into MCNPX2.7 input files by using the lattice structure format. The elemental composition data were converted to MCNPX format and implemented into the main input files. Details of the Monte Carlo simulation in the derivation of the beam profiles using MCNPX2.7 are provided in Table 3.5.

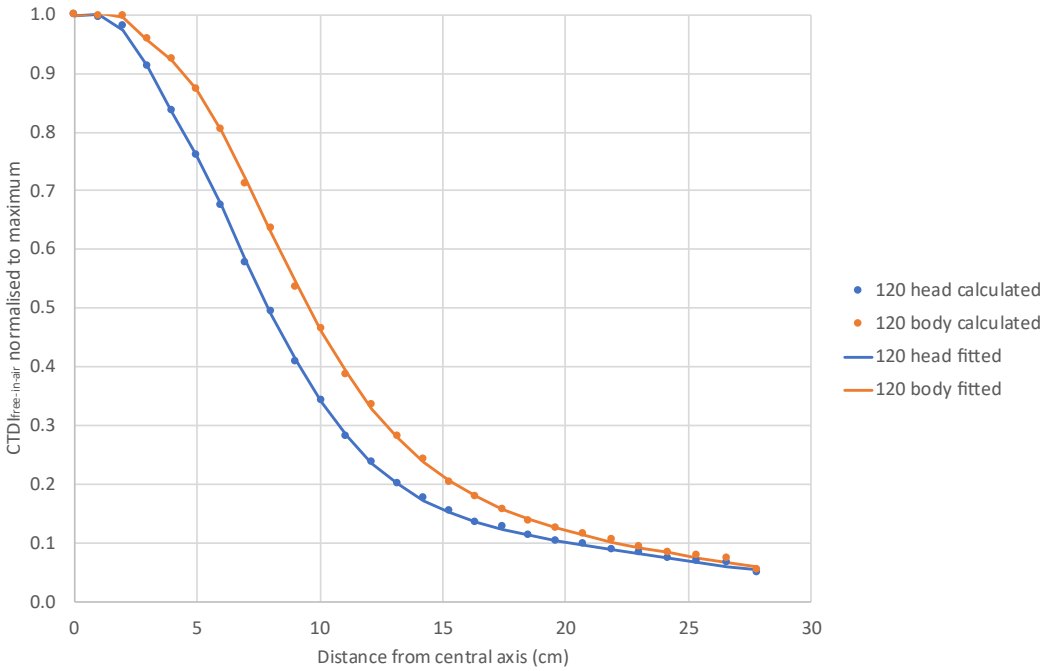

Fig. 3.9. Calculated $CTDI_{free\text{-}in\text{-}air}$ (solid markers) and fitted curves (solid lines) for 120 kV Head (blue) and Body (orange) beam shaping filters, demonstrating the attenuation profiles.

(71) After incorporating the ICRP reference scanner into the MCNPX2.7 code, organ absorbed dose calculations for all 12 paediatric phantoms and all slices were performed for the three tube voltages considered i.e. 80, 100, and 120 kV. For details of the slice numbers and their thickness, see Table 3.7.

(72) The absorbed doses to 28 organs and tissues were calculated along with $E_{103,\#\#M}$ or $E_{103,\#\#F}$. Similarly to the adult reference phantoms, the organ and tissue tags were selected for dose scoring in Monte Carlo calculations. For the determination of red bone marrow (R-marrow) and endosteum (Endost-BS) dose coefficients, fluence for the spongiosa region was scored at 18 different bone sites and the skeletal dose response function and the distribution of red bone marrow and endosteum were applied at each skeletal site (ICRP, 2010, 2023a). For each organ or tissue, the tissue weighting factor from *Publication 103* (ICRP, 2007a) was assigned. Details of the Monte Carlo radiation transport methods adopted in MCNPX2.7 for the calculation of dose coefficients are provided in Table 3.6.

Table 3.5. Details of the methodology used for the Monte Carlo calculations in the derivation of the beam profiles from MCNPX2.7 input files.

Radiation transport code	MCNPX2.7 (Pelowitz, 2013)
Cross section libraries	MCPLIB04/MCPLIB84 (White, 2012)
Particles transported	Photons
Energy considered	120 kV + 8.2 mm Al for 7-degree anode angle and 0% ripple
Source	Idealised, isotropic point source, collimated beams
Collimation	Idealised
Surrounding medium	Air
Quantity determined	$CTDI_{free\text{-}in\text{-}air}$ (Gy photon^{-1})
Normalisation quantity	$CTDI_{free\text{-}in\text{-}air}$ profiles are normalised to the maximum value at the centre
Purpose of dose simulations	To derive beam shaping filter profiles for the MCNPX2.7 user source code using as input the ICRP representative scanner model

Table 3.6. Details of the methodology used for the Monte Carlo calculations of the dose coefficients for the ICRP paediatric reference phantoms.

Purpose of simulation	Primary calculation of paediatric dose coefficients
Radiation transport code	MCNPX2.7
Cross section library	MCPLIB04/MCPLIB84 (White, 2012)
Particles considered	Photons
Energies considered	80, 100, 120, 140 kV
Source	Idealised, isotropic point, collimated beams Collimation is idealised Phantoms placed in air
Anthropomorphic phantoms	Paediatric voxel phantoms (ICRP, 2020b)
Surrounding medium	Air
Position of arms of phantoms	See Section 2
Projections (examinations) simulated	Fan beam irradiating a slice from the top of the head to bottom of the feet with slice thickness as indicated in Table 3.7
Skeletal dosimetry	Use of Dose Response Functions, DRF (ICRP, 2010, 2023a, 2025)
Organ dose coefficients	Red bone marrow (R-marrow), colon, lung, stomach wall (ST-wall), breast, ovaries or testes (gonads), urinary bladder wall (UB-wall), oesophagus, liver, thyroid, skeletal endosteum (Endost-BS), brain, salivary glands (S-glands), skin, remainder tissues: adrenals, extrathoracic region (ET), gall bladder wall (GB-wall,) heart wall (Ht-wall), kidneys, lymph, muscle, oral mucosa (O-mucosa), pancreas, small intestine wall (SI-wall), spleen, thymus, uterus (female) or prostate (male), and lens of the eye (lens)
Effective dose coefficients	The contribution of the male and female reference individuals is given separately
Normalisation quantity	$CTDI_{free\text{-}in\text{-}air}$ (Gy photon^{-1})

3.10. Independent verification of reference dose coefficients (spot checks)

(73) The calculated reference organ and effective dose coefficients for the ICRP paediatric and adult voxel phantoms were independently verified by repeating some of the calculations. The adult dose coefficients calculated by MCNP6.1 were benchmarked by two other methods based on MCNPX2.7 and Geant4, respectively for some specific operating conditions. The paediatric data calculated by MCNPX2.7 were verified by MCNP6.1- and Geant4-based methods, again for some specific operating conditions. Verification was conducted in two different phases: (1) Using ICRP reference scanner without tube current modulation; and (2) using the ICRP reference scanner with tube current modulation implemented. Further details can be found in Annex B.

Table 3.7. Voxel resolution (cm) and corresponding number of axial slices for the ICRP reference phantoms. The phantom height (cm) and number of Monte Carlo output files were derived.

ICRP Phantoms	Voxel Resolution (cm) x	y	z	Slice Thickness, T (cm)	# of Slices	Phantom Height (cm)	# of MC Output Files
00F	0.0663	0.0663	0.0663	0.1326	358	47.5	2148
00M	0.0663	0.0663	0.0663	0.1326	358	47.5	2148
01F	0.0663	0.0663	0.1400	0.1400	546	76.4	3276
01M	0.0663	0.0663	0.1400	0.1400	546	76.4	3276
05F	0.0850	0.0850	0.1928	0.1928	572	110.3	3432
05M	0.0850	0.0850	0.1928	0.1928	572	110.3	3432
10F	0.0990	0.0990	0.2425	0.2425	576	139.7	3456
10M	0.0990	0.0990	0.2425	0.2425	576	139.7	3456
15F	0.1200	0.1200	0.2828	0.2828	571	161.5	3426
15M	0.1250	0.1250	0.2832	0.2832	586	166.0	3516
AF	0.1775	0.1775	0.4840	0.4840	348	168.4	2776
AM	0.2137	0.2137	0.8000	0.8000	222	177.6	1776

4. AUTOMATIC TUBE CURRENT MODULATION (ATCM)

(74) Given the widespread use of Automatic Tube Current Modulation (ATCM) in clinical practice, the Task Group has developed a theoretical ATCM model to allow for tube current modulation along the z-axis or height of the phantom and total tube current modulation around the height, z, and angle, φ. The z modulation can be simulated by applying different weighting factors along the slices of the phantom. The angular modulation can be approximated by using a cosine transformed tube current for each phantom slice. The total modulation can then be represented by combining the z-axis modulation and the angular modulation for each slice, using appropriate weighting factors. The dose coefficients resulting from this model should not be taken as being representative of any manufacturer or scanner. They are intended for educational purposes only and provide an indication of the impact on organ and effective doses when ATCM techniques are employed.

4.1. Description of ATCM

(75) The attenuation of the human body is not uniform (see for example the image of the phantom in the lower panel of Fig. 3.5 demonstrating the attenuation of radiation in the body). Therefore, the use of a constant x-ray tube current in CT examinations will result in strongly varying mean detector signal during a scan. Directions with high attenuation are associated with the highest detector noise and are thus used to determine the tube current required to achieve diagnostic CT images. This, however, results in unnecessarily high doses in directions with less attenuation.

(76) To overcome this issue, manufacturers have continuously implemented and improved techniques to vary the tube current during a CT scan to account for the non-uniform attenuation of the human body. Such techniques are collectively described by the term Automatic Tube Current Modulation (ATCM). Historically, the first algorithms to be used only modulated the tube current along the main body axis (longitudinal or z-modulation) whilst keeping the tube current constant during one rotation. The next step was the development of modulation within the rotation (angular modulation) which is usually implemented along with z-modulation.

(77) In its simplest form, the relation between tube current I and attenuation A can be described by $I \sim A^q$, where q is the modulation strength and depends on the manufacture's choice and usually varies between 0 and 1, where 0 indicates no ATCM (Gies et al., 1999). Analytical calculations have shown that $q = 0.5$ would yield a minimal overall detector noise, while $q = 1$ leads to equal noise in all projections (Gies et al., 1999; Li et al., 2014; Tian et al., 2015).

(78) CT localiser radiographs (CTLR) can be used to develop algorithms that approximate the angular modulation using a (co-)sinusoidal function—this is termed sinusoidal ATCM and is the approach used in this publication. (Other terms sometimes used for the CT localiser are scout, survey, topogram, and scanogram). Sinusoidal ATCM in slice i can be described mathematically (Gies et al., 1999) by

$$I_{\mathrm{i}}(\varphi) \propto \left(A_{\mathrm{i}}^{\mathrm{AP}}\right)^q + \frac{\left(A_{\mathrm{i}}^{\mathrm{RLAT}}\right)^q - \left(A_{\mathrm{i}}^{\mathrm{AP}}\right)^q}{2}(1 + \cos 2\varphi), \qquad (4.1)$$

where $A_{\mathrm{i}}^{\mathrm{RLAT}}$ and $A_{\mathrm{i}}^{\mathrm{AP}}$ signify the attenuation in the right lateral and antero-posterior directions and $\varphi = 0$ and $\varphi = 90$ degrees, respectively. i indicates the serial number of a slice. Detail of how the dose coefficients were subsequently derived using this approach can be found in Section 4.4.

(79) As can be seen from Eq. (4.1), implementation of this scheme for sinusoidal ATCM requires knowledge of the attenuation in the antero-posterior (AP) and right lateral (RLAT)

directions at each longitudinal position within the scan range. This is obtained from the CTLRs [Alternatively, instead of the AP and RLAT directions, the postero-anterior (PA) and left lateral (LLAT) directions could be used]. The human body exhibits varying attenuation along both horizontal and longitudinal axes, so the determination of a single attenuation value A at each of the tube position cannot be performed unambiguously. It is, therefore, necessary to choose a value of A that is in some way representative of the attenuation in each of the AP and RLAT projections for each slice. Since high attenuation regions lead to the highest detector noise, using the maximal attenuation in each projection to represent A_i^{RLAT} and A_i^{AP} seems a justifiable course of action, and is the one adopted in this publication. Another option would be to use the average attenuation in each of the projections. Differences between the two options are explored in Section 4.2.

(80) An alternative approach to implementing angular ATCM is to approximate the value of A at each tube position based on the value of A, measured half a rotation earlier (Kalender et al., 1999a; Popescu et al., 1999). This approach is termed attenuation-based ATCM but is not used in this publication. Schlattl et al. (Schlattl et al., 2010) provides detail of how to calculate dose coefficients if this approach is adopted.

(81) By way of example, a comparison between attenuation-based and sinusoidal ATCM is shown in Fig. 4.1 for the adult female reference phantom at two different representative levels: in a transverse plane around the hip and above the iliac crest. The cross-section of the human body varies along the z-axis, and in many positions is represented poorly by a circle or ellipse. Therefore, the difference between the modulation delivered by sinusoidal and attenuation-based ATCM also varies with the z-position. For example, close to the iliac crest, sinusoidal ATCM is very similar to attenuation-based ATCM (Fig. 4.1a), while they agree less at the level of the hips (Fig 4.1b). Nevertheless, since both approaches lead to a similar modulation of the tube current in the transversal plane, it is not expected that dose coefficients obtained with either of the two approaches would differ substantially.

(82) Recently, a further type of tube current modulation that reduces doses for particular organs at risk (superficial radiosensitive organs such as the breast, thyroid, and eye) has been implemented by manufactures, denoted as organ-based tube current modulation (Layman et al., 2021; Inoue et al., 2024). This approach has not been considered in the present publication.

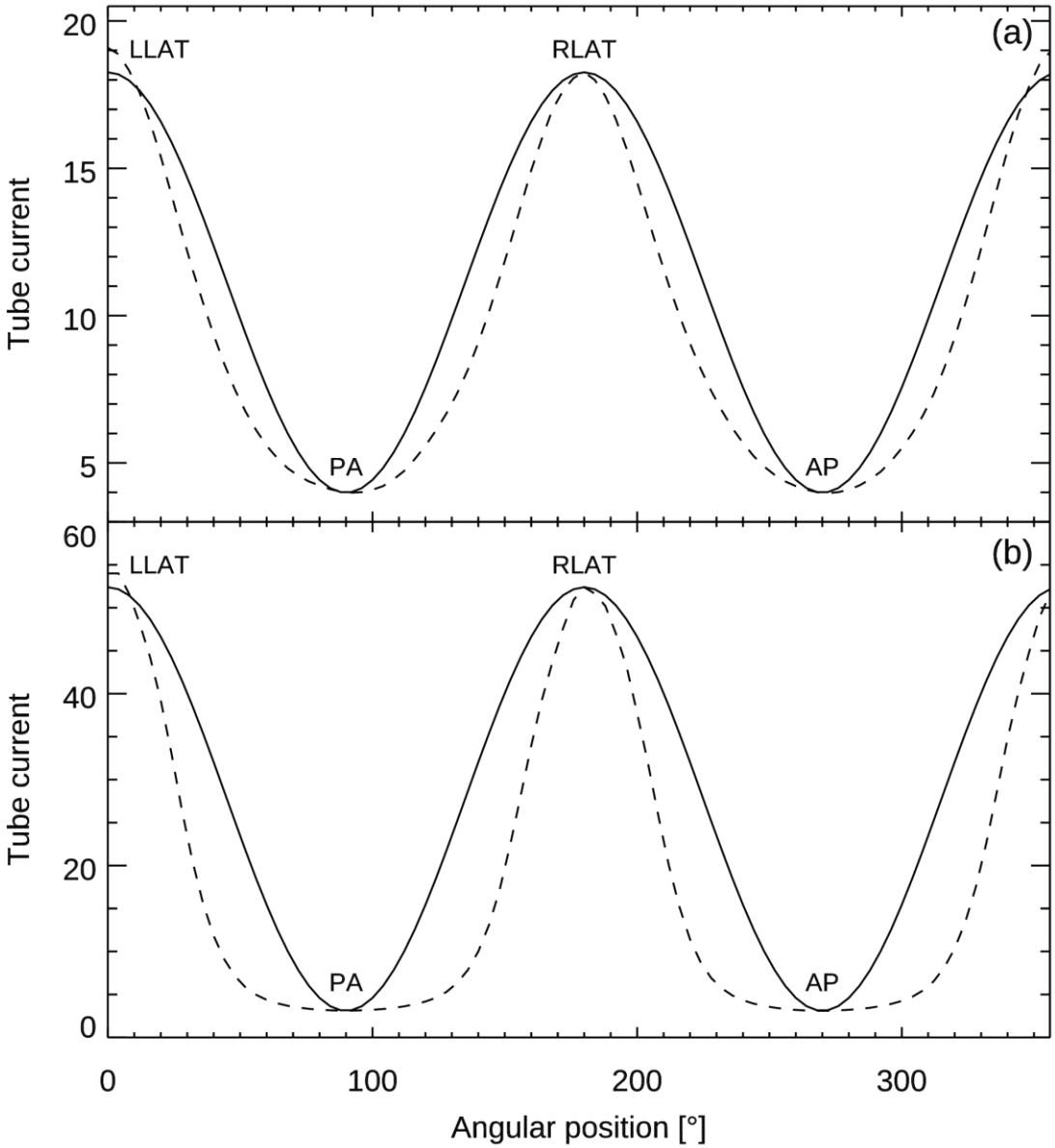

Fig. 4.1. Comparison between attenuation-based (dashed) and sinusoidal (solid lines) ATCM in arbitrary units with modulation strength $q = 0.75$ for the adult reference female phantom and a transversal plane above the iliac crest (a) and at the level of the hips (b). AP, antero-posterior; PA, postero-anterior; RLAT, right lateral; LLAT, left lateral.

4.2. Example of implementation of ATCM on selected phantoms

(83) To obtain the ATCM profiles, CTLRs were generated using Monte Carlo transport simulations on the reference paediatric and adult phantoms, using the Body and Head filters of the ICRP reference scanner at 80, 100, and 120 kV. For the adult phantoms, CTLR images were also simulated at 140 kV, again using both filters. The simulations were performed with an EGSnrc user code (Kawrakow et al., 2009), where the continuous CTLR scans were approximated by stepwise scans with steps equal to the slice thicknesses as given in Table 3.7. A summary of simulation details is given in Table 4.1.

Table 4.1. Details of the methodology used for the Monte Carlo simulations of the CT Localiser Radiograph (CTLR).

Radiation transport code	EGSnrc user code (Kawrakow et al., 2009)
Cross section libraries	XCOM/NIST (Berger and Hubbell, 1987)
Interactions	Photo effect, bound Compton scattering, Rayleigh scattering
Anthropomorphic phantoms	ICRP reference adult (ICRP, 2009) and paediatric (ICRP, 2020b) phantoms; without arms (see Section 2)
Particles considered	Photons, no secondary electrons (Kerma approximation)
Spectra	See Section 3
Source	Point source in vacuum
Geometry	Source-to-isocentre distance: 57 cm Source-to-detector distance: 114 cm Projections: AP & RLAT
Detector	Radial pixel size (at isocentre): 1.5 mm Z pixel size (at isocentre): equal to slice thickness (see Table 3.7) Particle counting detector

AP, antero-posterior; RLAT, right lateral.

(84) CTLR were simulated in both the AP and RLAT directions. An example showing the AP and lateral CTLRs for the adult female phantom, generated at 120 kV is provided in Fig. 4.2. A_i^{AP} and A_i^{RLAT}, as described in Eq., (4.1) were estimated by determining the maximum attenuation in each slice i. A simple smoothing on A_i^{AP} and A_i^{RLAT} was applied to avoid large changes between the slices.

(85) Since the male and female phantoms for the 0-, 1-, 5-, and 10-year-old children have identical anatomy, apart from the gender-specific organs and the urinary bladder, it was assumed that female and male phantoms for these ages lead to the same CTLRs. Thus, in these cases only CTLR images for the male phantoms were simulated, and the resulting ATCM profile was applied to the female phantoms as well.

(86) Figs 4.3 and 4.4 show the resulting profiles of the tube current limits (the minimum and maximum values of tube current) at 120 kV for the lateral and AP directions for the 1-year-old male and 15-year-old female reference phantoms, respectively (cyan lines). The tube current itself varies between the two limits as it rotates around the phantom, as described in Paragraph (68). It can be observed that in the cranial region and the feet, the attenuation in lateral direction is lower than in AP, while in the rest of the body the lateral attenuation is mostly higher, as might be expected. According to Eq. (4.1) this results in a higher tube current in AP than in lateral direction in the cranial region and the feet as opposed to the rest of the body.

(87) As outlined above, the maximal attenuation in each projection has been chosen to deduce representative values of A_i^{AP} and A_i^{RLAT} for each slice, as this corresponds to the lowest detector signal and therefore maximal noise in each projection. Adoption of this option for ATCM ensures that in each projection the maximal noise becomes similar. An alternative option would be to use the average attenuation in each projection as a representative value for A_i, ensuring in this way that the average noise is smoothed by ATCM appropriately. For comparison, the resulting tube current limits based on average instead of maximal attenuation are also shown in Figs 4.3 and 4.4 (yellow lines). As shown, the values are very similar in both cases leading to a very similar longitudinal ATCM. Thus, the dose coefficients obtained with either of the two options would not be substantially different.

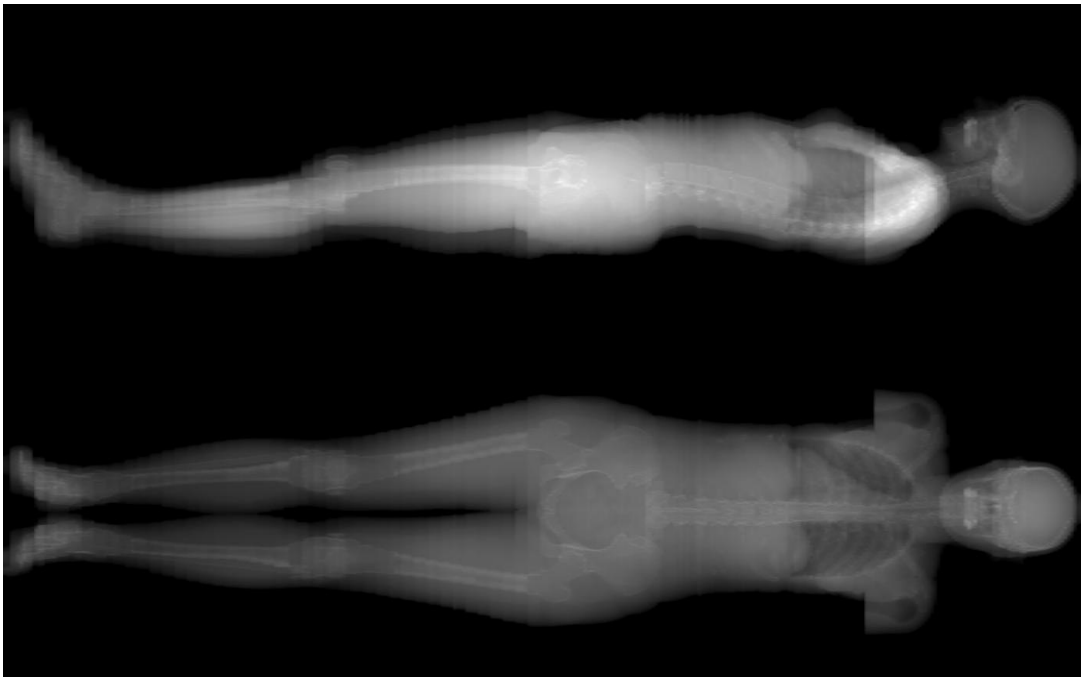

Fig 4.2. RLAT (upper) and AP (lower panel) CTLRs of adult female reference phantom without arms, generated by simulation with EGSnrc using the ICRP reference scanner with Body filter at 120 kV. The pixel intensities are scaled with the logarithm of the attenuation. RLAT, right lateral; AP, antero-posterior; CTLR, CT Localiser Radiograph.

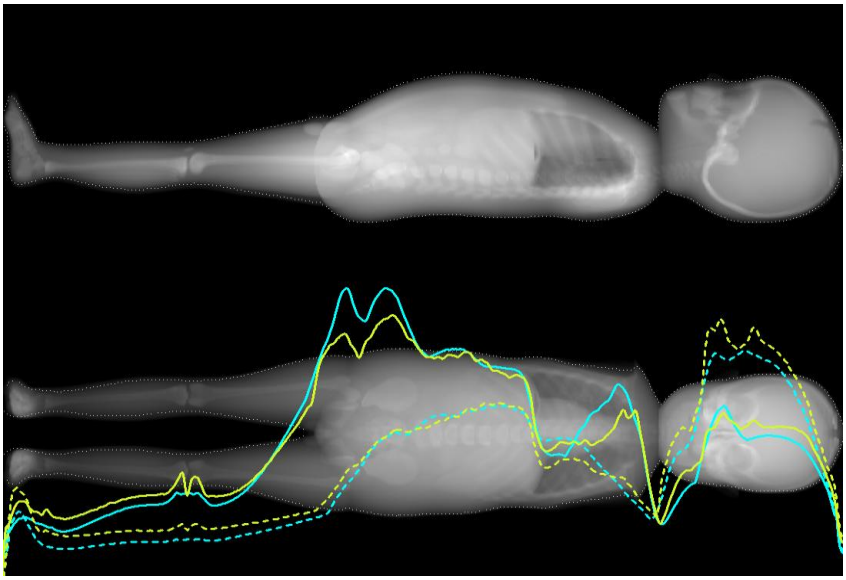

Fig. 4.3. RLAT (upper panel) and AP (lower panel) CTLRs of the 1-year-old male reference phantom without arms generated by simulation with EGSnrc using the ICRP reference scanner with Body filter at 120 kV. The pixel intensities are scaled with the logarithm of the attenuation. Overlaid are the resulting tube current limits for RLAT (solid lines) and AP (dashed lines) based on the maximal (cyan) and average (yellow) attenuation with the modulation strength q = 0.75 in arbitrary units. The dotted lines surrounding the phantom indicate the borders of the region used for determining the average attenuation. RLAT, right lateral; AP, antero-posterior; CTLR, CT Localiser Radiograph.

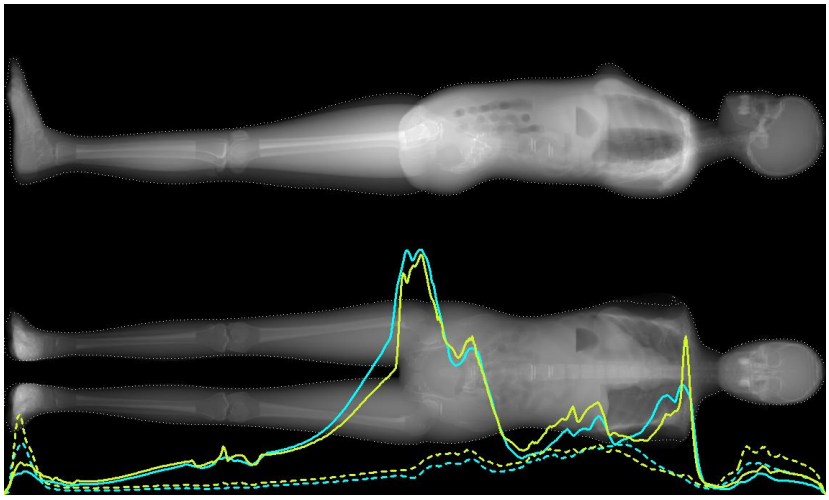

Fig. 4.4. RLAT (upper panel) and AP (lower panel) CTLRs of the 15-year-old female reference phantom without arms generated by simulation with EGSnrc using the ICRP reference scanner with Body filter at 120 kV. The pixel intensities are scaled with the logarithm of the attenuation. Overlaid are the resulting tube current limits for RLAT (solid lines) and AP (dashed lines) based on the maximal (cyan) and average (yellow) attenuation with the modulation strength q = 0.75 in arbitrary units. RLAT, right lateral; AP, antero-posterior; CTLR, CT Localiser Radiograph.

(88) Fig. 4.5 provides a further example for the 1-year-old male reference phantom at 80 kV. As before, the CTLR and resulting tube current limits are shown. Overall, these are very similar to the case with 120 kV (Fig. 4.3). However, the variation of the lateral limit (solid lines) in particular is somewhat stronger for 80 kV than for 120 kV. This is caused by the higher attenuation at 80 kV that is more notable for a larger body diameter, and thus more prominent in lateral than in AP direction.

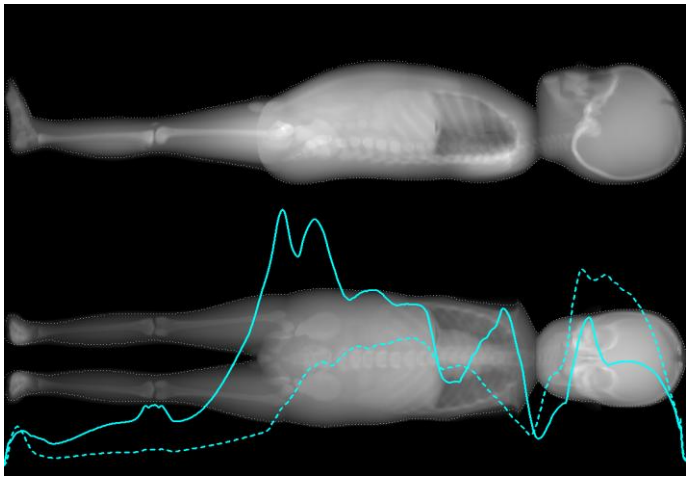

Fig. 4.5. RLAT (upper panel) and AP (lower panel) CTLRs of the 1-year-old male reference phantom without arms generated by simulation with EGSnrc using the ICRP scanner with body filtration at 80 kV. The pixel intensities are scaled with the logarithm of the attenuation. Overlaid are the resulting tube current limits for RLAT (solid lines) and AP (dashed lines) based in the maximal attenuation with modulation strength q = 0.75 in arbitrary units. The dotted lines surrounding the phantom indicate the borders of the region used for determining the average attenuation. RLAT, right lateral; AP, antero-posterior; CTLR, CT Localiser Radiograph.

4.3. ATCM model used in this publication

(89) The choice of the modulation strength q and type of angular modulation described in Section 4.1 are proprietary information specific to each manufacturer and are not fully disclosed. Moreover, actual implementations of ATCM can contain even more parameters that influence the actual tube current—see, for example, Favazza et al. (2015) and Mc Millan et al. (2017). Examples of non-disclosed parameters are:

- Upper and lower limits on the tube current. This means that the tube current is not only depending on settings of the manufacturer but also on the actual image-quality setting chosen by the operator.
- Upper and lower limits on the gradient of the tube current.
- Patient size or protocol-dependent values of the modulation strength q.
- Different values of q for angular and longitudinal modulation.

(90) Hence, CT organ dose coefficients are generally not only scanner-dependent, but also protocol- and operator-dependent. This makes it impossible to compute pre-defined sets of dose coefficients using ATCM that would provide accurate dose estimations (even) for the reference conditions assumed for the calculations of this publication. Accurate patient-specific doses would need to be computed on-the-fly, which is beyond the scope of this publication.

(91) Therefore, it has been decided to provide dose coefficients for a simple but still physics-based model of ATCM. In particular, the assumptions chosen for the implementation presented in this work are:

- Sinusoidal angular ATCM.
- A^{AP} and A^{RLAT} along the body axis are given by the maximal attenuation at each position deduced from antero-posterior and right-lateral CTLR.

(92) As shown above, the difference between attenuation-based and sinusoidal ATCM is small. This is also the case regarding the choice as to whether maximal or average attenuation is used as representative attenuation at each position.

(93) The general modulation strength chosen by each manufacturer depends on their philosophy as to whether overall or minimal noise is better suited to obtain an optimal image quality with least radiation dose. Thus, q is mostly chosen to be between 0.5 and 1. A mean value of $q = 0.75$ has therefore been selected for the GUI-based calculator distributed with this publication.

(94) However, the data provided in the library of dose coefficients allow for the implementation of any modulation strength between zero and one.

(95) In addition, because of the chosen theoretical tube-current scheme, the reported dose coefficients for CT protocols with ATCM are intrinsically associated with higher uncertainties than dose coefficients for constant tube current when applied to patient dose estimations for specific CT devices.

4.4. The derivation of dose coefficients for protocols with and without ATCM

(96) When dose coefficients are normalised to $\mathrm{CTDI_{vol}}$, they are only weakly depending on pitch for the same scan range. Both axial and helical CT protocols can therefore be

approximated by summing individual non-overlapping axial slices (pitch = 1) (Schlattl et al., 2010; Schlattl et al., 2012; Lee et al., 2015).

(97) In what follows, organ dose coefficients in slice *i* for constant tube current normalised to $\mathrm{CTDI_w}$ are denoted as $\left(D_{\mathrm{org}}/\mathrm{CTDI_w}\right)_{\mathrm{i},0}$. Dose coefficients are derived

a) for a protocol $\mathrm{P_C}$ that has no ATCM;

b) for a protocol $\mathrm{P_A}$ that has longitudinal and angular ATCM; and

c) for a protocol $\mathrm{P_L}$ that has only longitudinal ATCM.

(98) The dose coefficient for a protocol with no ATCM ($\mathrm{P_C}$) covering slices *n* to *m* is given by

$$\left(D_{\mathrm{org}}/\mathrm{CTDI_{vol}}\right)_{\mathrm{P_C}} = \frac{\sum_{i=n}^{m}\left(D_{\mathrm{org}}/\mathrm{CTDI_w}\right)_{\mathrm{i},0}(\mathrm{CTDI_w})_{\mathrm{i},0}}{(\mathrm{CTDI_{vol}})_{\mathrm{P_C}}}. \tag{4.2}$$

(99) Since the axial slices do not overlap, the pitch is 1, and thus $\mathrm{CTDI_{vol}}$ is given by the mean $\mathrm{CTDI_w}$ of all slices:

$$(\mathrm{CTDI_{vol}})_{\mathrm{P_C}} = \frac{\sum_{i=n}^{m}(\mathrm{CTDI_w})_{\mathrm{i},0}}{n-m+1}. \tag{4.3}$$

(100) For fixed tube current, $\mathrm{CTDI_w}$ is equal in each slice, which results in

$$(\mathrm{CTDI_{vol}})_{\mathrm{P_C}} = \frac{(\mathrm{CTDI_w})_0 \sum_{i=n}^{m} 1}{n-m+1} = (\mathrm{CTDI_w})_0, \tag{4.4}$$

and thus,

$$\left(D_{\mathrm{org}}/\mathrm{CTDI_{vol}}\right)_{\mathrm{P_C}} = \sum_{i=n}^{m}\left(D_{\mathrm{org}}/\mathrm{CTDI_w}\right)_{\mathrm{i},0}. \tag{4.5}$$

(101) Sinusoidal ATCM in slice *i* can be described mathematically (Gies et al., 1999) by

$$I_{\mathrm{i}}(\varphi) \propto \left(A_{\mathrm{i}}^{\mathrm{AP}}\right)^q + \frac{\left(A_{\mathrm{i}}^{\mathrm{RLAT}}\right)^q - \left(A_{\mathrm{i}}^{\mathrm{AP}}\right)^q}{2}(1+\cos 2\varphi) = \tau_{\mathrm{i}}\left(1+\zeta_{\mathrm{i}}(1+\cos 2\varphi)\right) \tag{4.6}$$

with $\tau_{\mathrm{i}} = \left(A_{\mathrm{i}}^{\mathrm{AP}}\right)^q$ and $\zeta_{\mathrm{i}} = \frac{1}{2}\left(\frac{\left(A_{\mathrm{i}}^{\mathrm{RLAT}}\right)^q}{\left(A_{\mathrm{i}}^{\mathrm{AP}}\right)^q} - 1\right)$ and $\varphi = 0$ being in right-lateral direction.

(102) With this in mind, the computation of dose coefficients with ATCM in each slice can be divided into the computation of

a) dose coefficients without ATCM $\left(D_{\mathrm{org}}/\mathrm{CTDI_w}\right)_{\mathrm{i},0}$ and

b) dose coefficients where the incident fluence (or air kerma or $\mathrm{CTDI_w}$) is proportional to $(1+\cos 2\varphi)$, denoted as $\left(D_{\mathrm{org}}/\mathrm{CTDI_w}\right)_{\mathrm{i},1}$ (see Fig. 4.6).

The advantage is that only these two data sets are required to deduce the dose coefficients for any value of q.

(103) In each slice *i* dose coefficients for angular sinusoidal TCM are then obtained by

$$\left(D_{\mathrm{org}}/\mathrm{CTDI_w}\right)_{\mathrm{i}} = \frac{\left(D_{\mathrm{org}}/\mathrm{CTDI_w}\right)_{\mathrm{i},0}(\mathrm{CTDI_w})_{\mathrm{i},0} + \zeta_{\mathrm{i}}\left(D_{\mathrm{org}}/\mathrm{CTDI_w}\right)_{\mathrm{i},1}(\mathrm{CTDI_w})_{\mathrm{i},1}}{(\mathrm{CTDI_w})_{\mathrm{i},0} + \zeta_{\mathrm{i}}(\mathrm{CTDI_w})_{\mathrm{i},1}}. \tag{4.7}$$

(104) The ratio $(\mathrm{CTDI_w})_{\mathrm{i},1}/(\mathrm{CTDI_w})_{\mathrm{i},0}$ is proportional to the ratio of average tube currents in the two components, i.e. $I_{\mathrm{i},1}/I_{\mathrm{i},0}$, where

$$\frac{I_{\mathrm{i},1}}{I_{\mathrm{i},0}} \propto \frac{\int_0^{2\pi}(1+\cos 2\varphi)\,\mathrm{d}\varphi}{\int_0^{2\pi}\mathrm{d}\varphi} = 1. \tag{4.8}$$

Hence,

$$\left(D_{\mathrm{org}}/\mathrm{CTDI_w}\right)_{\mathrm{i}} = \frac{\left(D_{\mathrm{org}}/\mathrm{CTDI_w}\right)_{\mathrm{i},0} + \zeta_{\mathrm{i}}\left(D_{\mathrm{org}}/\mathrm{CTDI_w}\right)_{\mathrm{i},1}}{1+\zeta_{\mathrm{i}}}. \tag{4.9}$$

(105) Combining these dose coefficients for a protocol with angular and longitudinal modulation P_A covering slices *n* to *m* is analogue to the fixed tube current case. However, the weighting of each slice is proportional to τ_i, thus,

$$\left(D_{org}/\mathrm{CTDI}_{vol}\right)_{P_A} = \frac{\sum_{i=n}^{m}\left(D_{org}/\mathrm{CTDI}_w\right)_i \tau_i (\mathrm{CTDI}_w)_0}{(\mathrm{CTDI}_w)_0 \sum_{i=n}^{m}\tau_i}(n-m+1). \quad (4.10)$$

Dose coefficients for the protocol P_A with angular and longitudinal modulation are then obtained by

$$\left(D_{org}/\mathrm{CTDI}_{vol}\right)_{P_A} = \frac{\sum_{i=n}^{m}\tau_i\left(D_{org}/\mathrm{CTDI}_w\right)_i}{\sum_{i=n}^{m}\tau_i}(n-m+1). \quad (4.11)$$

(106) Pure longitudinal ATCM (z-modulation) is assumed to be based on the maximal attenuation in each slice, i.e.,

$$I_i \sim A_{\max,i}^{q} = \max\left(\left(A_i^{AP}\right)^q, \left(A_i^{RLAT}\right)^q\right) := \eta_i. \quad (4.12)$$

(107) Analogue to the previous case, dose coefficients for a protocol P_L with longitudinal modulation covering slices *n* to *m* are given by

$$\left(D_{org}/\mathrm{CTDI}_{vol}\right)_{P_L} = \frac{\sum_{i=n}^{m}\eta_i\left(D_{org}/\mathrm{CTDI}_w\right)_{i,0}}{\sum_{i=n}^{m}\eta_i}(n-m+1). \quad (4.13)$$

(108) The files in the library of dose coefficients provide values of a) A^{AP}, b) A^{RLAT}, c) η_i (for longitudinal ATCM), and d) τ_i and ζ_i (for combined longitudinal and angular ATCM) for every slice *i* in each ICRP reference phantom at all used tube voltages. Note, that from 0 to 10-year-old the female and male phantoms are essentially the same, except for the gender-specific organs (uterus or prostate, ovaries or testes, and the urinary bladder). Therefore, only a sex-independent set of ATCM parameters is provided for these ages.

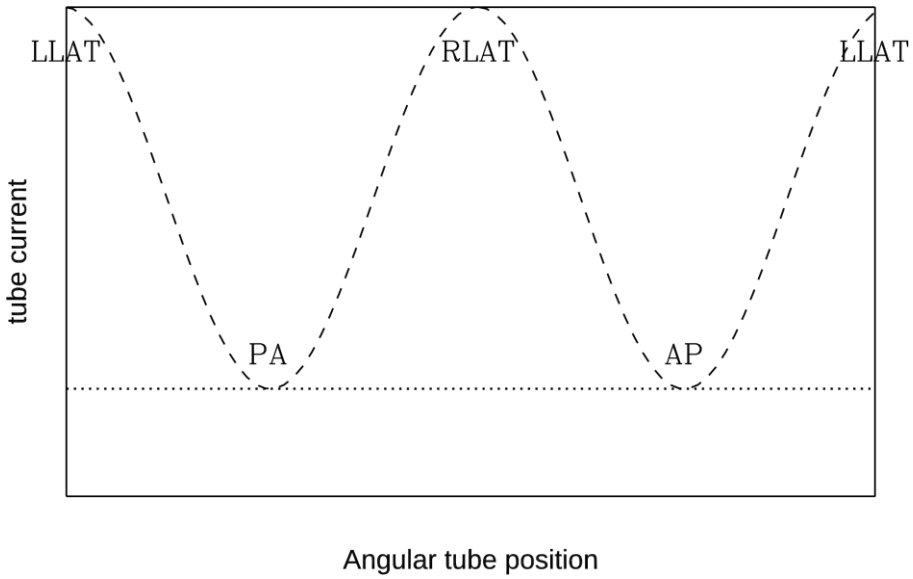

Fig. 4.6. Illustration of the separation of Monte Carlo calculations of dose coefficients for ATCM into two components. In the first simulation, dose coefficients are computed with a fixed tube current (dotted line). In the second step, simulations are performed with sinusoidal tube currents being maximal in lateral directions and zero in AP/PA direction (dashed line). The final dose coefficients for ATCM are obtained by summing these two components. AP, antero-posterior; PA, postero-anterior; RLAT, right lateral; LLAT, left lateral.

(109) To summarise, the dose coefficients can be calculated using the following equations:

a) Dose coefficients for a protocol with no ATCM (P_C) covering slabs *n* to *m* are given by

$$\left(D_{\mathrm{org}}/\mathrm{CTDI}_{\mathrm{vol}}\right)_{\mathrm{P_C}} = \frac{\sum_{i=n}^{m}\left(D_{\mathrm{org}}/\mathrm{CTDI}_{\mathrm{w}}\right)_{\mathrm{i,0}}\left(\mathrm{CTDI}_{\mathrm{w}}\right)_{\mathrm{i,0}}}{\left(\mathrm{CTDI}_{\mathrm{vol}}\right)_{\mathrm{P_C}}}.$$

b) Dose coefficients for a protocol P_A with angular and longitudinal modulation can be obtained using

$$\left(D_{\mathrm{org}}/\mathrm{CTDI}_{\mathrm{vol}}\right)_{\mathrm{P_A}} = \frac{\sum_{i=n}^{m}\tau_{\mathrm{i}}\left(D_{\mathrm{org}}/\mathrm{CTDI}_{\mathrm{w}}\right)_{\mathrm{i}}}{\sum_{i=n}^{m}\tau_{\mathrm{i}}}(n-m+1),$$

where

$$\left(D_{\mathrm{org}}/\mathrm{CTDI}_{\mathrm{w}}\right)_{\mathrm{i}} = \frac{\left(D_{\mathrm{org}}/\mathrm{CTDI}_{\mathrm{w}}\right)_{\mathrm{i,0}}+\zeta_{\mathrm{i}}\left(D_{\mathrm{org}}/\mathrm{CTDI}_{\mathrm{w}}\right)_{\mathrm{i,1}}}{1+\zeta_{\mathrm{i}}}.$$

c) Dose coefficients for a protocol P_L with longitudinal modulation are given by

$$\left(D_{\mathrm{org}}/\mathrm{CTDI}_{\mathrm{vol}}\right)_{\mathrm{P_L}} = \frac{\sum_{i=n}^{m}\eta_{\mathrm{i}}\left(D_{\mathrm{org}}/\mathrm{CTDI}_{\mathrm{w}}\right)_{\mathrm{i,0}}}{\sum_{i=n}^{m}\eta_{\mathrm{i}}}(n-m+1).$$

5. THE DOSE COEFFICIENT LIBRARY

(110) Following verification, a comprehensive library of dose coefficients for various organs and CT scan parameters was produced. These results were subsequently integrated into a web-based, graphical user interface-based ICRP CT dose calculator which will be described in Section 6, allowing for easy access and application of much of the dose library in medical and radiation protection contexts.

(111) To enable organ dose estimation across diverse CT scan scenarios—accounting for patient age and sex, scan protocol (e.g., coverage and technical parameters), and scanner models, an algorithm that is common to most existing CT organ dose calculation tools can be used. This approach integrates two underpinning methods. First, while absolute organ doses vary significantly among different CT scanners, when normalised by $CTDI_{vol,}$ the coefficient of variation across scanners is reduced to within 5%, allowing for the derivation of scanner-independent dose coefficients i.e. organ doses per $CTDI_{vol}$. Multiplying these coefficients by scanner-specific $CTDI_{vol}$ yields organ doses tailored to the given scanner. These coefficients can be precomputed for various combinations of phantom age, sex, scan region, tube voltage, and beam shaping filter settings of the ICRP reference scanner. Second, organ dose from a helical CT acquisition can be approximated by summing the contributions from a series of adjacent axial scans covering the same anatomical region (Lee et al., 2015). See Section 4.4 for a mathematical description of the derivation of the dose coefficients.

(112) Since the algorithm described in the preceding paragraph derives organ and contributions to effective dose ($E_{103,\#\#M}$ or $E_{103,\#\#F}$) for helical scans by the summation of axial scans, the dose coefficients were calculated for a series of axial scans ranging from the bottom of the feet to the top of the head in each ICRP phantom. As has been described in Section 3, the organ dose coefficients were calculated per CTDI measured free-in-air. As outlined in Section 3, the original z resolution of all ICRP reference phantoms was adopted for axial scan dose calculation, except for the newborn male and female phantoms (Table 3.7). X-ray spectra of 80, 100, and 120 kV with Head and Body filters were applied to the paediatric phantoms, whereas those of 80, 100, 120, and 140 kV with Head and Body filters were used for the adult phantoms.

(113) The dose coefficients described in the preceding paragraph were also determined for the situation when a transform of $(1 + \cos 2\varphi)$ was applied to the incident x-ray fluence as described in Section 4.

(114) $CTDI_{free\text{-}in\text{-}air}$ to $CTDI_w$ conversion coefficients for 80, 100, 120, and 140 kV Head and Body filters for both CTDI head (16 cm) and body (32 cm) phantoms were calculated.

(115) Additionally, the attenuation data described in Section 4 were calculated for each tube voltage and phantom as described in Section 4.

(116) The results of all the calculations described above are included in the electronic supplement, allowing a wide range of operating conditions to be simulated using Eqs (4.2) to (4.13). Additionally, a restricted set of operating conditions can be utilised, without recourse to the data files, using the graphical user interface-based ICRP CT dose calculator that will be further described in Section 6.

5.1. Description of the data files in the dose coefficient library

(117) The library of organ and $E_{103,\#\#M}$ or $E_{103,\#\#F}$ dose coefficients for the ICRP reference paediatric and adult voxel phantoms was generated in the form of a series of tables to be found in the electronic supplement available for download from the current publication. To produce

these data, Monte Carlo calculations for 36,118 MCNPX input files were conducted: 31,566 calculations for the paediatric phantoms and 4552 for the adult phantoms. The number of calculations reflects the number of phantoms, the number of phantom slices and the range of kVs and beam shaping filters used. All input files produced over 2 million tallies (i.e. each input file produced 62 tallies for organ doses and skeletal fluences).

(118) Three sets of data files are provided, each set to be found in a different folder—they are described below.

5.1.1. Tables of dose coefficients per $CTDI_{free\text{-}in\text{-}air}$

(119) For each phantom, two sets of tables are provided as Excel and open-source spreadsheets. There are twelve tables in each set, corresponding to the twelve phantoms utilised. Each table in the first set has the suffix '_notcm' indicating that no tube current modulation has been applied. For example, the table '_adm_dose_notcm' refers to data for the adult male phantom when a constant tube current has been applied i.e. no ATCM. These tables can be found in the folder CONSTANT. Each table in the second set, found in the folder COSINE, has the suffix '_tcm' indicating that the coefficients have been generated using an incident fluence that is proportional to $(1+\cos 2\varphi)$ as described in Section 4.

(120) Each table contains six (for the paediatric) or eight (for the adult) tabs corresponding to the different spectra employed, i.e. 80 kV Head, 80 kV Body, 100 kV Head, 100 kV Body, 120 kV Head, 120 kV Body, 140 kV Head, and 140 kV Body. Note that the140 kV spectra were only used with the adult phantoms. Each tab is structured as follows:

- Column A: slice number
- Column B: z location from the top of the head (cm)
- Column C–AD: slice-specific organ dose coefficients
- Column AE: slice-specific $E_{103,\#\#M}$ or $E_{103,\#\#F}$ coefficients

(121) The number of rows in each data file is equal to the number of axial slices used in the simulation, as shown in Table 3.7. So, for example, there are 222 rows of data in the file for the adult male and 576 in the file for the 10-year-old female. Each row of data provides coefficients of organ absorbed dose per $CTDI_{free\text{-}in\text{-}air}$ in mGy mGy^{-1} for each of the 28 organs and tissues, as well as for $E_{103,\#\#M}$ or $E_{103,\#\#F}$ in mSv mGy^{-1}.

5.1.2. Tables of $CTDI_{free\text{-}in\text{-}air}$ to $CTDI_w$ conversion factors

(122) The folder 'CTDIw' contains one Excel / open-source spreadsheet that includes the $CTDI_w$ per $CTDI_{free\text{-}in\text{-}air}$ conversion factors (in Gy Gy^{-1}) for 80, 100, 120, and 140 kV Head and Body filters, measured in both the $CTDI_w$ Body and $CTDI_w$ Head phantoms. Thus, there are a total of 16 conversion factors. This allows for a greater range of conditions to be computed than is possible using the GUI-based calculator.

5.1.3. Tables of attenuation factors A^{AP} and A^{RLAT}

(123) Four sets of Table are provided as Excel and open-source spreadsheets in the folder 'Attenuation Data'. There is a Table for each of 80, 100, 120, and 140 kV. Each table contains entries for the newborn, 1-year-old, 5-year-old, 10-year-old, 15-year-old male, 15-year-old female, adult male, and adult female phantoms. For each slice of each phantom, values are provided for A^{AP} and A^{RLAT}, and also for ζ_i, τ_i, and η_i (all as described in Section 4). The latter three variables, i.e. ζ_i, τ_i, and η_i can be varied by entering a value for modulation strength q in

the first sheet of each set of Tables. Note, that for the reference Head and Body filters the same attenuation factors are used.

5.2. Illustrative results on contribution to effective dose, $E_{103,\#\#\#}$

(124) The library of dose coefficients was used to prepare an illustrative comparison of the contribution to effective dose, $E_{103,\#\#\#}$ per $CTDI_{free\text{-}in\text{-}air}$ (Sv Gy^{-1}) to demonstrate the impact of different parameters. Note, that ### indicates the age and sex of the phantom, i.e. A, adult, 15-, 10-, 05-, 01-, 00-year-old and M and F, male and female, respectively, as described previously.

(125) The impact of the phantom's sex (male or female) on the contribution of effective dose coefficients, $E_{103,AM}$ and $E_{103,AF}$, for a whole-body scan of the adult male and female phantoms at a tube voltage of 120 kV Body filter is shown in Fig. 5.1. In the curve showing the values for the male phantom, three prominent peaks correspond to contributions from the thyroid ($w_T = 0.04$), breast ($w_T = 0.12$), and testes ($w_T = 0.08$). In the adult female curve, three corresponding peaks arise from the thyroid ($w_T = 0.04$), breast ($w_T = 0.12$), and ovaries ($w_T = 0.08$). These characteristic peaks are consistently observed in subsequent figures (Figs 5.2–5.4). Note that the coefficients in the figures are normalised to a slice thickness of 1 cm, to enable appropriate comparisons.

(126) Fig. 5.2 shows the age-dependent $E_{103,\#\#\#}$ coefficients for a CT whole-body scan with 120 kV Body filter for (a) adult, 10-year-old, and 15-year-old male phantoms and (b) for 5-year-old, 1-year-old, and newborn male phantoms. Fig. 5.3 shows the impact of tube voltage on $E_{103,AM}$ coefficients (Sv Gy^{-1}) for a whole-body scan of the adult male phantom at the tube voltage of 80, 100, and 120 kV. Fig. 5.4 depicts the impact of the beam shaping filter (Head or Body) on the $E_{103,AM}$ coefficients (Sv Gy^{-1}) for the adult male phantom, of which the whole body was scanned at the tube potential of 120 kV.

(127) These figures show the variability of the $E_{103,AM}$ and $E_{103,AF}$ per $CTDI_{free\text{-}in\text{-}air}$, along the z axis of the phantom. The largest variations within the body are observed with phantom sex (Fig 5.1) and age (Fig 5.2). The variation introduced by different tube voltages (Fig 5.3) and beam shaping filters (Fig 5.4) are considerably lower.

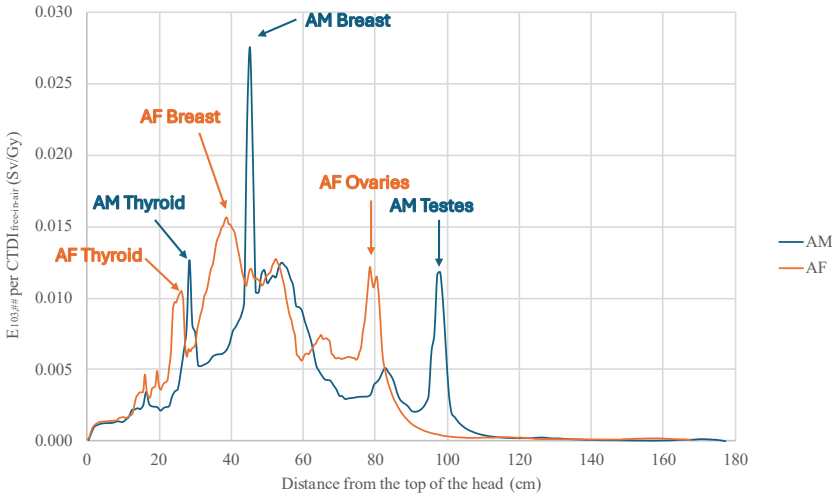

Fig. 5.1. $E_{103,AM}$ and $E_{103,AF}$ per $CTDI_{free\text{-}in\text{-}air}$ (Sv Gy^{-1}) corrected to a slice thickness of 1 cm for whole-body scan with 120 kV Body filter for the adult male (AM) and female (AF) phantoms.

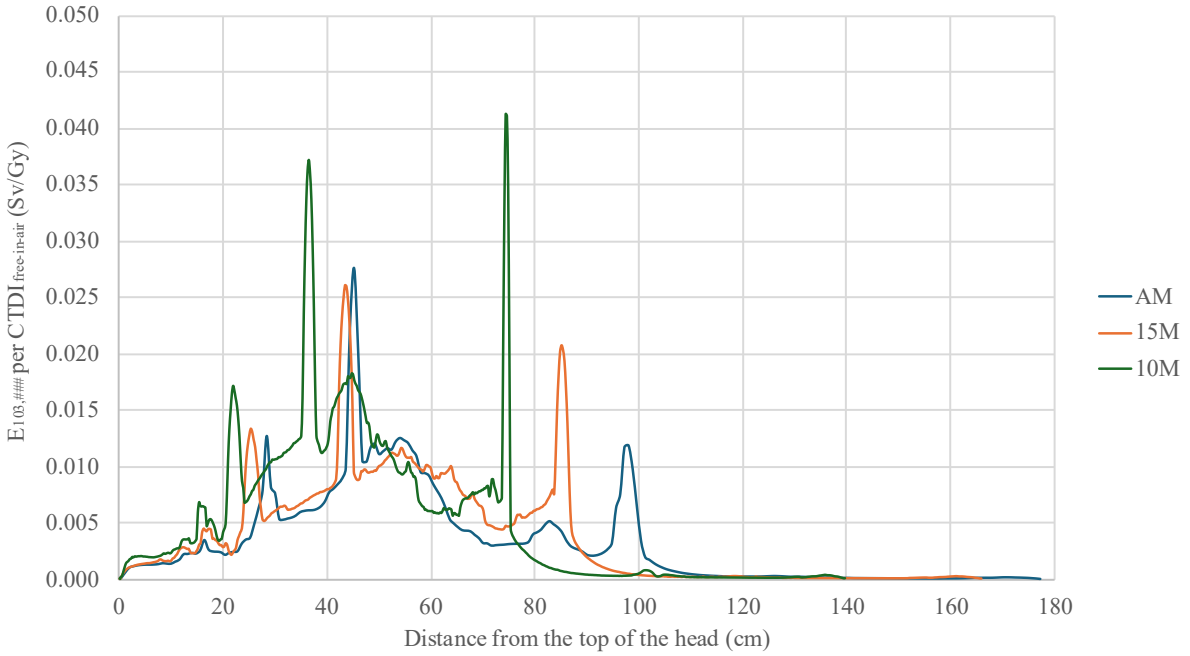

Fig. 5.2a. $E_{103,\#\#\#}$ per $CTDI_{free\text{-}in\text{-}air}$ (Sv Gy^{-1}) corrected to a slice thickness of 1 cm for whole-body scan with 120 kV Body filter. AM, adult male;15M, 15-year-old male; 10M, 10-year-old male.

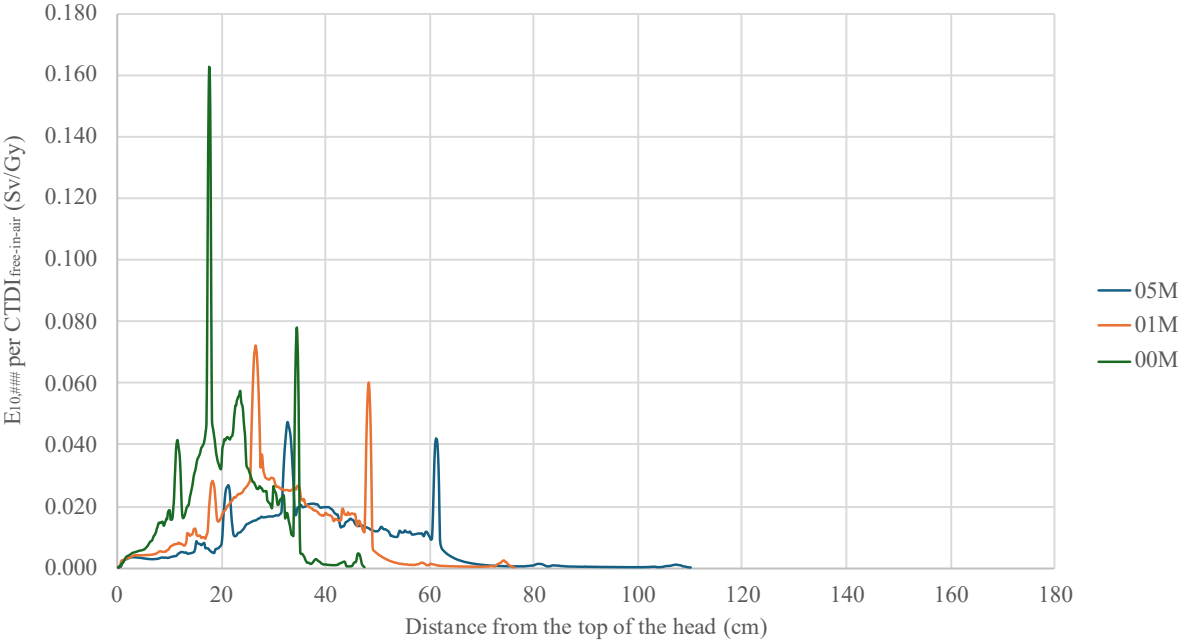

Fig. 5.2b. $E_{103,\#\#\#}$ per $CTDI_{free\text{-}in\text{-}air}$ (Sv Gy^{-1}) corrected to a slice thickness of 1 cm for whole-body scan with 120 kV Body filter. 05M, 5-year-old male; 01M, 1-year-old male; 00M newborn male.

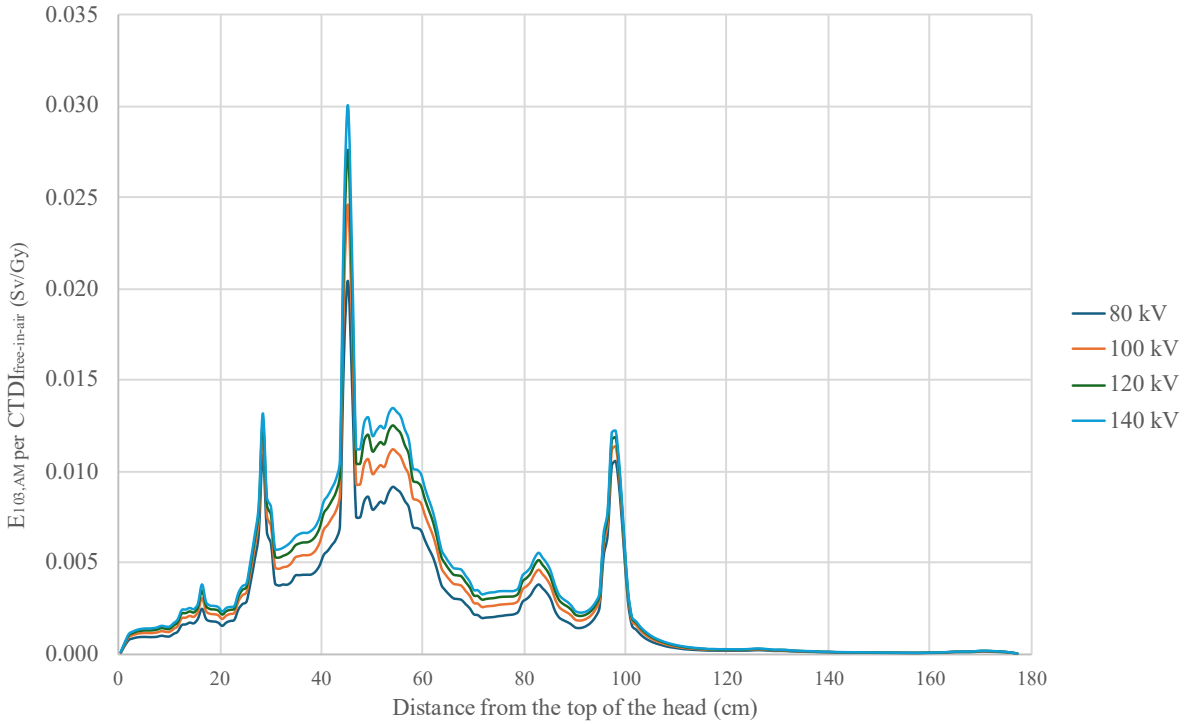

Fig. 5.3. $E_{103,AM}$ per $CTDI_{free\text{-}in\text{-}air}$ (Sv Gy^{-1}) corrected to a slice thickness of 1 cm for whole-body scan of the adult male phantom with 80, 100, 120, and 140 kV and Body filter.

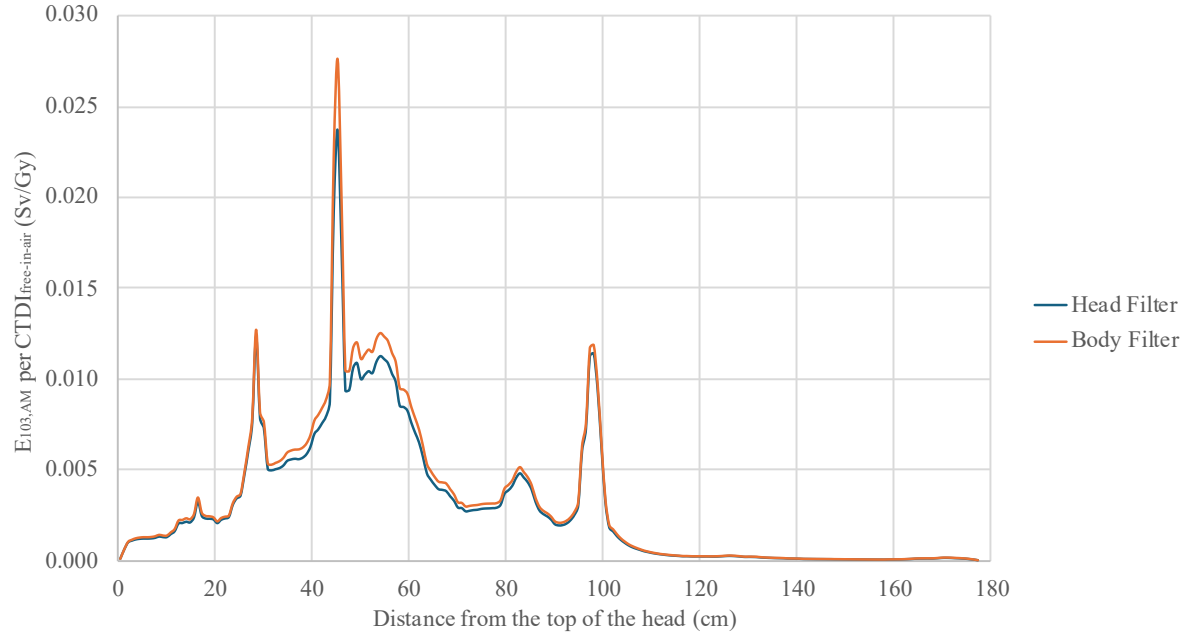

Fig. 5.4. $E_{103,AM}$ per $CTDI_{free\text{-}in\text{-}air}$ (Sv Gy^{-1}) corrected to a slice thickness of 1 cm for whole-body scan of the adult male phantom with 120 kV Head and Body filters.

6. THE GRAPHICAL USER INTERFACE-BASED DOSE CALCULATOR

(128) This section begins by providing three illustrative dose calculations showing how the graphical user interface-based calculator (GUIC) accompanying this publication can be used. The GUIC works by looking up information contained in, or generated from, the data files included in the electronic annex and described in Section 5.1. Note that the dose coefficients were formatted into comma-separated value (.csv) format prior to integration into the calculator, which uses the concept of organ dose per $CTDI_{vol}$ described in Section 5.

(129) The current section then goes on to show how the data files can be manipulated by users to generate their own results using the three examples provided for the GUIC, and another with a different modulation strength.

6.1. Examples demonstrating use of the GUI-based calculator

6.1.1. Example 1

(130) The parameters for this example are shown in Table 6.1. Fig. 6.1 shows the output of the GUIC; note that since the $CTDI_{vol}$ is set to 10 mGy, the resulting doses are ten times the dose coefficients, which are doses normalised to $CTDI_{vol}$ (mGy mGy^{-1}). Note also the use of the scout view display option in this case. The resolution of the phantom, along the long axis, is displayed next to the scan length.

Table 6.1. CT scanner parameters used for Example 1.

Phantom	Tube voltage	Filter	Start position	End position	ATCM	$CTDI_{vol}$ (mGy)
Adult male	120 kV	Body	28 cm	58 cm	None	10

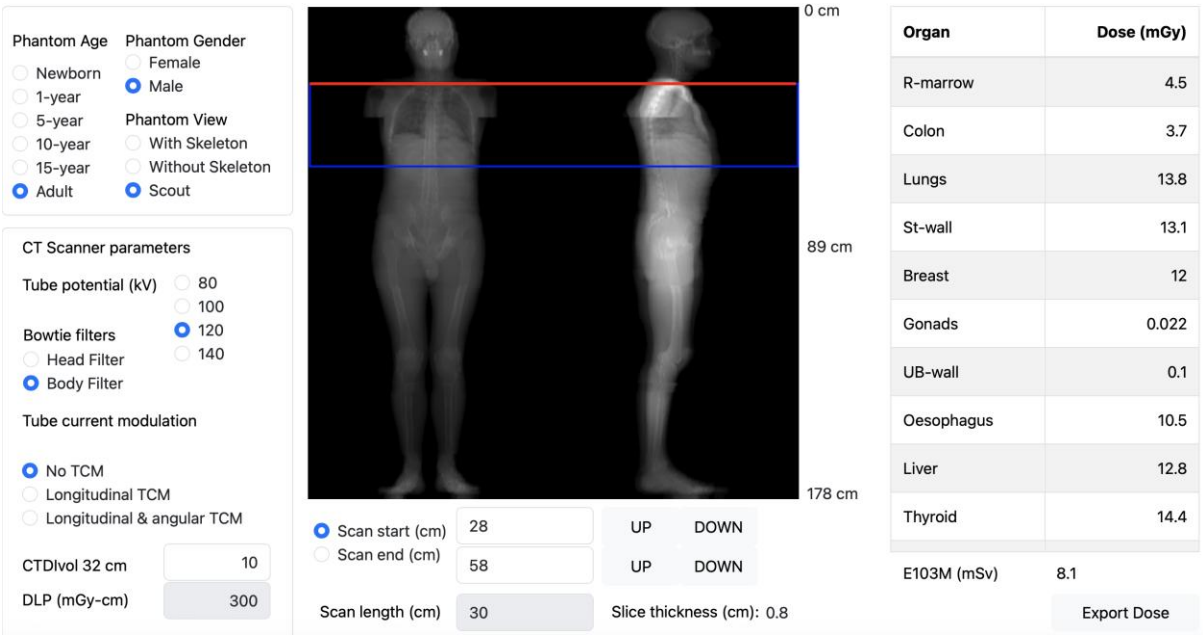

Fig. 6.1. Graphical user interface showing the input parameters and resulting doses based on the scanner parameters described in Table 6.1.

(131) A list of the individual organ doses (in mGy) calculated for the given protocol is shown on the right-hand side of the GUIC. The full list of doses can be inspected by scrolling the table. Also shown is the quantity $\sum w_T \times H_T^M$ described using the notation 'E103M', indicating that this sum was estimated using radiation weighting factors and tissue weighting factors described in *Publication 103* and the dose coefficients for the male phantom as described in Paragraph (23). Use of the 'Export Dose' button opens a new tab in the browser that displays a tabulation of the organ doses and the quantity $\sum w_T \times H_T^M$. These data can be copied and pasted into a user's own applications using for example a spreadsheet.

6.1.2. Example 2

(132) The parameters for this example are almost the same as those for Example 1, the only change being that longitudinal modulation is applied. Note that the method adopted here is provided for educational use only and does not represent the implementation of any manufacturer's approach—see Section 4. The parameters in the example are shown in Table 6.2. Fig. 6.2 shows the GUIC output for the example. Note that in this case visualisation is performed using the 'Without Skeleton' view.

Table 6.2. CT scanner parameters used for Example 2.

Phantom	Tube voltage	Filter	Start position	End position	ATCM	$CTDI_{vol}$ (mGy)
Adult male	120 kV	Body	28 cm	58 cm	Longitudinal	10

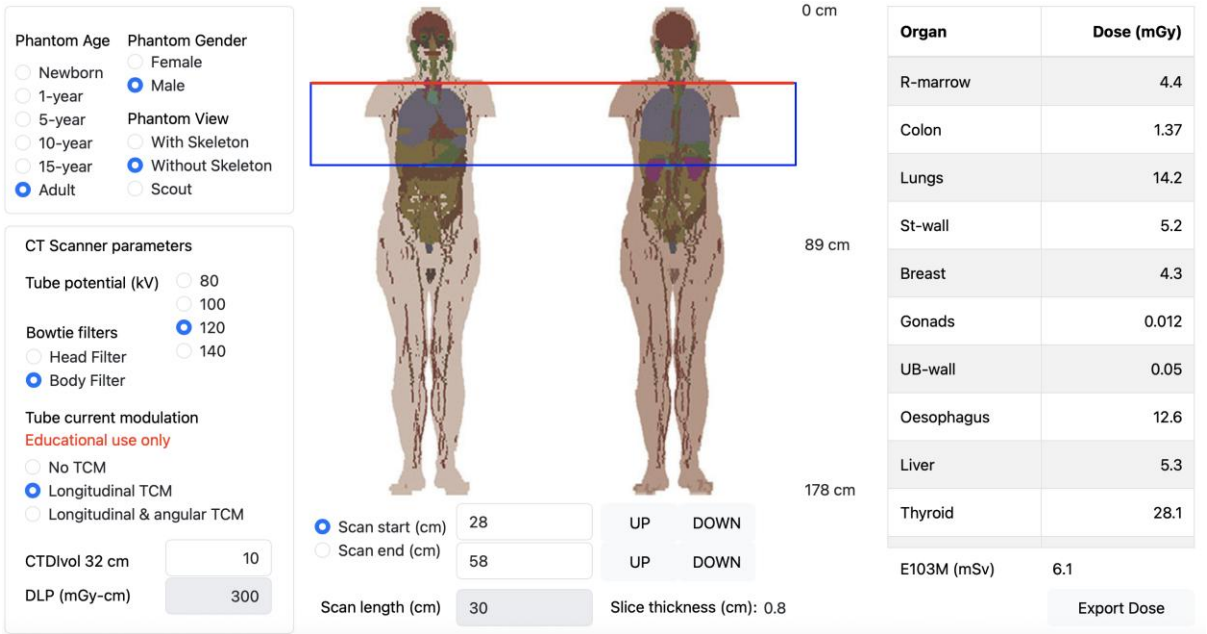

Fig. 6.2. Graphical user interface showing the input parameters and resulting doses based on the scanner parameters described in Table 6.2.

6.1.3. Example 3

(133) The parameters for this example again almost replicate those of Example 1, except that full (i.e. longitudinal and angular) modulation is applied. Note again that the method adopted here is provided for educational use only and does not represent the implementation of any manufacturer's approach—see Section 4. As described in Section 4, the only modulation strength considered in the GUIC is 0.75; however, users can use their own values of modulation

strength using the method described later in this section (see Section 6.2). The parameters in this example are shown in Table 6.3. Fig. 6.3 shows the GUIC output for the example. Note that this example shows the GUIC when visualisation is performed using the 'With Skeleton' view.

Table 6.3. CT scanner parameters for Example 3.

Phantom	Tube voltage	Filter	Start position	End position	ATCM	$CTDI_{vol}$ (mGy)
Adult male	120 kV	Body	28 cm	58 cm	Longitudinal and angular	10

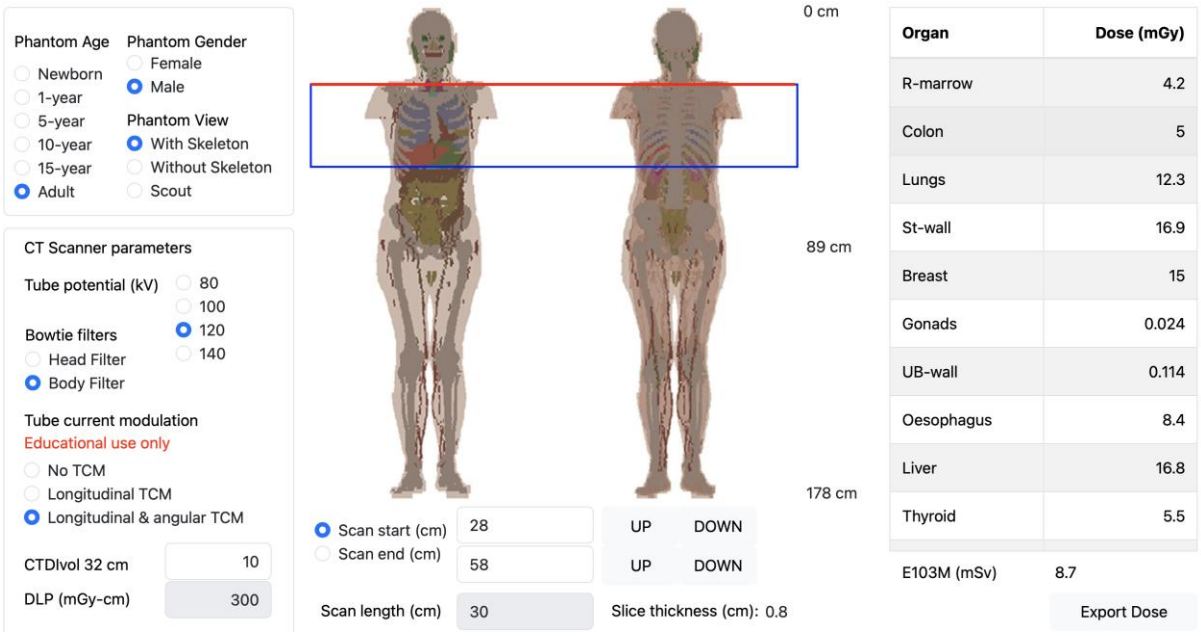

Fig. 6.3. Graphical user interface showing the input parameters and resulting doses based on the scanner parameters described in Table 6.3.

(134) Table 6.4 shows the results from all three examples obtained using the 'Export Dose' button of the GUIC. The table shows the change in doses resulting from the application of ATCM. As might be expected, some doses have increased and some have decreased and there are differences between the results obtained from two types of ATCM (longitudinal only vs longitudinal and angular). It is important to be aware that application of dose modulation should not *ipso facto* be expected to reduce a dose coefficient. For the same $CTDI_{vol}$ some body parts receive more dose with ATCM and some less dose than without ATCM, so the dose coefficients when ATCM is employed may be higher or lower than when it isn't. However, it should be remembered that when ATCM is used, the average $CTDI_{vol}$ over the entire scan (generally the quantity displayed on the scanner console), will usually be lower than in the constant current case. Therefore, in practice, values of $CTDI_{vol}$ and organ doses tend to be lower when ATCM is employed than when it is not, provided that the same image quality is required. See for example *Publications 154* (ICRP, 2023) and *160* (ICRP, 2025), (van Straten et al., 2009; IAEA, 2014; Papadakis and Damilakis, 2020).

Table 6.4. Results of Examples 1, 2, and 3 obtained using the 'Export Dose' function with a displayed $CTDI_{vol}$ of 10 mGy.

Organ	Dose with no ATCM (mGy)	Dose with longitudinal modulation only (mGy)	Dose with longitudinal and angular ATCM (mGy)
R-marrow	4.5	4.4	4.2
Colon	3.7	1.24	5.1
Lungs	13.8	14.2	12.2
St-wall	13.1	4.8	17
Breast	12	4.1	15.1
Testes	0.022	0.011	0.024
UB-wall	0.1	0.04	0.115
Oesophagus	10.5	12.7	8.3
Liver	12.8	4.9	17
Thyroid	14.4	28.8	5.3
Endost-BS	2.44	2.55	2.23
Brain	0.212	0.37	0.14
S-glands	0.9	1.58	0.57
Skin	2.51	2.58	2.51
Adrenals	11.8	4.1	15
ET	0.73	1.26	0.46
GB-wall	10.8	3.6	14.3
Ht-wall	14.6	10.9	14.3
Kidneys	8.3	2.69	10.7
Lymph	5.6	5	5.5
Muscle	2.76	3.14	2.55
O-mucosa	0.62	1.03	0.42
Pancreas	9.3	3.08	11.5
Prostate	0.05	0.021	0.05
SI-wall	2.27	0.8	2.93
Spleen	13.9	5.5	19.1
Thymus	15.6	31.6	7.3
Lens	0.259	0.4	0.19
$E_{103,AM}$ (mSv)	8.1	6	8.7

R-marrow, red bone marrow; ST-wall, stomach wall; UB-wall, urinary bladder wall; Endost-BS, skeletal endosteum; S-glands, salivary glands; ET, extrathoracic region; GB-wall, gall bladder wall; Ht-wall, heart wall; O-mucosa, oral mucosa; SI-wall, small intestine wall; Lens, lens of the eye.

6.2. Worked examples using the data tables

(135) The examples presented in this section show how the data tables can be used to derive results without recourse to the GUIC by directly implementing the equations provided in Section 4. They confirm that identical results are obtained whether the GUIC is employed or not. To achieve this, the examples employ the same methodology for defining the start and finish positions within the phantom slice as is used by the GUIC.

(136) It is important to note that each phantom has a particular slice width (resolution) and the calculations reported in the GUIC do not include any inter or intra slice interpolation. The GUIC looks up values directly from the data files and the start position specified is converted to phantom slice numbers by rounding down the result of dividing each physical position in cm by the phantom resolution in cm and adding one (since the first row of data is row 1, not

row zero). In a similar manner, the end position is converted to a phantom slice by rounding up, but without the subsequent addition of one.

(137) For example, consider the male phantom and the example used above. When the start position selected in the GUIC is 28 cm from the top of the phantom i.e. head, the first slice in the phantom that the GUIC takes data from, is number 36. Inspection of the data files shows that slice number 36 has a central position of 28.4 cm, thus covering the range between 28.0 and 28.8 cm from the top of the phantom. The GUIC includes the organ doses of this slice in the calculation. Using the approach outlined above, an end position of 58 cm from the top of the phantom, would correspond to slice 73. Inspection of the data files shows that slice number 73 has a central position of 58 cm, thus covering the range between 57.6 to 58.4 cm from the top of the phantom. The GUIC includes the organ doses of this slice as if the whole slice were in the scan range, and not just part of it.

(138) Users can adopt more sophisticated approaches than that used in the GUIC by direct manipulation of the data in the data files.

6.2.1. Example 4

(139) This first example shows how to use the data from the tables to evaluate the organ doses for the case shown in 6.1 above. The steps are as follows and involve a direct calculation of Eq. (4.5):

a) Open the spreadsheet 'adm_dose_notcm' and choose the tab '120body'.

b) Open the spreadsheet 'ctdiw_per_ctdiair'.

c) Divide every value in 'adm_dose_notcm/120_body' by 0.37742, the value in cell B9 of 'ctdiw_per_ctdiair'. This results in a table of organ doses per $\mathrm{CTDI_w}$. This is the table denoted $\left(D_{\mathrm{org}}/\mathrm{CTDI_w}\right)_{\mathrm{i,0}}$ in Section 4.

d) Identify the first slice and last slices in the range from 28 cm to 58 cm. These are slices 36 and 73.

e) Sum the coefficients of the table $\left(D_{\mathrm{org}}/\mathrm{CTDI_w}\right)_{\mathrm{i,0}}$ for each organ from slice 36 to slice 73.

f) The 5 steps above are a direct implementation of Eq. (4.5), $\left(D_{\mathrm{org}}/\mathrm{CTDI_{vol}}\right)_{\mathrm{P_C}} = \sum_{i=n}^{m}\left(D_{\mathrm{org}}/\mathrm{CTDI_w}\right)_{\mathrm{i,0}}$.

(140) The results obtained using this approach are as shown in Table 6.5 and can be seen, as expected, to be the same as those determined using the GUIC (allowing for rounding errors) and shown in Table 6.4.

6.2.2. Example 5

(141) The second example replicates Example 2 above, but by direct calculation of Eq. (4.13). The steps in the calculation are as follows:

a) Replicate steps a) to d) of Example 4.

b) Open the tab 'AttenuationData_120kV/adult male' and ensure that the global modulation strength is set to 0.75.

c) Multiply every value in the table $\left(D_{\mathrm{org}}/\mathrm{CTDI_w}\right)_{\mathrm{i,0}}$ by the corresponding value of η_{i} found in column H of 'AttenuationData_120kV/adult male'. For example, each value in slice 1 is multiplied by 5.47×10^{-3}, each value in slice 2 by 7.23×10^{-3} and so on.

d) Sum the coefficients for each organ from slice 36 to slice 73 in the table generated in step c). This is $\sum_{i=n}^{m} \eta_i \left(D_{org}/\mathrm{CTDI_w}\right)_{i,0}$.

e) Sum the values of η_i from slice 36 to 73. This is 15.55.

f) Divide the results obtained for each organ in step d) by 15.55 and then multiply by (73 − 36 + 1 = 38).

(142) The above 6 steps describe a direct implementation of Eq. (4.13), i.e. $\left(D_{org}/\mathrm{CTDI_{vol}}\right)_{P_L} = \frac{\sum_{i=n}^{m} \eta_i \left(D_{org}/\mathrm{CTDI_w}\right)_{i,0}}{\sum_{i=n}^{m} \eta_i} (n - m + 1)$. The results using this approach are as shown in Table 6.5 and can be seen to be the same as those in Table 6.4 from Example 2, allowing for rounding errors.

6.2.3. Example 6

(143) Example 6 has the same parameters as in Example 3 above, using direct calculation of Eq. (4.11). The steps in the calculation are as follows:

a) Replicate steps a) to d) of Example 4.

b) Divide every value in 'adm_dose_tcm/120_body' by 0.37742, resulting in a second table of organ doses per $\mathrm{CTDI_w}$. This is $\left(D_{org}/\mathrm{CTDI_w}\right)_{i,1}$ as described in Section 4.

c) Using values of ζ_i from tab 'AttenuationData_120kV/adult male' combine the two tables to form a third table $\left(D_{org}/\mathrm{CTDI_w}\right)_i$ containing the values of the term $\frac{\left(D_{org}/\mathrm{CTDI_w}\right)_{i,0} + \zeta_i \left(D_{org}/\mathrm{CTDI_w}\right)_{i,1}}{1+\zeta_i}$.

d) Values of τ_i can then be obtained from 'AttenuationData_120kV/adult male' and combined with the above in the summation range slice 36 to 73 to generate $\left(D_{org}/\mathrm{CTDI_{vol}}\right)_{P_A} = \frac{\sum_{i=n}^{m} \tau_i \left(D_{org}/\mathrm{CTDI_w}\right)_i}{\sum_{i=n}^{m} \tau_i} (n - m + 1)$ where n – m + 1 = 38, as before.

(144) The results of this calculation are shown in Table 6.5 and are the same as those in Table 6.4 from Example 3, allowing for rounding errors.

6.2.4. Example 7

(145) This example is the same as Example 6, with the exception that a different modulation strength of 0.5 is used. The only difference from the calculation described in Example 6 is that when the spreadsheet 'AttenuationData_120kV' is opened, the entry for modulation strength in tab 'Strength' is changed from 0.75 to 0.5. The calculation is carried out exactly as shown in Example 6, using modified values of ζ_i and τ_i obtained by altering the strength coefficient. Results are provided in Table 6.5.

Table 6.5. Results of Examples 4 to 7 using the tables of the electronic supplement for the calculation.

Organ	Dose with no ATCM (mGy)	Dose with longitudinal ATCM only (mGy)	Dose with longitudinal and angular ATCM, strength 0.75 (mGy)	Dose with longitudinal and angular ATCM, strength 0.5 (mGy)
R-marrow	4.49	4.37	4.23	4.23
Colon	3.69	1.24	5.06	4.64
Lungs	13.81	14.24	12.23	12.52
St-wall	13.10	4.79	17.04	15.85
Breast	12.01	4.05	15.08	14.21
Testes	0.02	0.01	0.02	0.02
UB-wall	0.10	0.04	0.11	0.11
Oesophagus	10.52	12.70	8.32	8.69
Liver	12.82	4.91	16.96	15.69
Thyroid	14.39	28.84	5.34	7.11
Endost-BS	2.44	2.55	2.23	2.25
Brain	0.21	0.37	0.14	0.16
S-glands	0.90	1.58	0.57	0.66
Skin	2.51	2.58	2.51	2.52
Adrenals	11.81	4.08	15.00	14.07
ET	0.73	1.26	0.46	0.53
GB-wall	10.83	3.61	14.27	13.24
Ht-wall	14.62	10.93	14.31	14.33
Kidneys	8.28	2.69	10.72	10.01
Lymph	5.60	4.98	5.55	5.50
Muscle	2.76	3.14	2.55	2.61
O-mucosa	0.62	1.03	0.42	0.48
Pancreas	9.28	3.08	11.54	10.91
Prostate	0.05	0.02	0.05	0.05
SI-wall	2.27	0.80	2.92	2.73
Spleen	13.89	5.49	19.14	17.47
Thymus	15.60	31.55	7.31	8.91
Lens	0.26	0.40	0.19	0.21
$E_{103,AM}$ (mSv)	8.12	4.37	8.69	8.43

R-marrow, red bone marrow; ST-wall, stomach wall; UB-wall, urinary bladder wall; Endost-BS, skeletal endosteum; S-glands, salivary glands; ET, extrathoracic region; GB-wall, gall bladder wall; Ht-wall, heart wall; O-mucosa, oral mucosa; SI-wall, small intestine wall; Lens, lens of the eye.

7. UNCERTAINTIES, VARIABILITY, AND LIMITATIONS

(146) Computed tomography is a powerful diagnostic tool that delivers 3-dimensional high-resolution images of internal body structures. As described in the introduction to this publication, there are many reasons why it is important to be able to estimate organ doses resulting from CT scans. This publication has described the development of the ICRP reference scanner and associated dose coefficient library that will permit such estimations to be carried out. As previously outlined, the scope is confined to 'conventional' CT; technologies such as photon counting CT or spectral CT, whether using dual detectors or kV switching have not been considered.

(147) The dose coefficients of this publication were calculated for the reference phantoms at reference ages (newborn, 1-, 5-, 10-, 15-year-old, and adult) (ICRP, 1995) and the ICRP reference scanner. Within the scope of their intended use, these coefficients are reference values and as such are fixed and specified with no uncertainty (JCGM, 2012), independent of the fact that the basis of these values may include uncertainties. In the context of the present case, the accuracy of the dose coefficients provided is limited by uncertainties in the physical input parameters, such as interaction cross sections and deviations of the particle transport simulation from the real exposure situation, for example the source geometry i.e. CT scanner. A discussion of the uncertainties encountered in the calculation of the reference coefficients can be found in section 7.4 A detailed discussion on the interpretation of reference dose coefficients can be found in *Publication 163* (ICRP, 2025).

(148) This section outlines the uncertainties, variability, and limitations associated with using the data in the dose library. They are shown in Tables 7.1 and 7.2. It should be noted that uncertainty and variability are distinct concepts, uncertainty referring here to lack of exact knowledge, whereas variability refers here to quantitative differences between different members of a population and different exposure conditions. The glossary to the 2019 UNSCEAR report provides further information on this topic (UNSCEAR, 2020).

7.1. Uncertainty in doses calculated using the dose coefficients

(149) The organ and effective dose coefficients presented in this publication are valid for the reference phantoms and the ICRP reference scanner described. They are subject to uncertainties when applied to represent any specific CT scanner. These uncertainties arise from several factors, including differences in CT scanner geometries, discrepancies in beam shaping filter design and materials, difference in photon spectra (resulting from, for instance, different beam filtration), differences in $CTDI_{vol}$ calibration and uncertainty in kV calibration. The influence of these factors on the uncertainty of calculated organ and effective doses is examined in the following discussion

(150) In Annex A comparisons are made for the adult male and female reference phantoms for the ICRP reference scanner and those obtained for the individual scanners listed in Table 3.1. Related figures in the electronic supplement present graphical comparisons between organ absorbed doses — plus $E_{103,\mathrm{AM}}$ and $E_{103,\mathrm{AF}}$ for all the operating conditions listed in Table 3.1. These estimates, obtained for each slice along the long dimension of the phantoms, can be used as a visual indication of the variation between results from the ICRP reference scanner and those from each of the scanners used in its development.

(151) In practice, one of the largest contributions to the uncertainty in the determination of organ doses calculated using the coefficients is the uncertainty associated with the display of $CTDI_{vol}$ on the CT console. This can amount up to 20% or more according to some studies

(Stratis et al., 2014; Cannillo et al., 2018; Fehrmann et al., 2020; Forss et al., 2021) The current IEC standard (IEC 61223-3-5) for acceptance and constancy tests of CT devices specifies that the measured $CTDI_w$ value is allowed to deviate from the displayed value by ±20% or ±1 mGy, whatever is larger. Factors of 20% (EANM, 2017; AAPM, 2019) and 15% (Iball et al., 2016) have previously been recommended for quality control purposes. A relative standard deviation (RSD, defined as the standard deviation divided by the mean) of ±20% is the value chosen for use in this analysis.

(152) The other major uncertainty to be considered is the uncertainty introduced by utilising the ICRP reference scanner to estimate doses from any other scanner. An estimate of this uncertainty was made in the following way.

(i) The effective dose for all simulated scanners and operating conditions was calculated by averaging the gender specific effective dose coefficients $E_{103,\mathrm{AM}}$ and $E_{103,\mathrm{AF}}$

(ii) The effective dose per $CTDI_{w,32cm}$ was then calculated and averaged for

a. All operating conditions considered together

b. Scanners grouped by beam shaping filter (Head or body)

c. Scanners grouped by applied kV (80,100,120,140)

d. Scanners grouped by beam shaping filter and applied kV (8 categories)

(153) As an example of the way the data is distributed, Fig. 7.1 shows, for the adult female phantom, the quantity $E_{103,\mathrm{AF}}$divided by $CTDI_{w,32cm}$ together with the standard deviation, as a function of distance along the long axis of the phantom. Graphs are presented for the Body beam shaping filter and the four tube voltage region. Analysis of the data presented in Fig. 7.1 shows that there are statistically significantly differences between $E_{103,\mathrm{AF}}$ calculated at 80 kV and 140 kV for large parts of the trunk.

(154) For all the scanners grouped together, the RSD was 0.117. Grouping by the two beam shaping filters resulted in a maximum RSD over the two groups of 0.116. Grouping by the four applied kVs resulted in a maximum RSD of 0.067. The grouping chosen in the implementation of the reference scanner, i.e. by beam shaping filter and kV resulted in a maximum RSD of 0.064, or ±6.4%

(155) A further contribution to the total uncertainty is the tolerance associated with the kV displayed on the CT console. A value of 2kV or approximately ±2% is commonly considered to be acceptable (AAPM, 2019). To determine the resultant uncertainty in $E_{103,A\#}$, its dependence (when normalised to $CTDI_{w,32}$) on tube voltage was investigated. In the ICRP reference scanner, the largest differences in $E_{103,A\#\#}$ per $CTDI_{w,32}$ occur between 80 and 100 kV. Accordingly, the ratio of $E_{103,A\#}$ per $CTDI_{w,32cm}$ for 100 kV divided by that at 80 kV was calculated per slice and averaged over the trunk region for the adult male and female phantoms using both Body and Head beam shaping filters. The largest value of this ratio obtained was 1.18 (i.e. a difference of 18%) using the combination of adult male phantom and Head filter. When the Body filter was used, the maximum value of the ratio was found to be 1.15, again in the adult male phantom. Since these values correspond to a tube-voltage change of 20 kV, it is reasonable to suppose that a variation of 2kV will result in a difference in $E_{103,A\#}$ of 1.8% or less. The implication is that for an uncertainty of ±2 kV in tube voltage the estimated uncertainty in $E_{103,A\#}$ per $CTDI_{w,32}$ is less than1.8%, which can conservatively be rounded to ±2%.

(156) Uncertainties due to the beam shaping filter, such as position, shape, material, density, and the focus to centre of rotation distances have already been taken into account in the analysis described above.

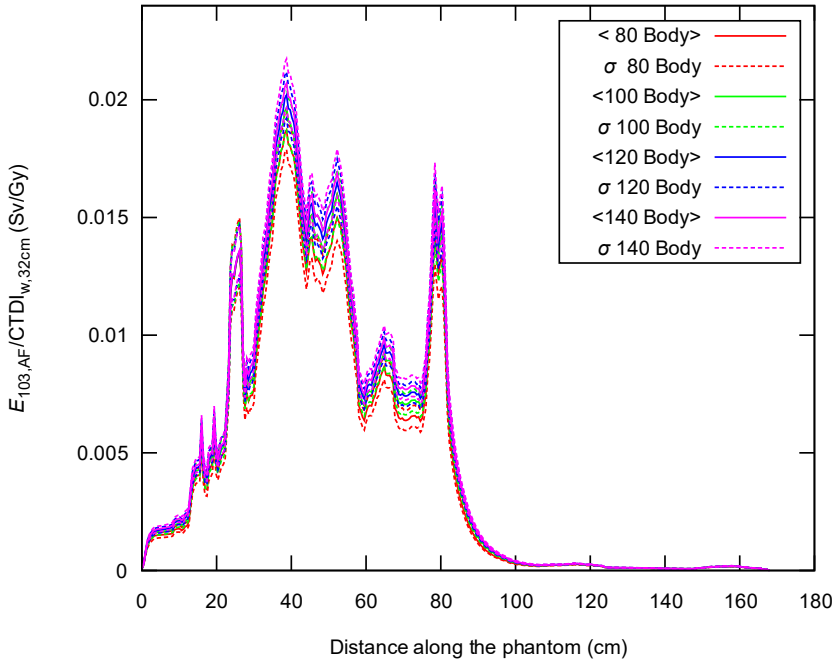

Fig. 7.1. $E_{103,\mathrm{AF}}$ normalised to $\mathrm{CTDI}_{\mathrm{w,32cm}}$ as a function of distance along the long axis of the phantom. CT scanners have been grouped according to 4 tube voltage regions, namely, 80, 100, 120, and 140 kV. The solid lines indicate the average $E_{103,\mathrm{AF}}$ / $\mathrm{CTDI}_{\mathrm{w,32cm}}$ and the dashed lines below and above the solid lines indicate the average − standard deviation and the average + standard deviation, respectively. Note that the top of the head is positioned at 0 cm and that the distance increases going towards the bottom of the feet.

(157) Taking the three sources of uncertainty together, i.e. RSDs of a) ±20%, in displayed $\mathrm{CTDI}_{\mathrm{vol}}$ on any individual scanner, b) ±6.4% due to the ICRP reference scanner and c) ±2% resulting from the kV tolerance results in a standard uncertainty (RSD) of ±21%, and an overall expanded uncertainty of ±42% (k=2), a figure dominated by the magnitude of the uncertainty associated with the $\mathrm{CTDI}_{\mathrm{vol}}$ display. To be clear, this is the uncertainty in the estimate of a dose to a reference phantom determined using the dose coefficients applied to any specific scanner.

7.2. Potential limitations to, and variations encountered in, the practical application of dose coefficients

(158) The reference dose coefficients provided have been calculated for male and female reference adults and children corresponding to the reference ages, as defined in *Publication 89* (ICRP, 2002), and as these are reflected at the ICRP reference voxel phantoms of *Publication 110* and *143* (ICRP, 2009, 2020b). Note, that although the anatomy of these reference individuals i.e. height and masses, densities, and elemental compositions of the organs, is defined in *Publication 89*, there is no reference location of the organs.

(159) The reference dose coefficients cannot be used to estimate doses to an individual patient; however, they can give an indication of their magnitude. In this context it must be noted that the ICRP reference phantoms represent standard body sizes of Caucasians (ICRP, 2002). They cannot fully capture the variability in patient body habitus and doses estimated using them should not be considered as being representative of individual patient doses. Several studies have attempted to quantify the associated uncertainties, which strictly speaking, are expressing the variability, with results indicating that organ dose estimates can vary by 20% to

over 100%, depending on the method used and the clinical scenario. For example, Lee et al. (2017) reported that lung doses based on reference phantoms may be underestimated by up to 50% in underweight patients and overestimated by up to 200% in overweight patients.

(160) Caution must be exercised when comparing the doses obtained using the dose coefficients reported in this publication with those obtained using other simulation methods, mainly because of the influence of phantom design. Different types of computational phantoms, for example, voxel or mathematical, can lead to different estimations of any dose coefficient. Lee et al. (Lee and Bolch, 2006) compared organ doses for paediatric CT examinations with voxel and stylised phantoms and found significant dose discrepancies in some organs, especially small and irregularly shaped ones such as thyroid and stomach. The study showed that voxel phantoms yield more accurate dose coefficients, especially in small organs whilst stylised phantoms may underestimate dose in regions near bone or lung interfaces. One of their conclusions was that differences between phantom types could reach up to 30% in some organs. Other studies have shown that the position of the organs in relation to the field, can result in different values for dose coefficients. One study of simulated CT examinations which employed a library of different sizes of (non-reference) phantoms, based on the scaling of a limited number of size-adjusted individuals, revealed significant differences of up to 50% in the colon dose coefficient (Martin et al., 2021).

(161) It is worth noting that when the authors of this publication compared organ dose coefficients for the voxel-type (ICRP, 2010) and mesh-type (ICRP, 2020) ICRP reference adult female phantoms using the ICRP reference scanner, no significant differences were found.

(162) Different scanning protocols (e.g., chest and abdominal CT protocols) result in varying dose distribution and are dependent on many factors. For this reason, this publication does not make recommendations for specific clinical protocols or present results for particular clinical indications. Care must be taken when using the reference scanner to compare the results from differing sources to ensure that equivalent scan conditions and assumptions are being compared. Inaccuracies in recording or modelling scanner parameters introduce another layer of uncertainty.

(163) Variations in tube current modulation (ATCM) algorithms among different CT scanner manufacturers can lead to significant uncertainties in dose estimation. Each manufacturer implements unique ATCM strategies, many of which are proprietary and not publicly disclosed, making it challenging to replicate or model them accurately. As a result, it is not feasible to develop a universally applicable algorithm that mimics all existing modulation techniques. To address this limitation, a generic and simplified ATCM algorithm was developed for this work. The aim was to describe the general behaviour of ATCM across scanners, not to facilitate comparison with more specific ATCM implementations.

(164) Some scanners have dedicated organ reduction protocols for peripheral organs and employ tube current reduction for those organs which are near the tube. Additionally, for small organs, like the lens of the eye, some scanners allow helical protocols to be applied in which the tube is opposite the organ at risk as it passes the organ z-position and the pitch is high. The ICRP reference CT scanner is not suitable for calculating organ doses for either of the above types of protocol, as the calculated doses for the axial slices are for uniform rotational exposure combined with $(1+\cos(2\varphi))$ rotational exposures. In the case of the organ dose reduction methods, a $(1+\cos(\varphi))$ like rotational exposure is needed and this has not been implemented in this work. Similarly, for small organs, helical-specific exposures are required but these have not been included in this work. It is worth noting that in the case of eye lens dose reduction, organ-based tube current modulation can result in a 30% dose reduction, but gantry tilting can be more effective by placing the eye lens outside the exposure field, achieving a 75% reduction of eye lens dose (Nikupaavo et al., 2015). Gantry tilting is not included in the current ICRP CT dose calculator.

Table 7.1. Summary of the uncertainties contributing to doses estimated using the dose coefficients.

Category	Definition	Source	Quantified value
$CTDI_{vol}$ display accuracy	Lack of exact knowledge about the true value (e.g., measurement or calibration errors)	Console display calibration	20% or ±1 mGy whatever is larger
Scanner geometry & beam filters	Modelling limitations (e.g., beam shaping filter, source geometry)	Differences between ICRP reference and real scanners	6.4% (RSD)
kV tolerance	Displayed kV value	Tube voltage calibration	2% (±2 kV)
Combined uncertainty in dose	Aggregated uncertainty from the different components	All of the above	21% (standard) 42% (expanded, k=2)

Table 7.2. Summary of the potential causes of variations between different estimates of dose.

Category	Definition	Source	Quantified value
Patient body habitus	Quantitative differences between individuals (e.g., underweight vs. overweight patients, organ location)	Differences in patient height, weight, anatomy	20% to >100%
Phantom type	Differences in dose estimates due to phantom design (e.g., voxel vs. mathematical models)	Voxel vs. stylized phantoms	Up to 30%
Organ positioning	Differences in dose due to organ position (e.g., colon dose coefficient)	Organ location relative to scan field	Up to 50%
Protocols	Differences between protocol definitions (e.g. differing start and stop positions for scanning protocols with apparently the same name such as chest or pelvis)	Use of differing parameters	Not quantifiable
ATCM algorithms	Proprietary algorithms for automatic tube current modulation	Manufacturer-specific tube current modulation	Not quantifiable
Special protocols	Protocol-specific adjustments	Organ-specific dose reduction (e.g., current modulation, gantry tilting)	30%–75% reduction

7.3. Uncertainties in dose coefficients calculated using Monte Carlo methods

(165) As has already been explained, the uncertainty in the reference dose coefficients is, by definition, zero. However, for the sake of completeness, the following discussion provides an indication of the uncertainties associated with the Monte Carlo calculations used in the derivation of the reference dose coefficients.

(166) Monte Carlo methods are particularly useful for simulating radiation transport through the body to model complex physical processes, accounting for the anatomy of the body, geometry of the radiation source, and the physical interactions of ionising radiation such as x-rays with tissues. These simulations model the stochastic nature of radiation interactions on a particle-by-particle basis, allowing for precise dose calculations.

(167) Since Monte Carlo simulations are based on probabilistic methods, there is always some degree of uncertainty in the results. Statistical uncertainties arise due to the inherent random nature of the particle transport process, and these are quantified through confidence intervals or standard deviations. These uncertainties are strongly influenced by the number of particle histories used in the simulation. In this publication, a total of 100 million particle histories per slice were employed to reduce Monte Carlo errors to 5% for organs located near scan boundaries, where dose estimates are typically more variable.

(168) Other sources of uncertainty in the Monte Carlo calculations are uncertainties in cross sections, elemental compositions, densities of the organs and tissues, and inadequacies in the description of the photon source. For example, the uncertainties in the determination of photon cross sections have been estimated to be of the order of 5% below 5 keV and 2% up to 10 MeV (Hubbell and Seltzer, 1995).

7.4. The interpretation of effective dose and its limitations

(169) For the calculation of $\sum_T w_T \times H_T^M$ and $\sum_T w_T \times H_T^F$ given in this publication, the current ICRP System of Radiological Protection (ICRP, 2007b) was applied, using a simplified set of tissue weighting factors, based on sex- and age-averaged relative detriment values and specifies only two nominal detriment values: 5.7×10^{-2} Sv^{-1} for the whole population and 4.2×10^{-2} Sv^{-1} for adults (ICRP, 2007b). Thus, recognised differences in detriment and relative detriment (the contribution of the various organs and tissues to total detriment) as a function of age at exposure are not considered, other than in the differences between the two nominal detriment values (ICRP, 1991a, 2007b). Thus, differences in effective dose coefficients as a function of age shown in this publication relate only to differences in physical size and organ masses and do not address differences in detriment per Sv. Similarly, differences in organ absorbed dose coefficients do not inform on differences in stochastic risk per Gy as a function of age at exposure.

(170) It is estimated that the age at exposure introduces an approximate variation up to a factor of three, therefore effective dose can be considered an approximate indicator of the possible risk. This approximation is usually sufficient to inform judgements and the assessment of possible risks in the medical uses of radiation and communication with patients (ICRP, 2021).

(171) These are issues that ICRP plans to consider in the future. However, it should also be kept in mind that patients may be a different group compared to the general population since they can have existing pathologies, the cause of which could be erroneously related to the use of radiation. For guidance on the use of effective dose for patients, see *Publication 147* (ICRP,

2021). Further advice on the meaningful interpretation of the effective dose in medicine can be found in Martin (2020) who describes the approximations made in the derivation of effective dose for medical exposures, emphasises the uncertainties in calculating the subsequent risk and warns not to overstate its accuracy. *Publication 163* (ICRP, 2025) also discusses the limitations of reference effective and organ dose coefficients for common radiographic examinations.

8. SUMMARY

(172) For over 40 years, various organisations have made efforts to estimate patient doses due to computed tomography scans. As a result, numerous tables and software tools have been developed by different authors, built upon extensive libraries of pre-calculated dose coefficients obtained using computational phantoms and Monte Carlo radiation transport codes. There is no standardised methodology to facilitate national and international assessments of such doses.

(173) ICRP has recently provided reference dose coefficients for common radiographic examinations (ICRP, 2025), and this publication extends that work to computed tomography. The availability of ICRP reference organ and effective dose coefficients in CT will facilitate the work of national and international authorities responsible for calculations of medical exposures to populations. In addition, the availability of such coefficients will aid the process of optimisation by allowing inter and intra hospital comparisons of imaging practice and procedure. Information provided as a result of the use of the coefficients will act as an aid to clinical judgement in terms of, for example, justification.

(174) This publication describes the ICRP approach to providing organ absorbed dose coefficients for CT imaging. The coefficients have been produced for the adult male and female ICRP reference voxel phantoms and the suite of paediatric phantoms. These dose coefficients are therefore not intended to be and should not be used for individual patient dosimetry and subsequent risk estimation.

(175) The scope of the publication is confined to ‘conventional’ CT; technologies such as photon counting CT or spectral CT, whether using dual detectors or kV switching have not been considered. Therefore, using these coefficients for those systems will probably lead to higher uncertainties for the resulting doses than for the ‘conventional’ CTs.

(176) Data and methods are provided to enable the computation of organ dose coefficients for any scan length, over a range of accelerating potentials and for two beam shaping filters, Head and Body. Since effective dose is a sex-averaged quantity this publication also provides values of the coefficient for either $\sum_T w_T \times H_T^M$ or $\sum_T w_T \times H_T^F$, depending on whether the simulation of the examination is performed on the male or female phantom. It must be stressed that neither quantity is ‘effective dose’, so considerable caution should be exercised, and additional uncertainties should be explicitly considered, if they are to be considered for risk estimation.

(177) A theoretical model of Automatic Tube Current Modulation has been developed to enable users to explore how a generic ATCM affects organ dose coefficients.

(178) To facilitate easy access to the data, a GUI-based calculator is provided. This calculator allows users to determine organ dose coefficients and doses without needing to perform calculations. Because the calculator does not cover all potential combinations of tube voltage, beam shaping filter, and ATCM strength, a set of analytical equations is provided to allow more comprehensive application of the dose coefficient. For example, the calculator only allows for an ATCM modulation strength of 0.75—but the data can be used to investigate ATCM with any strength between zero and one. Worked examples to assist in the calculations have been provided.

(179) Although the uncertainties in the calculated dose coefficients presented in this publication are small, there are a range of uncertainties associated with their application. These uncertainties must always be taken into account when evaluating and reporting patient doses. A solid understanding of the underlying principles and limitations is essential to avoid giving the dose estimates an unjustified level of precision.

(180) The standardised methodology described in this publication is designed to harmonise CT dose assessments internationally, eliminating inconsistencies caused by different datasets due to differing phantoms and other dosimetric methodologies. Use of the dose coefficients may support optimisation, justification, and risk communication in clinical imaging and population studies, thereby strengthening radiological protection in CT practice.

(181) The publication is intended for all those who have an interest in patient dosimetry and optimisation, such as national authorities responsible for dose calculations, medical physicists, research scientists, radiologists, radiographers, and other radiological practitioners.

REFERENCES

AAPM, 2019. Performance Evaluation of Computed Tomography Systems - The Report of TG 233. AAPM Report 233, American Association of Physicists in Medicine. Alexandriaa, VA 22314.

Agostinelli, S., Allison, J., Amako, K., et al., 2003. Geant4—a simulation toolkit. Nuclear Instruments and Methods in Physics Research Section A: Accelerators, Spectrometers, Detectors and Associated Equipment 506(3), 250-303.

Allison, J., Amako, K., Apostolakis, J., et al., 2016. Recent developments in Geant4. Nuclear Instruments and Methods in Physics Research Section A: Accelerators, Spectrometers, Detectors and Associated Equipment 835, 186-225.

Ban, N., Takahashi, F., Sato, K., et al., 2011. Development of a web-based CT dose calculator: WAZA-ARI. Radiat Prot Dosimetry 147(1-2), 333-7.

Becker, J., Zankl, M., Fill, U., et al., 2008. Katja — the 24th week of virtual pregnancy for dosimetric calculations. Pol J Med Phys Eng. 14(1), 13-19.

Berger, M.J., Hubbell, J.H., 1987. XCOM: photon cross sections on a personal computer. NBSIR 87-3597, National Bureau of Standards (former name of NIST), Gaithersburg, MD.

Berris, T., Myronakis, M., Stratakis, J., et al., 2024. Is deep learning-enabled real-time personalized CT dosimetry feasible using only patient images as input? Physica Medica 122, 103381.

Cannillo, B., Ostan, A., Dionisi, C., et al., 2018. Variability of the discrepancy between manufacturer and measured CTDI(100) values by scanner type, acquisition parameters and phantom size. Phys Med 49, 34-39.

Council of the European Union, 2014. Council directive 2013/59/Euratom of 5 December 2013 laying down basic safety standards for protection against the dangers arising from exposure to ionising radiation, and repealing Directives 89/618/Euratom, 90/641/Euratom, 96/29/Euratom, 97/43/Euratom and 2003/122/Euratom.

Cristy, M., Eckerman, K.F., 1987. Specific absorbed fractions of energy at various ages from internal photon sources, Part I: Methods. ORNL Report TM-8381/V1, Oak Ridge National Laboratory, Oak Ridge, TN.

Cullen, D.E., Hubbell, J.H., Kissel, L., 1997. EPDL97: The Evaluated Photon Data Library, '97 Version.UCRL-50400, 6, Rev. 5. UCRL-50400 Vol. 6, Rev. 5, Lawrence Livermore National Laboratory,

Damilakis, J., Stratakis, J., 2024. Descriptive overview of AI applications in x-ray imaging and radiotherapy. Journal of radiological protection : official journal of the Society for Radiological Protection 44(4),

Ding, A., Mille, M., M. , Liu, T., et al., 2012. Extension of RPI-adult male and female computational phantoms to obese patients and a Monte Carlo study of the effect on CT imaging dose. Physics in Medicine and Biology 57(9), 2441–2476.

Ding, A., Gao, Y., Liu, H., et al., 2015. VirtualDose: a software for reporting organ doses from CT for adult and pediatric patients. Physics in Medicine and Biology 60(14), 5601-5625.

EANM, 2017. Qulaity Control of Nuclear Medicine Instrumentation and Protocol Standardisation. Vienna.

Favazza, C.P., Duan, X., Zhang, Y., et al., 2015. A cross-platform survey of CT image quality and dose from routine abdomen protocols and a method to systematically standardize image quality. Physics in Medicine and Biology 60(21), 8381–8397.

Fehrmann, M.L., Schegerer, A., Werncke, T., et al., 2020. Comparison of experimental and numerical methods of patient dose estimations in CT using anthropomorphic models Radiat. Prot. Dosim. 190(1), 71-83.

Forss, V., Yli-Ollila, H., Vatanen, J., et al., 2021. The reliability of radiation dose display of a computed tomography scanner. Eur J Radiol Open 8, 100345.

GEHealthcare., DoseWatch: optimized radiation dose management. https://www.gehealthcare.com/products/dose-management/dosewatch-dose-monitoring-software-ge-healthcare.
Geyer, A.M., O'Reilly, S., Lee, C., et al., 2014. The UF/NCI family of hybrid computational phantoms representing the current US population of male and female children, adolescents, and adults--application to CT dosimetry. Phys Med Biol 59(18), 5225-42.
Gies, M., Kalender, W.A., Wolf, H., et al., 1999. Dose reduction in CT by anatomically adapted tube current modulation. I. Simulation studies. Medical Physics 26(11), 2235-2247.
Greening, J.R., 1985. Fundamentals of Radiation Dosimetry, 2nd Edition, Adam Hilger, Bristol, 1985. ISBN 0-85274-789-6 Adam Hilger, Bristol.
Hart, D., Wall, B.F., Hillier, M.C., et al., 2010. Frequency and Collective Dose for Medical and Dental X-ray Examinations in the UK, 2008. HPA-CRCE-012, Health Protection Agency, Chilton.
Hough, M., Johnson, P., Rajon, D., et al., 2011. An image-based skeletal dosimetry model for the ICRP reference adult male—internal electron sources. Physics in Medicine and Biology 56(8), 2309-2346.
Hubbell, J.H., Seltzer, S.M., 1995. Tables of X-Ray mass attenuation coefficients and 48 additional substances of dosimetric interest. NIST Report 5632, U.S. Department of Commerce, National Institute of Standards and Technology, Gaithersburg, MD.
IAEA, 2014. Diagnostic Radiology Physics. IAEA, Vienna,
IAEA, 2018. Radiation protection and safety in medical uses of ionizing radiation SSG-46. IAEA, Vienna.
Iball, G.R., Moore, A.C., Crawford, E.J., 2016. A routine quality assurance test for CT automatic exposure control systems. J Appl Clin Med Phys 17(4), 291-306.
ICRP, 1987. Radiation dose to patients from radiopharmaceuticals. ICRP Publication 53, Pergamon Press, Oxford, UK. Ann. ICRP 18(1-4)
ICRP, 1991a. 1990 Recommendations of the International Commission on Radiological Protection. ICRP Publication 60. Ann. ICRP 21(1-3),
ICRP, 1991b. Radiation dose to patients from radiopharmaceuticals. Addendum 1 to ICRP Publication 53. ICRP Publication 62. Annals of the ICRP 22(3),
ICRP, 1995. Basic anatomical and physiological data for use in radiological protection: the skeleton. ICRP Publication 70. Ann. ICRP 25(2),
ICRP, 1998. Radiation dose to patients from radiopharmaceuticals. ICRP Publication 80. Annals of the ICRP 28(3),
ICRP, 2002. Basic anatomical and physiological data for use in radiological protection: reference values. ICRP publication 89. Annals of the ICRP 32, 5.
ICRP, 2007a. Managing patient dose in multi-detector computed tomography (MDCT). ICRP Publication 102. Annals of the ICRP 37(1),
ICRP, 2007b. The 2007 Recommendations of the International Commission on Radiological Protection. Annals of the ICRP 37(2-4),
ICRP, 2009. Adult reference computational phantoms. ICRP Publication 110. Annals of the ICRP 39(2),
ICRP, 2010. Conversion Coefficients for Radiological Protection Quantities for External Radiation Exposures. ICRP Publication 116. Annals of the ICRP 40(2-5),
ICRP, 2013. Assessment of Radiation Exposure of Astronauts in Space. ICRP Publication 123, International Commission of Radiological Protection, Oxford, UK. Ann. ICRP 42(4)
ICRP, 2015a. Occupational Intakes of Radionuclides: Part 1. ICRP Publication 130. Annals of the ICRP 44(2),
ICRP, 2015b. Radiation Dose to Patients from Radiopharmaceuticals: A Compendium of Current Information Related to Frequently Used Substances. ICRP Publication 128, International Commission of Radiological Protection, Oxford, UK. Ann. ICRP 44(2S).)
ICRP, 2016a. Occupational Intakes of Radionuclides: Part 2. ICRP Publication 134 Annals of the ICRP 45(3-4), 1-352.
ICRP, 2016b. The ICRP computational framework for internal dose assessment for reference adults: specific absorbed fractions. ICRP Publication 133. Annals of the ICRP 45(2), 1-74.
ICRP, 2017. Occupational Intakes of Radionuclides: Part 3. ICRP Publication 137. Annals of the ICRP 46(3-4),

ICRP, 2019. Occupational Intakes of Radionuclides: Part 4. ICRP Publication 141. Annals of the ICRP 48(2-3), 352.
ICRP, 2020a. Adult Mesh-type Reference Computational Phantoms. ICRP Publication 145. Annals of the ICRP 49(3),
ICRP, 2020b. Paediatric Reference Computational Phantoms. ICRP Publication 143. Annals of the ICRP 49(1),
ICRP, 2020c. Dose coefficients for external exposures to environmental sources. ICRP Publication 144. Annals of the ICRP 49(2), 1-147.
ICRP, 2021. Use of Dose Quantities in Radiological Protection. ICRP Publication 147. Annals of the ICRP 50(1),
ICRP, 2022. Occupational Intakes of Radionuclides: Part 5. ICRP Publication 151. Annals of the ICRP 51(1-2),
ICRP, 2023a. Specific Absorbed Fractions for Paediatric Individuals. ICRP Publication 155. Annals of the ICRP 52(4),
ICRP, 2023b. Optimisation of Radiological Protection in Digital Radiology Techniques for Medical Imaging. ICRP Publication 154. Annals of the ICRP 52(3),
ICRP, 2024a. Paediatric mesh-type reference computational phantoms. ICRP Publication 156. Annals of the ICRP 53(1-2),
ICRP, 2024b. Dose Coefficients for Intakes of Radionuclides by Members of the Public: Part 1. ICRP Publication 158. Annals of the ICRP 53(4-5),
ICRP, 2024c. Ethics in Radiological Protection for Patients in Diagnosis and Treatment. ICRP Publication 157. Annals of the ICRP 53(3),
ICRP, 2025. Reference Organ Absorbed and Effective Dose Coefficients for Common Radiographic Examinations. ICRP Publication 163. Annals of the ICRP 54(3),
ICRU, 1964. Physical Aspects of Irradiation. National Bureau of Standards Handbook 85. 10b, International Commission on Radiation Units and Measurements,
ICRU, 1992. Photon, electron, proton and neutron interaction data for body tissues. ICRU Report 46, International Commission on Radiation Units and Measurements, Bethesda, MD.
IEC, 2016. Medical electrical equipment—Part 2-44: Particular requirements for the safety of X-ray equipment for computed tomography - Amendment 1—Corrigendum 1 Technical Report. International Electrotechnical Commission, Geneva.
ImpaCT, 2011. ImPACT patient dosimetry calculator. . https://www.ukhsa-protectionservices.org.uk/mdg/patientdosimetry/patientdoseestimationtool/.
Inoue, Y., Itoh, H., Koizumi, K., et al., 2024. Effects of organ dose modulation applied to a part of the scan range on radiation dose in computed tomography of the body. Journal of radiological protection : official journal of the Society for Radiological Protection 44(3),
Jansen, J.T.M., Shrimpton, P.C., 2016. Development of Monte Carlo simulations to provide scanner-specific organ dose coefficients for contemporary CT. Physics in Medicine and Biology 61(14), 5356–5377.
Jansen, J.T.M., Shrimpton, P.C., Edyvean, S., 2022. CT scanner-specific organ dose coefficients generated by Monte Carlo calculation for the ICRP adult male and female reference computational phantoms. Physics in Medicine & Biology 67(22), 225015.
Jansen, J.T.M., Shrimpton, P.C., Holroyd, J., et al., 2018. Selection of bone dosimetry models for application in Monte Carlo simulations to provide CT scanner-specific organ dose coefficients. Phys Med Biol 63(12), 125015.
JCGM, 2012. International Vocabulary of metrology -Basic and general concepts and associated terms (VIM) - 3rd editioin. Joint Committee for Guides in Metrology, Sévres.
Johnson, P.B., Bahadori, A.A., Eckerman, K.F., et al., 2011. Response functions for computing absorbed dose to skeletal tissues from photon irradiation - an update. Physics in Medicine and Biology 56(8), 2347–2365.
Jones, D.G., Wall, B.F., 1985. Organ doses from medical x-ray examinations calculated using Monte Carlo techniques. NRPB Report 186, National Radiological Protection Board, Chilton, Didcot, Oxon, UK.

Jones, D.G., Shrimpton, P.C., 1993. Normalised organ doses for x-ray computed tomography calculated using Monte Carlo techniques. NRPB Software Report 250, National Radiological Protection Board, Chilton, Didcot, Oxon, UK.

Kainz, W., Neufeld, E., Bolch, W.E., et al., 2019. Advances in Computational Human Phantoms and Their Applications in Biomedical Engineering - A Topical Review. IEEE Trans Radiat Plasma Med Sci 3(1), 1-23.

Kalender, W.A., Wolf, H., Suess, C., 1999a. Dose reduction in CT by anatomically adapted tube current modulation. II. Phantom measurements. Medical Physics 26(11), 2248-2253.

Kalender, W.A., Schmidt, B., Zankl, M., et al., 1999b. A PC program for estimating organ dose and effective dose values in computed tomography. European Radiology 9(3), 555-562.

Kawrakow, I., Mainegra-Hing, E., Rogers, D.W.O., et al., 2009. The EGSnrc code system: Monte Carlo simulation of electron and photon transport. PIRS Report 701, National Research Council of Canada (NRCC), Ottawa.

Khursheed, A., Hillier, M.C., Shrimpton, P.C., et al., 2002. Influence of patient age on normalized effective doses calculated for CT examinations. British Journal of Radiology 75(10), 819-830.

Kittelmann, T., et al., 2017. Monte Carlo particle lists: MCPL. Computer Physics Communications 218 17-42.

Kramer, R., Zankl, M., Williams, G., et al., 1982. The calculation of dose from external photon exposures using reference human phantoms and Monte Carlo methods, Part I: The male (Adam) and female (Eva) adult mathematical phantoms. GSF-Report S-885, GSF - National Research Center for Environment and Health, Neuherberg, Germany.

Kulesza, J.A., Adams, T.R., Armstrong, J.C., et al., 2022. MCNP Code Version 6.3.0 Theory & User Manual. United States.

Layman, R.R., Hardy, A.J., Kim, H.J., et al., 2021. A comparison of breast and lung doses from chest CT scans using organ-based tube current modulation (OBTCM) vs. Automatic tube current modulation (ATCM). J Appl Clin Med Phys 22(5), 97-109.

Le Heron, J., 1993. CTDOSE: A User's Guide. National Radiation Laboratory, Ministry of Health, Christchurch, New Zealand,

Lee, C., 2021. A Review of Organ Dose Calculation Tools for Patients Undergoing Computed Tomography Scans. J. Radiat. Prot. Res 46(4), 151-159.

Lee, C., Bolch, W.E., 2006. Age-dependent organ and effective dose coefficients for external photons: a comparison of stylized and voxel-based paediatric phantoms. Physics in Medicine & Biology 51(18), 4663.

Lee, C., Yeom, Y.S., Folio, L., 2022. CT organ dose calculator size adaptive for pediatric and adult patients. Biomed Phys Eng Express 8(6),

Lee, C., Kim, K.P., Bolch, W.E., et al., 2015. NCICT: a computational solution to estimate organ doses for pediatric and adult patients undergoing CT scans. Journal of radiological protection : official journal of the Society for Radiological Protection 35(4), 891-909.

Lee, C., Lodwick, D., Hasenauer, D., et al., 2007. Hybrid computational phantoms of the male and female newborn patient: NURBS-based whole-body models. Physics in Medicine and Biology 52(12), 3309-33.

Lee, C., Lodwick, D., Hurtado, J., et al., 2010. The UF family of reference hybrid phantoms for computational radiation dosimetry. Physics in Medicine and Biology 55(2), 339-363.

Lee, C., Flynn, M.J., Judy, P.F., et al., 2017. Body Size-Specific Organ and Effective Doses of Chest CT Screening Examinations of the National Lung Screening Trial. AJR Am J Roentgenol 208(5), 1082-1088.

Li, X., Segars, W.P., Samei, E., 2014. The impact on CT dose of the variability in tube current modulation technology: a theoretical investigation. Physics in Medicine and Biology 59(16), 4525–4548.

Lide, D.R., 2005. Handbook of Chemistry and Physics. Taylor & Francis, Boca Raton, FL. USA.

Ma, R., Qiu, R., Wu, Z., et al., 2021. Development of Chinese mesh-type pediatric reference phantom series and application in dose assessment of Chinese undergoing computed tomography scanning. Phys. Med. Biol. 66(19), 195002.

Maier, J., Klein, L., Eulig, E., et al., 2022. Real-time estimation of patient-specific dose distributions for medical CT using the deep dose estimation. Medical Physics 49(4), 2259-2269.

Martin, C.J., 2020. Effective dose in medicine. Ann. ICRP 49(1_suppl), 126-140.
Martin, C.J., Abuhaimed, A., Lee, C., 2021. Dose quantities for measurement and comparison of doses to individual patients in computed tomography (CT). Journal of radiological protection : official journal of the Society for Radiological Protection 41(4),
McMillan, K., Bostani, M., Cagnon, C.H., et al., 2017. Estimating patient dose from CT exams that use automatic exposure control: Development and validation of methods to accurately estimate tube current values. Medical Physics 44(8), 4262-4275.
Na, Y.H., Zhang, B., Zhang, J., et al., 2010. Deformable adult human phantoms for radiation protection dosimetry: anthropometric data representing size distributions of adult worker populations and software algorithms. Phys Med Biol 55(13), 3789-811.
NCRP, 2019. Medical Radiation Exposure of Patients in the United States. NCRP Report 184, National Council on Radiation Protection and Measurements, Bethesda, MD.
Nikupaavo, U., Kaasalainen, T., Reijonen, V., et al., 2015. Lens dose in routine head CT: comparison of different optimization methods with anthropomorphic phantoms. AJR. Am. J. Roentgenol. 204(1), 117-23.
Ocampo Ramos, J.C., Kofler, C., Dawson, R., et al., 2026. MIRD Pamphlet No. 34, Part 1: MIRDct-A Customizable Software Tool for CT Dosimetry. J Nucl Med,
Pafundi, D.H., 2009. Image-based skeletal tissue and electron dosimetry models for the ICRP reference pediatric age series.
Papadakis, A.E., Damilakis, J., 2020. Evaluation of an organ-based tube current modulation tool in pediatric CT examinations. European Radiology 30(10), 5728-5737.
Pelowitz, D.B.e., 2011. MCNPX User's Manual, Version 2.7.0. LA-UR-11-02295, Los Alamos National Laboratory, Los Alamos, NM.
Pelowitz, D.B.e., 2013. Initial MCNP6 Release Overview - MCNP6 version 1.0. LA-UR-13-22934, Los Alamos National Laboratory, Los Alamos, NM.
Peng, Z., Fang, X., Yan, P., et al., 2020. A method of rapid quantification of patient-specific organ doses for CT using deep-learning-based multi-organ segmentation and GPU-accelerated Monte Carlo dose computing. Medical Physics 47(6), 2526-2536.
Perkins, S.T., Cullen, D., M. Seltzer, S., 1991. Tables and graphs of electron-interaction cross sections from 10 eV to 100 GeV derived from the LLNL Evaluated Electron Data Library (EEDL), Z = 1 to 100.
Perkins, S.T., Cullen, D., M. Seltzer, S., 1997. Tables and graphs of atomic subshell and relaxation data derived from the LLNL evaluated atomic data library (EADL), Z=1-100, UCRL-50400.
Petoussi-Henss, N., Zankl, M., Schlattl, H., et al., 2006. Organdosiskonversionsfaktoren für röntgendiagnostische Untersuchungen anhand von Monte-Carlo-Simulationen. In: Bogner, L., Dobler, B. (Eds.), 37. Jahrestagung der Deutschen Gesellschaft für Medizinische Physik e.V, Regensburg, 1,
Popescu, S., Hentschel, D., Wolf, H., et al., 1999. Adaptive dose modulation during CT scanning.Assigned to Siemens Aktiengesellschaft (Munich). United States Patent & Trademark Office 5867555, 8.
Salimi, Y., Akhavanallaf, A., Mansouri, Z., et al., 2023. Real-time, acquisition parameter-free voxel-wise patient-specific Monte Carlo dose reconstruction in whole-body CT scanning using deep neural networks. Eur Radiol 33(12), 9411-9424.
Sato, K., Noguchi, H., Emoto, Y., et al., 2007. Japanese adult male voxel phantom constructed on the basis of CT images. Radiation Protection Dosimetry 123(3), 337-344.
Schlattl, H., Zankl, M., Becker, J., et al., 2010. Dose conversion coefficients for CT examinations of adults with automatic tube current modulation. Phys Med Biol 55(20), 6243-61.
Schlattl, H., Zankl, M., Becker, J., et al., 2012. Dose conversion coefficients for paediatric CT examinations with automatic tube current modulation. Physics in Medicine and Biology 57(20), 6309-6326.
Schümann, J., Paganetti, H., Shin, J., et al., 2012. Efficient voxel navigation for proton therapy dose calculation in TOPAS and Geant4. Physics in Medicine and Biology 57(11), 3281-3293.
Shrimpton, P.C., Edyvean, S., 1998. CT scanner dosimetry. Report on a round table meeting establishing a survey of standard dosimetric measurements on CT scanners, held at St George's Hospital, London, 18 April 1997. British Journal of Radiology 71, 1--3.

Shrimpton, P.C., Jones, D.G., Hillier, M.C., et al., 1991. Survey of CT practice in the UK. Part 2: Dosimetric aspects. NRPB Report 249, National Radiological Protection Board, Chilton, Didcot, Oxon, UK.

Snyder, W.S., Ford, M.R., Warner, G.G., 1978. Estimates of specific absorbed fractions for monoenergetic photon sources uniformly distributed in various organs of a heterogeneous phantom. MIRD Pamphlet 5, Revised, Society of Nuclear Medicine, New York, NY.

Snyder, W.S., Ford, M.R., Warner, G.G., et al., 1969. Estimates of absorbed fractions for monoenergetic photon sources uniformly distributed in various organs of a heterogeneous phantom. Medical Internal Radiation Dose Committee (MIRD). Pamphlet No. 5. Society of Nuclear Medicine, New York, NY.

Stamm, G., Nagel, H.D., 2002. CT-Expo - ein neuartiges Programm zur Dosisevaluierung in der CT. Fortschr Röntgenstr 174(12), 1570-1576.

Stratis, A., Molfetas, M., Panagiotakis, N., et al., 2014. Accuracy of CT dose monitor values: a multicentric study. Radiat. Prot. Dosim. 158(3), 285-289.

Sutton, D.G., Reilly, A.J., Cranley, A.J.K., et al., 2015. Catalogue of Diagnostic X-Ray Spectra and other data - Report 78 2nd Edition. The Institute of Physics and Engineering In Medicine, York.

Takahashi, F., Sato, K., Endo, A., et al., 2015. Numerical Analysis of Organ Doses Delivered During Computed Tomography Examinations Using Japanese Adult Phantoms with the WAZA-ARI Dosimetry System. Health Physics 109(2), 104-112.

Tian, X., Li, X., Segars, W.P., et al., 2015. Prospective estimation of organ dose in CT under tube current modulation. Medical Physics 42(4), 1575-1585.

Turner, A.C., Zankl, M., DeMarco, J.J., et al., 2010. The feasibility of a scanner-independent technique to estimate organ dose from MDCT scans: Using CTDIvol to account for differences between scanners. Medical Physics 37(4), 1816-1825.

Tzanis, E., Damilakis, J., 2022. A novel methodology to train and deploy a machine learning model for personalized dose assessment in head CT. European Radiology 32(9), 6418-6426.

Ukkola, L., Oikarinen, H., Henner, A., et al., 2016. Information about radiation dose and risks in connection with radiological examinations: what patients would like to know. Eur Radiol 26(2), 436-43.

UNSCEAR, 2008. Volume I: Sources, and effects of ionizing radiation. Annex A. Medical radiation exposures. United Nations Scientific Committee on the Effects of Atomic Radiation, New York.

UNSCEAR, 2020. Report to the General Assembly - Sources, Effects and Risks of Ionizing Radiation with Scientific Annexes. New York.

UNSCEAR, 2022. Sources, effects and risks of ionizing radiation. Annex A. Evaluation of medical exposure to ionizing radiation. United Nations Scientific Committee on the Effects of Atomic Radiation, New York.

van Straten, M., Deak, P., Shrimpton, P.C., et al., 2009. The effect of angular and longitudinal tube current modulations on the estimation of organ and effective doses in x-ray computed tomography. Medical Physics 36(11), 4881-4889.

White, M.C., 2012. Further Notes on MCPLIB03/04 and New MCPLIB63/84. Compton Broadening Data For All Versions of MCNP5. LANL LA-UR-12-00018, Los Alamos National Laboratory, Los Alamos.

X-5 Monte Carlo Team, 2003. MCNP–A General Monte Carlo N-Particle Transport Code, Version 5 - Vol. I: Overview and Theory," LA-UR-03-1987 Los Alamos National Laboratory, Los Alamos.

Xu, X.G., Taranenko, V., Zhang, J., et al., 2007. A boundary-representation method for designing whole-body radiation dosimetry models: pregnant females at the ends of three gestational periods—RPI-P3, -P6 and -P9. Physics in Medicine and Biology 52, 7023–7044.

Yeom, Y.S., Wang, Z.J., Thang Tat, N., et al., 2016. Development of skeletal system for mesh-type ICRP reference adult phantoms. Physics in Medicine & Biology 61(19), 7054.

Zankl, M., 2010. The GSF voxel computational phantom family, in: Xu, X.G., Eckerman, K.F. (Eds.), Handbook of anatomical models for radiation dosimetry. Taylor & Francis, Boca Raton, London, New York, pp. 65-85.

Zankl, M., Wittmann, A., 2001. The adult male voxel model "Golem" segmented from whole body CT patient data. Radiation and Environmental Biophysics 40, 153-162.

Zankl, M., Panzer, W., Drexler, G., 1991. The calculation of dose from external photon exposures using reference human phantoms and Monte Carlo methods, Part VI: Organ doses from computed tomographic examinations. GSF-Report 30/91, GSF - Forschungszentrum für Umwelt und Gesundheit, Neuherberg, Germany.

Zankl, M., Panzer, W., Drexler, G., 1992. The calculation of organ doses from computed tomography examinations. Radiation Protection Dosimetry 43(1/4), 237-239.

Zankl, M., Fill, U., Petoussi-Henss, N., et al., 2002. Organ dose conversion coefficients for external photon irradiation of male and female voxel models. Physics in Medicine and Biology 47(14), 2367-2385.

Zankl, M., Petoussi, N., Veit, R., et al., 1989. Organ doses for a child in diagnostic radiology: comparison of a realistic and a MIRD-type phantom. BIR Report 20, British Institute of Radiology, London, UK.

Zankl, M., Becker, J., Fill, U., et al., 2005. GSF male and female adult voxel models representing ICRP Reference Man - the present status. In: The Monte Carlo Method: Versatility Unbounded in a Dynamic Computing World, Chattanooga, TN, USA.,

Zhang, J., Na, Y.H., Caracappa, P.F., et al., 2009. RPI-AM and RPI-AF, a pair of mesh-based, size-adjustable adult male and female computational phantoms using ICRP-89 parameters and their calculations for organ doses from monoenergetic photon beams. Physics in Medicine and Biology 54(19), 5885–5908.

ANNEX A. COMPARING THE ICRP REFERENCE SCANNER WITH THE MODELLED SCANNERS

(A 1) Section 3 of this publication describes the development of the ICRP reference scanner. Figs 3.5 to 3.8 provide examples of how representative the ICRP reference scanner is. Fig 3.5 provides a comparison of $E_{103,\mathrm{AF}}$ estimated for the ICRP reference scanner with $E_{103,\mathrm{AF}}$ estimated for the simulated CT scanners used in its derivation. The comparison was performed at a tube voltage of 140 kV using the Body beam shaping filter for the adult female phantom (ICRP, 2009). Fig. 3.6 presents a similar comparison for $E_{103,\mathrm{AM}}$ derived using a tube voltage of 80 kV and the Head beam shaping filter. Figs 3.7 and 3.8 show corresponding examples for the absorbed dose to the colon for the adult male and female phantoms at a tube voltage of 120 kV.

(A 2) As described in the Introduction (Section 1), for simplicity in this publication, $E_{103,\mathrm{AM}}$ refers to the coefficient of the quantity $\sum_{\mathrm{T}} w_{\mathrm{T}} \times H_{\mathrm{T}}^{\mathrm{M}}$ resulting from an examination on an adult male phantom and $E_{103,\mathrm{AF}}$ refers to the coefficient of the quantity $\sum_{\mathrm{T}} w_{\mathrm{T}} \times H_{\mathrm{T}}^{\mathrm{F}}$ resulting from an examination on the adult female phantom, where $H_{\mathrm{T}}^{\mathrm{M}}$ and $H_{\mathrm{T}}^{\mathrm{F}}$ are the equivalent doses to the tissues or organs T of the reference male and female, respectively, and w_{T} is the tissue weighting factor for target tissue T, with $\sum w_{\mathrm{T}} = 1$. Per definition, the average of these coefficients gives the effective dose (ICRP, 2007b).

(A 3) This annex presents further comparisons for $E_{103,\mathrm{AF}}$ and $E_{103,\mathrm{AM}}$ for other operating conditions, as well as comparisons for the absorbed dose coefficients for these organs that are contributing to the calculation of the effective dose. As explained previously for the CT scanner models listed in Table 3.1, the manufacturers kindly provided details under Non-Disclosure Agreements. These CT scanners with their operating conditions, were used to derive the ICRP reference scanner. For these modelled CT scanners and their respective operating conditions, as well as for the derived virtual ICRP reference scanner, Monte Carlo calculations were performed for the adult male and adult female phantoms (ICRP, 2009) and absorbed organ doses were estimated for every slice along the long dimension of the phantoms. The calculation method is described in Section 3.7.

(A 4) The operating conditions of the ICRP reference scanner are combinations of tube voltages of 80, 100, 120, and 140 kV with Body and Head beam shaping filters. If a CT scanner is operated at 110 kV, a tube voltage of 120 kV is used for the figures; similarly, for 130 kV or 135 kV, a voltage of 140 kV is assumed for the figures. The Body beam shaping filter, accounts for the Body, Large, and L-Wedge filters described in Table 3.1 and the Head beam shaping filter, accounts for the Head, Small, and S-Wedge filter. The Siemens Definition dual source CT scanner has a Full and Small fan beam, and both were used in the derivation of the ICRP reference scanner.

(A 5) The calculated organ absorbed doses for both phantoms and all operating conditions for the reference CT scanner are shown as organ absorbed dose coefficients normalised to $\mathrm{CTDI}_{\text{free-in-air}}$ corrected for a slice thickness of 1 cm along the long axis of the phantom in plots to be found in the electronic supplement of this publication, in the folder called ‘CT scanner-specific dose coefficients’. The quantities $E_{103,\mathrm{AF}}$ and $E_{103,\mathrm{AM}}$ are also shown in the figures included in the Supplement. To compare the ICRP reference scanner with each of the specific modelled CT scanners, the scanner-specific coefficients are also plotted against the height along the phantom.

(A 6) In these figures, the CT scanner models listed in Table 3.1 are randomised and referred to as CT scanner A to M, for 80, 120, and 140 kV and as CT scanner A to K, for 100 kV, and the respective curves are represented by different coloured lines (see plot legends).

The relevant dose coefficients for the ICRP reference scanner are shown as black lines. The average dose coefficients of the modelled CT scanners at these operating conditions at every slice are shown as grey dashed lines indicated as '<xx Body>' or '<xx Head>', where 'xx' is the value of tube voltage in kV. If in any graph the solid black line is almost identical or very close to the grey dashed line, the agreement between the average coefficient and the coefficient of the ICRP reference scanner is excellent. The coloured lines showing the coefficients of the modelled CT scanners demonstrate the level of uncertainty per slice for the average values of coefficients obtained from all modelled CT scanners and can be used to judge if the ICRP reference scanner is representative for all the modelled CT scanners. Note that the beginning of the trunk is positioned at 0 cm in all of the figures.

(A 7) From the figures, it can be concluded that the ICRP reference scanner is representative for all the CT scanners considered for the respective operating conditions. The analysis shows that the dose coefficients of the ICRP reference scanner are well within one standard deviation of the averaged dose coefficients of the CT scanner models but some difference between these curves can be observed for the abdominal and chest region i.e. at distances from about 10 cm to 50 cm along the phantom.

ANNEX B. VERIFICATION OF THE MONTE CARLO CALCULATIONS OF DOSE COEFFICIENTS (SPOT CHECKS)

(B 1) The calculated reference organ and effective dose coefficients for the ICRP paediatric and adult voxel phantoms were independently verified by repeating some of the calculations. The adult dose coefficients calculated by MCNP6.1 (Pelowitz, 2013) were benchmarked by two other methods based on MCNPX2.7 (Pelowitz, 2011) and Geant4 (Version 10.7) (Agostinelli et al., 2003), respectively for some specific operating conditions. The paediatric data calculated by MCNPX2.7 were verified by MCNP6.1 and Geant4-based methods, again for some specific operating conditions. Verification was conducted in two different phases: (i) using ICRP reference scanner without tube current modulation; and (ii) using the ICRP reference scanner with tube current modulation implemented, as described in Section 4.

B.2. Monte Carlo simulation method based on Geant4

(B 2) The Monte Carlo code, Geant4 (Version 10.7) (Agostinelli et al., 2003), was used as an independent calculation method of dose coefficients to verify the primary dataset of the organ and effective dose coefficients produced using MCNPX2.7 and MCNP 6.1. The Geant4 Monte Carlo code was developed in the C++ programming language and has been actively improved and maintained by the Geant4 collaboration of various international research groups. The Geant4 code is freely released via the website (http://geant4.cern.ch/) and widely used in various applications including radiation dosimetry, medical application, space science, and accelerator physics (Allison et al., 2016).

(B 3) To simulate the representative scanner in the Geant4 code, one approach that might be considered would be to interpret and identically define the geometry and source of the scanner used in the MCNP input file in the Geant4 code. Instead, the information (position, direction, and energy) of the particles (photons and secondary electrons) crossing the boundary of the scanner bore was pre-generated by performing simulations with the MCNP6.1 input file where the geometry and source of the representative scanner, which was then used to simulate the source in the Geant4 code. This approach does not require the geometry modelling of the representative scanner and is more efficient in dose calculations against the full simulation of x-ray source together with the scanner geometry.

(B 4) To generate the phase-space files, the original MCNP6.1 input file for the representative scanner was slightly modified to include the SSW (Surface Source Write) card and used to perform Monte Carlo simulations using MCNP6.2 (Werner et al., 2018), finally creating an SSW file including the information of the particles crossing the boundary of the scanner bore. The binary SSW file was converted to an ASCII file by using the MCPL (Monte Carlo Particle Lists) code (Kittelmann, 2017). The converted ASCII file, which is a human readable text file, was implemented in the Geant4 code. For each MCNP simulation used to generate the phase-space file for a particular condition such as filter type (Body or Head) and slice thickness (depending on phantom type), 10^7 primary particles were simulated and then about 5×10^4 to 5×10^5 particles were recorded in the phase-space file depending on the conditions. During the dose calculations in the Geant4 code from the source data in the phase-space file, a particle was selected randomly, and its position and direction were rotated uniformly around the z-axis (i.e., the central axis of the scanner bore) to simulate the axial rotation of the CT scanner.

(B 5) The voxel models of the reference phantoms were implemented in the Geant4 code using the G4VNestedParameterisation class, recommended by a study (Schümann et al., 2012) as the most efficient class among the various classes handling voxel geometry. To transport photons and secondary electrons, the physics library of the G4EmLivermorePhysics was used, including EPDL97 (Cullen et al., 1997), EEDL (Perkins et al., 1991), and EADL (Perkins et al., 1997). The default secondary production cut-off range of 1 mm was reduced to 1 μm for secondary electrons to secure precision of simulation. Absorbed doses to all target organs/tissues, except for the target skeletal tissues (i.e., red bone marrow and endosteum), were calculated by using the G4PSEnergyDeposit class. The absorbed doses to the skeletal tissues were calculated using the paediatric DRFs provided in *Publication 155* (ICRP, 2023) following the same approach used in a previous study (Yeom et al., 2016). 10^7 primary particles for each slice simulation were used so that the coefficients of variance of the calculated organ/tissue absorbed doses were below 5% for most organs/tissues crossing each fan beam. Details of the Geant4 simulations are given in Table B.1. It should be noted that, whilst the primary paediatric and adult dose coefficient calculations were performed with phantoms placed in air and the spot check calculations used phantoms in vacuum, this methodological difference has no practical consequence for the results. It merely reflects the different procedures followed by different calculators. Since the CT scanner spectra are hardened by the homogenous and beam shaping filters, the inclusion or exclusion of air attenuation and scatter has no relevance, especially given the short distance between the filter of the x-ray tube and the skin entrance.

Table B.1. Details of the methodology used for the Monte Carlo calculations of the dose coefficients using Geant4.

Purpose	Verification of organ absorbed dose coefficients
Radiation transport code	Geant4
Cross section library	EPDL97 (Cullen et al., 1997), EEDL (Perkins et al., 1991), EADL (Perkins et al., 1997)
Particles considered	Photons and secondary electrons
Energies Considered	80, 100, 120, 140 kV
Source	Phase-space created from MCNP6.1 (Pelowitz, 2013) input files
Anthropomorphic phantoms	ICRP reference adult (ICRP, 2009) and paediatric (ICRP,2020) voxel phantoms
Surrounding medium	Vacuum
Position of arms of phantoms	Arms removed. See Section 2
Projections (examinations) simulated	Fan beam irradiating a slice from the top of the head to bottom of the feet with the slice thickness (Table 3.7)
Skeletal dosimetry	Use of Dose Response Functions, DRF (ICRP, 2023)
Organ dose coefficients	Red bone marrow (R-marrow), colon, lung, stomach wall (ST-wall), breast, ovaries or testes (gonads), urinary bladder wall (UB-wall), oesophagus, liver, thyroid, skeletal endosteum (Endost-BS), brain, salivary glands (S-glands), skin, remainder tissues: adrenals, extrathoracic region (ET), gall bladder wall (GB-wall,) heart wall (Ht-wall), kidneys, lymph, muscle, oral mucosa (O-mucosa), pancreas, small intestine wall (SI-wall), spleen, thymus, uterus (female) or prostate (male), and lens of the eye (lens)
Effective dose coefficients	The contribution of the male and female reference individuals is given separately
Normalisation quantity	$CTDI_{free\text{-}in\text{-}air}$ (Gy photon^{-1})

B.3. Verification of the calculations of organ dose coefficients for the ICRP reference scanner without tube current modulation

(B 6) Organ-level doses per $CTDI_{free\text{-}in\text{-}air}$ (Gy Gy^{-1}) for the ICRP adult male voxel phantom calculated by MCNP6.1 method (primary calculation) were compared with those calculated from the accelerated MCNPX2.7 method (verifier) for the ICRP reference scanner without tube current modulation implemented. Agreement well within 6% was achieved across the organs and skeletal tissues as shown in Fig. B.1a.

(B 7) Next, the organ dose coefficients calculated for the ICRP 10-year-old male voxel phantom using the MCNPX2.7 method (primary calculation) were compared with those from the MCNP6.1 and Geant4 methods (verifiers). For more thorough comparison, the summation of 577 slices from the bottom of the feet to the top of the head was calculated for each organ and effective dose and compared to each other. The results agreed within 10% as depicted in Fig. B.1b.

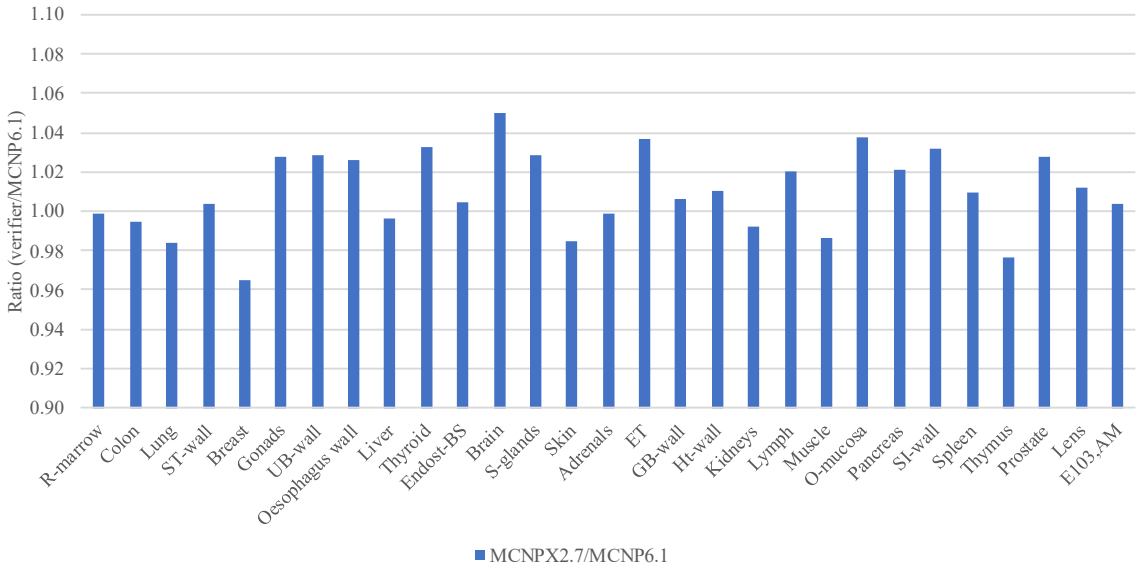

Fig. B.1a. Comparison of organ dose per $CTDI_{free\text{-}in\text{-}air}$ (Gy Gy^{-1}) for (a) the ICRP adult male voxel phantom using MCNPX2.7 (Pelowitz, 2011) (verifier) and MCNP6.1 (Pelowitz, 2013) (primary calculation). Both simulations were performed at 120 kV with the Body beam shaping filter of the ICRP reference scanner model.

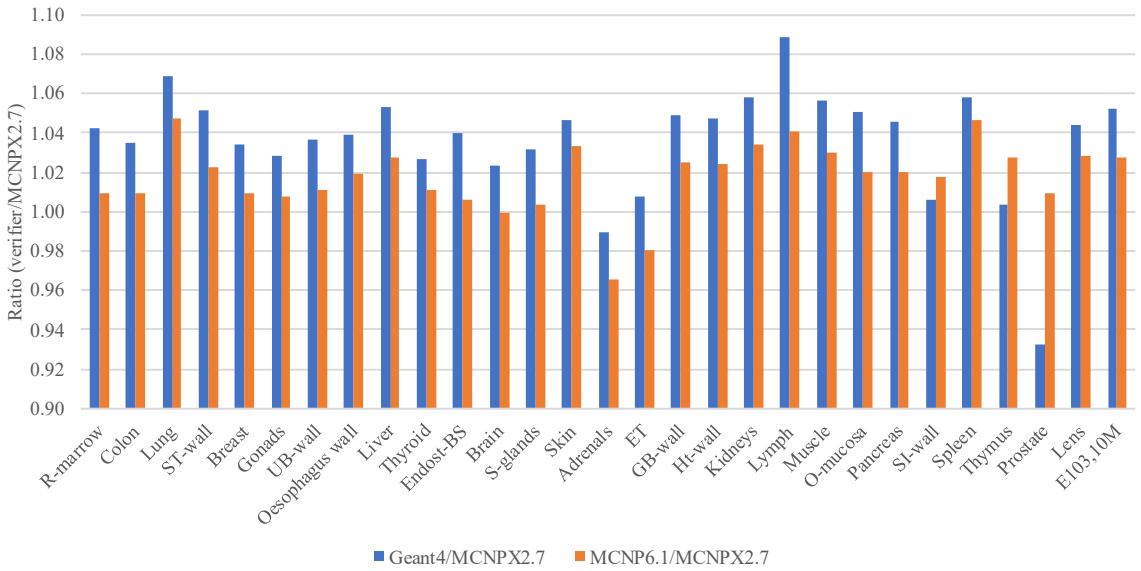

Fig. B.1b. Comparison of organ dose per $CTDI_{free\text{-}in\text{-}air}$ (Gy Gy^{-1}) for the ICRP 10-year-old male voxel phantom using MCNP6.1 (Pelowitz, 2013) and Geant4 (Agostinelli et al, 2003) (verifiers) with MCNPX2.7 (Pelowitz, 2011) (primary calculation). All simulations were performed at 120 kV with the Body beam shaping filter of the ICRP reference scanner model.

B.4. Verification of the calculations of the organ dose coefficients for the ICRP reference scanner with tube current modulation

(B 8) Finally, organ doses per $CTDI_{free\text{-}in\text{-}air}$ (Gy Gy^{-1}) calculated for the ICRP reference scanner with longitudinal tube current modulation, as described in Section 4, were calculated by the primary calculation methods (MCNP6.1 for the adult phantoms and MCNPX2.7 for the paediatric phantoms) and compared with those from the verifier methods. The summation of dose per slice across the total slices was calculated and compared for the ICRP (a) adult, (b) 10-year-old, (c) 5-year-old, and (d) newborn voxel phantoms (Fig. B.2). The discrepancy was less than 5% for all cases.

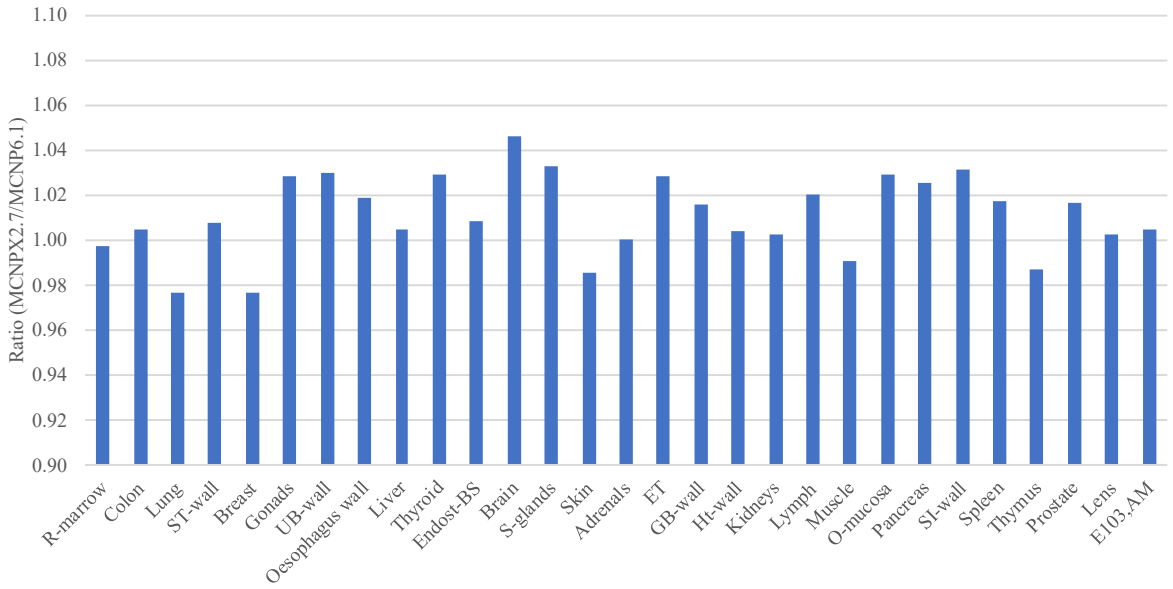

Fig. B.2a. Comparison of organ dose per $CTDI_{free\text{-}in\text{-}air}$ (Gy Gy^{-1}) for the ICRP adult male voxel phantom using MCNPX2.7 (Pelowitz, 2011) (verifier) and MCNP6.1 (Pelowitz, 2013). Both simulations were performed at 120 kV with the Body beam shaping filter of the ICRP reference scanner model.

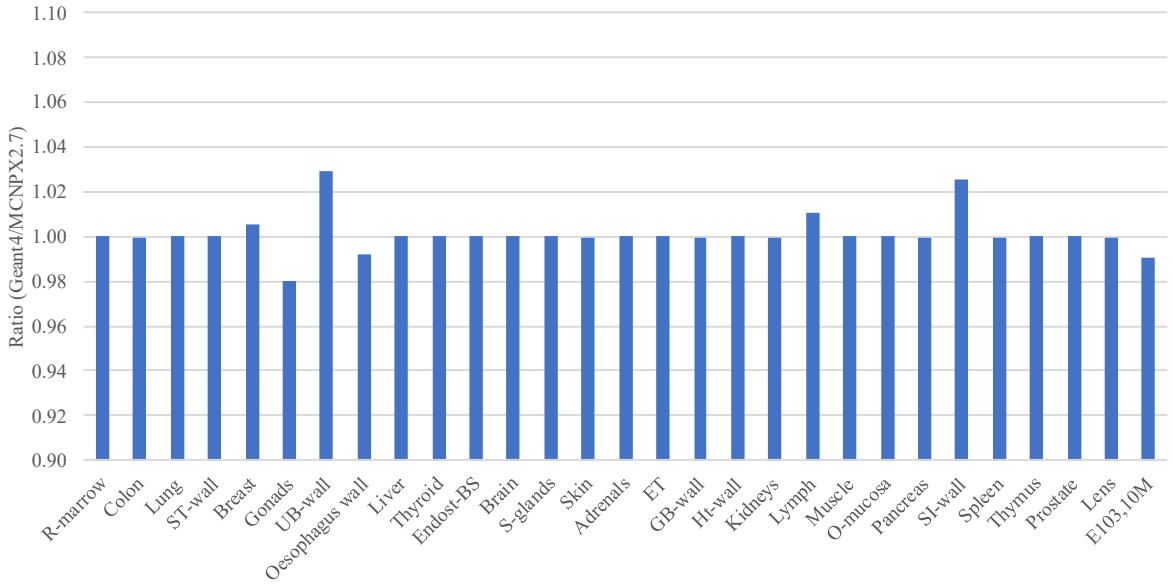

Fig. B.2b. Comparison of organ dose per $CTDI_{free\text{-}in\text{-}air}$ (Gy Gy^{-1}) for the ICRP 10-year-old male voxel phantom using Geant4 (Agostinelli et al, 2003) (verifier) and MCNPX2.7 (Pelowitz, 2011). Both simulations were performed at 120 kV with the Body beam shaping filter of the ICRP reference scanner model.

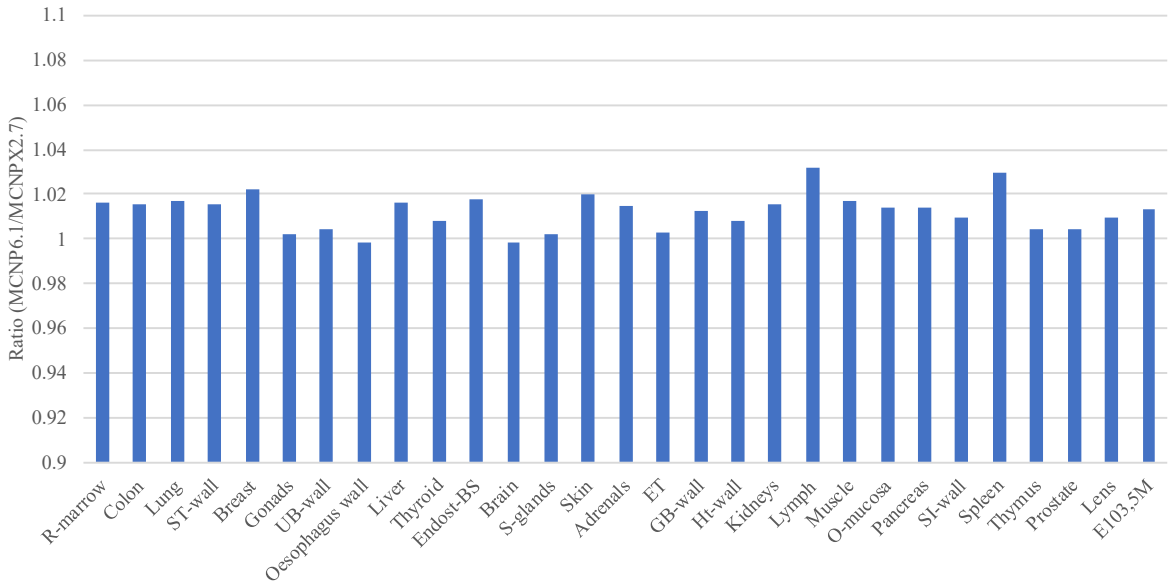

Fig. B.2c. Comparison of organ dose per $CTDI_{free\text{-}in\text{-}air}$ (Gy Gy^{-1}) for the ICRP 5-year-old male voxel phantom using MCNP6.1 (Pelowitz, 2013) (verifier) and MCNPX2.7 (Pelowitz, 2011). Both simulations were performed at 120 kV with the Body beam shaping filter of the ICRP reference scanner model.

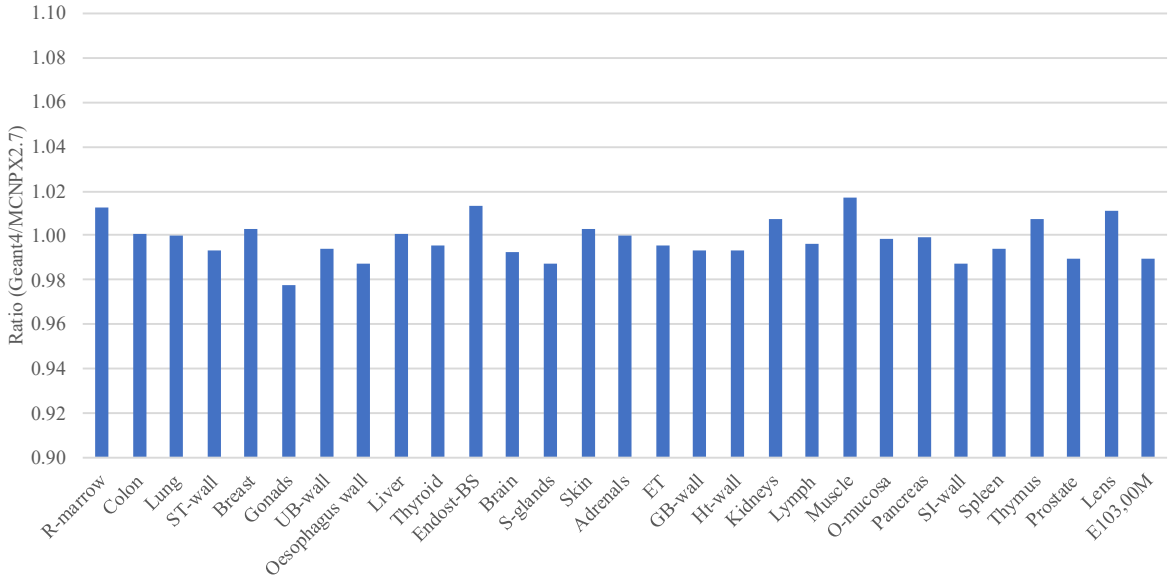

Fig. B.2d. Comparison of organ dose per $CTDI_{free\text{-}in\text{-}air}$ (Gy Gy^{-1}) for the ICRP newborn male voxel phantom using Geant4 (Agostinelli et al, 2003) (verifier) and MCNPX2.7 (Pelowitz, 2011). Both simulations were performed at 120 kV with the Body beam shaping filter of the ICRP reference scanner model.

B.5. References

Agostinelli, S., Allison, J., Amako, K., et al., 2003. Geant4—a simulation toolkit. Nuclear Instruments and Methods in Physics Research Section A: Accelerators, Spectrometers, Detectors and Associated Equipment 506(3), 250-303.

2371 Allison, J., Amako, K., Apostolakis, J., et al., 2016. Recent developments in Geant4. Nuclear
2372 Instruments and Methods in Physics Research Section A: Accelerators, Spectrometers, Detectors
2373 and Associated Equipment 835, 186-225.
2374 Cullen, D.E., Hubbell, J.H., Kissel, L., 1997. EPDL97: The Evaluated Photon Data Library, '97
2375 Version.UCRL-50400, 6, Rev. 5. UCRL-50400 Vol. 6, Rev. 5, Lawrence Livermore National
2376 Laboratory.
2377 ICRP, 2009. Adult reference computational phantoms. ICRP Publication 110. Annals of the ICRP 39(2).
2378 ICRP, 2020. Paediatric Reference Computational Phantoms. ICRP Publication 143. Annals of the ICRP
2379 49(1).
2380 ICRP, 2023. Specific Absorbed Fractions for Paediatric Individuals. ICRP Publication 155. Annals of
2381 the ICRP 52(4).
2382 Kittelmann, T., et al., 2017. Monte Carlo particle lists: MCPL. Computer Physics Communications 218
2383 17-42.
2384 Pelowitz, D.B.e., 2011. MCNPX User's Manual, Version 2.7.0. LA-UR-11-02295, Los Alamos
2385 National Laboratory, Los Alamos, NM.
2386 Pelowitz, D.B.e., 2013. Initial MCNP6 Release Overview - MCNP6 version 1.0. LA-UR-13-22934,
2387 Los Alamos National Laboratory, Los Alamos, NM.
2388 Perkins, S.T., Cullen, D., M. Seltzer, S., 1991. Tables and graphs of electron-interaction cross sections
2389 from 10 eV to 100 GeV derived from the LLNL Evaluated Electron Data Library (EEDL), Z = 1 to
2390 100.
2391 Perkins, S.T., Cullen, D., M. Seltzer, S., 1997. Tables and graphs of atomic subshell and relaxation data
2392 derived from the LLNL evaluated atomic data library (EADL), Z=1-100, UCRL-50400.
2393 Schümann, J., Paganetti, H., Shin, J., et al., 2012. Efficient voxel navigation for proton therapy dose
2394 calculation in TOPAS and Geant4. Physics in Medicine and Biology 57(11), 3281-3293.
2395 Werner, Christopher John, Bull, Jeffrey S., Solomon, C. J., et al., 2018 MCNP Version 6.2 Release
2396 Notes, https://doi.org/10.2172/1419730.
2397 Yeom, Y.S., Wang, Z.J., Thang Tat, N., et al., 2016. Development of skeletal system for mesh-type
2398 ICRP reference adult phantoms. Physics in Medicine & Biology 61(19), 7054.

ANNEX C. DOSIMETRIC QUANTITIES USED IN PATIENT DOSIMETRY IN COMPUTED TOMOGRAPHY

C.1. Organ absorbed dose and equivalent dose

(C 1) The mean absorbed dose averaged over the volume of organs and tissues is the primary scientific quantity from which effective dose, E, is calculated. Absorbed dose (D) is defined as the quotient of mean energy imparted, $\mathrm{d}\bar{\varepsilon}$ by ionising radiation in a volume element and the mass, $\mathrm{d}m$, of the matter in that volume:

$$D = \frac{\mathrm{d}\bar{\varepsilon}}{\mathrm{d}m} \tag{C.1}$$

(C 2) The International System (SI) unit of absorbed dose is J kg^{-1}, and its special name is gray (Gy). Absorbed dose is derived from the mean value of the stochastic quantity of energy imparted, ε, and does not reflect the random fluctuations of the interaction events in tissue. While it is defined at any point in matter, its value is obtained as an average over a mass element $\mathrm{d}m$ and hence over many atoms or molecules of matter.

(C 3) When using the quantity absorbed dose in radiological protection, doses are averaged over tissue volumes. It is assumed that for low doses, the mean value of absorbed dose averaged over a specific organ or tissue can be correlated with radiation detriment for stochastic effects in that tissue with an accuracy sufficient for the purposes of radiological protection. The averaging of absorbed dose is carried out over the volume of a specified organ (e.g. liver) or tissue (e.g. active bone marrow) or the sensitive region of a tissue (e.g. endosteal surfaces of the skeleton).

(C 4) Equivalent dose, H_T, to a tissue or organ is defined as:

$$H_{T=} \sum_R w_R D_{T,R} \tag{C.2}$$

where w_R is the radiation weighting factor for radiation type R and $D_{T,R}$ is the mean absorbed dose from the incident radiation type R on the body for a tissue or organ T of the age-specified Reference Male or Female. Since w_R is dimensionless, the SI unit for the equivalent dose is the same as for absorbed dose, J kg^{-1}, and its special name is sievert (Sv). Values of w_R are shown in Table C.1 and are taken from *Publication 103* (ICRP, 2007).

Table C.1. ICRP radiation weighting factors (ICRP, 2007).

Radiation type	Radiation weighting factor, w_R
Photons	1
Electrons and muons	1
Protons and charged pions	2
Alpha particles, fission fragments, heavy ions	20
Neutrons	Continuous function of neutron energy See Eq. (4.3) of *Publication 103* (ICRP, 2007).

C.2. Effective dose

(C 5) The effective dose, E, introduced in *Publication 60* (ICRP, 1991) is the risk-related quantity in radiological protection and is defined as a weighted sum of organ equivalent doses. In accordance with the definition of effective dose in *Publication 103* (ICRP, 2007), the effective dose is computed as:

$$E = \sum_T w_T \left[\frac{H_T^F + H_T^M}{2}\right], \quad \text{(C.3)}$$

where H_T^M and H_T^F are the equivalent doses to the tissues or organs T of the Reference Male and Female, respectively, and w_T is the tissue weighting factor for target tissue T, with $\Sigma w_T = 1$. The sum is performed over all organs and tissues of the human body considered to be sensitive to the induction of stochastic effects. Values of w_T are given in *Publication* 103 (ICRP, 2007). Since w_R and w_T are dimensionless, the SI unit for effective dose is the same as for absorbed and equivalent dose, J kg^{-1}, and its special name is sievert (Sv).

(C 6) Eq. C.3 is numerically the same as:

$$E = \frac{E_M + E_F}{2}, \quad \text{(C.4)}$$

where $E_M = \sum_T w_T \times H_T^M$ and $E_F = \sum_T w_T \times H_T^F$, respectively. In this document, these contributions are annotated as $E_{103,AM}$ and $E_{103,AF}$, for the adult male and female phantoms, $E_{103,15M}$, $E_{103,15F}$ for the 15-year-old male and female, $E_{103,10M}$, $E_{103,10F}$ for the 10-year-old etc. and are given at the tables of the electronic supplement. The effective dose can be obtained by taking the average of the two.

(C 7) Effective dose (E) was originally introduced for the control of occupational exposures to external and internal sources of radiation. While the concept has remained essentially unchanged through *Publication 60* (ICRP, 1991) to *Publication 103* (ICRP, 2007), its use has been extended to members of the public of all ages, including in utero exposures of the fotus (ICRP, 2001, 2004, 2006). ICRP provides effective dose coefficients for situations of external and internal exposures of workers and members of the public, and for radiopharmaceutical administrations to patients, as reference values for use in prospective and retrospective dose assessments.

Table C.2. ICRP tissue weighting factors (ICRP, 2007).

Tissue	w_T	$\sum w_T$
Bone-marrow, breast, colon, lung, stomach, remainder tissues (13*)	0.12	0.72
Gonads	0.08	0.08
Urinary bladder, oesophagus, liver, thyroid	0.04	0.16
Bone surface, brain, salivary glands, skin	0.01	0.04

w_T, tissue weighting factor.

*Remainder tissues: adrenals, extrathoracic (ET) regions of the respiratory tract, gall bladder, heart, kidneys, lymphatic nodes, muscle, oral mucosa, pancreas, prostate (male), small intestine, spleen, thymus, uterus/cervix (female).

(C 8) The tissue weighting factors of Table C.2 are sex- and age-averaged values for all organs and tissues, including the male and female breast, testes, and ovaries (i.e. gonads: related to possible carcinogenic and heritable effects). This averaging implies that the application of this approach is restricted to the determination of effective dose in radiological protection (ICRP, 2007).

(C 9) E is calculated for sex-averaged Reference Persons at specified ages as defined in *Publication 89*. *Publication 103* definition includes the specification of reference male and female anatomical phantoms for radiation transport calculations. While exposures may relate to individuals or population groups, E is calculated for Reference Persons exposed in the same way.

(C 10) Effective dose (E), in units of sievert (Sv), is accepted internationally as the central radiological protection quantity and is used for regulatory purposes worldwide, providing a risk-adjusted measure of total body dose from both external and internal sources in relation to stochastic risks of cancer and hereditary effects, expressed in terms of detriment. Considering

the uncertainties associated with risk projection to low doses or low dose rates, effective dose may be considered as an approximate indicator of possible risk, recognising also that lifetime cancer risk varies with age at exposure, sex, and population group. *E* has proved to be a valuable and robust quantity for use in the optimisation of protection and in setting of control criteria such as dose limits, constraints, and reference levels for workers, research subjects, or members of the public.

(C 11) *Publication 147* (ICRP, 2021) provides additional guidance for the use of effective dose to estimate risks, particularly in evaluating exposures of patients from medical procedures. In medical applications, estimates of effective dose can be used for comparing doses from different diagnostic and interventional imaging modalities (e.g. computed tomography and nuclear medicine) and exposure techniques that give different spatial distributions of radiation within the body tissues. In this context, effective dose is used to provide a generic indicator for classifying different types of medical procedure into broad risk categories for the purpose of communicating risks to clinicians and patients. Effective dose is also used to inform decisions on justification of patient diagnostic and interventional procedures, planning requirements in research studies, and evaluation of unintended exposures. In each of these cases, effective dose provides an approximate indicator of possible risk. Thus, effective dose can be used prospectively as an indicator of radiation detriment in justification decisions and when planning medical research studies involving radiation exposure, or retrospectively in assessments of accidental exposures.

(C 12) Moreover, *Publication 147* (ICRP, 2021) lists the situations for medical procedures for which effective dose is not recommended to be used: measurable quantities are used directly in applications comparing doses from particular procedures in different health centres, including the setting of diagnostic reference levels and in maintenance of patient records. For situations in which a single organ receives the majority of the dose, such as the breast in mammography or the thyroid from therapeutic administration of radioiodine, mean absorbed doses to the tissues of interest should be used rather than effective dose.

(C 13) For communication of doses and associated health risks, the reader is referred to *Publication 147* (ICRP, 2021).

C.3. Air kerma and CT dosimetry quantities used in this publication

(C 14) The kerma, K, for ionising uncharged particles, is given by

$$K = \frac{\mathrm{d}E_{\mathrm{tr}}}{\mathrm{d}m}, \tag{C.5}$$

where $\mathrm{d}E_{\mathrm{tr}}$ is the mean sum of the initial kinetic energies of all the charged particles liberated in the mass ($\mathrm{d}m$) of a material by the uncharged particles incident on $\mathrm{d}m$. The unit of kerma is J kg^{-1}, and has the special name gray (Gy). The quantity ($\mathrm{d}E_{\mathrm{tr}}$) includes the kinetic energy of the charged particles emitted in the decay of excited atoms/molecules or in nuclear de-excitation or disintegration.

(C 15) The Computed Tomography Dose Index (CTDI) is most commonly defined for a 100 mm long pencil ionisation chamber by

$$\mathrm{CTDI} = \frac{1}{NT}\int_{-50\mathrm{mm}}^{50\mathrm{mm}} K(z)\mathrm{d}z. \tag{C.6}$$

In this equation N is the number of detector rows and T is the nominal thickness of each row (Martin and Sutton, 2014). CTDI has the unit Gy. The pencil chamber (and thus the integration) must be parallel to the rotation axis of the CT scanner and the air kerma $K(z)$ is measured for a single rotation (ICRU, 2005).

(C 16) The methodology for determining CTDI is employed for measurements carried out both free-in-air and in the standard PMMA dosimetry Head and Body phantoms (ICRU,1992).

(C 17) Measurements of CTDI performed in the standard phantoms are carried out in air and at the centre ($CTDI_{centre}$) and periphery ($CTDI_{periphery}$) of the phantoms. The $CTDI_{periphery}$ is measured at four evenly distributed locations positioned 10 mm below the surface and is the average of these four measurements. The weighted $CTDI_w$ is then defined by

$$\mathrm{CTDI_w} = \frac{1}{3}\left(\mathrm{CTDI_{centre}} + 2\mathrm{CTDI_{periphery}}\right) \quad \text{(C.7)}$$

and has the unit Gy.

(C 18) Another quantity used in CT dosimetry is $CTDI_{vol}$, a volume average that is defined as

$$\mathrm{CTDI_{vol}} = \frac{\mathrm{CTDI_w}}{p}, \quad \text{(C.8)}$$

where p is the pitch defined as the distance the patient table travels during one revolution, divided by the slice thickness or beam collimation.

(C 19) A CT scan involves irradiation along the z axis length of a scanner, thus a volume type dose descriptor is used, which is the CT Dose Length Product (DLP). This is specifically the product of $CDTI_{vol}$ (Gy) and scan length L (cm)

$$\mathrm{DLP} = \mathrm{CTDI_{vol}}L. \quad \text{(C.9)}$$

The DLP represents the total radiation exposure over the scanned length of the body and has the unit of Gy cm.

C.4. References

ICRP, 1991. 1990 Recommendations of the International Commission on Radiological Protection. ICRP Publication 60. Ann. ICRP 21(1–3).

ICRP, 2001. Doses to the embryo and fetus from intakes of radionuclides by the mother. ICRP Publication 88. Ann. ICRP 31(1–3).

ICRP, 2004. Doses to infants from radionuclides ingested in mothers' milk. ICRP Publication 95. Ann. ICRP 34(3–4).

ICRP, 2006. Assessing Dose of the Representative Person for the Purpose of the Radiation Protection of the Public. ICRP Publication 101a. Ann. ICRP 36(3).

ICRP, 2007. The 2007 Recommendations of the International Commission on Radiological Protection. ICRP Publication 103. Ann. ICRP 37(2–4).

ICRP, 2021. Use of Dose Quantities in Radiological Protection. ICRP Publication 147. Ann. ICRP 50(1).

ICRU, 1992 Phantoms and Computational Models in Therapy, Diagnosis ad Protection ICRU Report 48. International Commission on Radiation Units and Measurement, Bethesda, MD.

Martin, C., Sutton, D.G., 2014. Practical Radiation Protection in Healthcare, 2nd Edition. Oxford University Press, Oxford.

ANNEX D. DESCRIPTION OF THE ELECTRONIC SUPPLEMENT

(D 1) The electronic supplement available for download from the current publication consists of three sets of data files, each set to be found in a different folder – and a set of graphical illustrations.

D.1. Data files

D.1.1. Tables of dose coefficients per $CTDI_{free\text{-}in\text{-}air}$

(D 2) For each phantom, two sets of tables are provided as Excel and open-source spreadsheets. There are twelve tables in each set, corresponding to the twelve phantoms utilised. Each table in the first set has the suffix '_notcm' indicating that no tube current modulation has been applied. For example, the table '_adm_dose_notcm' refers to data for the adult male phantom when a constant tube current has been applied i.e. no ATCM. These tables can be found in the folder CONSTANT. Each table in the second set, found in the folder COSINE, has the suffix '_tcm' indicating that the coefficients have been generated using an incident fluence that is proportional to $(1 + \cos 2\varphi)$ as described in Section 4.

(D 3) Each table contains six (for the paediatric) or eight (for the adult) tabs corresponding to the different spectra employed, i.e. 80 kV Head, 80 kV Body, 100 kV Head, 100 kV Body, 120 kV Head, 120 kV Body, 140 kV Head, and 140 kV Body. Each tab is structured as follows:

- Column A: Slice number
- Column B: z location from the top of the head (cm)
- Column C–AD: slice-specific organ dose coefficients
- Column AE: slice-specific effective dose coefficients

(D 4) The number of rows in each data file is equal to the number of axial slices used in the simulation, as shown in Table 3.7. So, for example, there are 222 rows of data in the file for the adult male and 576 in the file for the 10-year-old female. Each row of data provides coefficients of organ absorbed dose per $CTDI_{air}$ in mGy mGy^{-1} for each of the 28 organs and tissues, as well as for $E_{103,\#\#M}$ or $E_{103,\#\#F}$ in mSv mGy^{-1}.

D.1.2. Tables of $CTDI_{free\text{-}in\text{-}air}$ to $CTDI_w$ conversion factors

(D 5) The folder '$CTDI_w$' contains one Excel / open-source spreadsheet that includes the $CTDI_w$ per $CTDI_{free\text{-}in\text{-}air}$ conversion factors (in Gy Gy^{-1}) for 80, 100, 120, and 140 kV Head and Body filters, measured in both the $CTDI_w$ Body and $CTDI_w$ Head phantoms. Thus, there are a total of 16 conversion factors. This allows for a greater range of conditions to be computed than is possible using the GUI-based calculator.

D.1.3. Tables of attenuation factors A^{AP} and A^{RLAT}

(D 6) Four sets of tables are provided as Excel and open-source spreadsheets in the folder 'Attenuation Data'. There is a table for each of 80, 100, 120, and 140 kV. Each table contains entries for the newborn, 1-year-old, 5-year-old, 10-year-old, 15-year-old male, 15-year-old female, adult male, and adult female phantoms. For each slice of each phantom, values are provided for A^{AP} and A^{RLAT}, and also for ζ_i, τ_i, and η_i (all as described in Section 4). The latter three variables, i.e. ζ_i, τ_i, and η_i, can be varied by entering a value for modulation strength q in

the first sheet of each set of Tables. Note, that for the reference Head and Body filters the same attenuation factors are used.

D.2. Set of figures

(D 7) The folder indicated as 'CT scanner-specific dose coefficients' shows graphically the organ absorbed dose coefficients normalised to the $CTDI_{free\text{-}in\text{-}air}$ (in Gy Gy^{-1}) with a slice thickness of 1 cm along the long axes of the phantom, for the reference adult male and female phantoms and for the reference CT scanner and all operating conditions. The organs considered are those contributing to the effective dose (ICRP, 2007) and the lens of the eye. The quantities $E_{103,AM}$ and $E_{103,AF}$ are also shown in separate figures. To compare the ICRP reference scanner with each of the specific modelled CT scanners, the scanner-specific coefficients (see Table 3.1 for scanners and operating conditions) are also plotted against the height along the phantom.

D.3. References

ICRP, 2007. The 2007 Recommendations of the International Commission on Radiological Protection. ICRP Publication 103. Ann. ICRP 37(2–4).

ACKNOWLEDGEMENTS

This is the second publication from ICRP Task Group 113 on Reference Organ and Effective Dose Coefficients for Common Diagnostic X-Ray Imaging Examinations. Task Group 113 is a joint Task Group of ICRP Committees 2 and 3 and was established in May 2019. The first publication was concerned with exposures in diagnostic radiography (*Publication* 163), this publication of the Task Group covers computed tomography. Forthcoming publications will address paediatric diagnostic fluoroscopy, fluoroscopically guided interventions, and radiographic and CT exposures of the pregnant patient and its fetus. This is the first time that ICRP has published reference dose coefficients for these types of exposures.

ICRP thanks all those involved in the development of this publication for their hard work and dedication. Special thanks are due to Kimberly Applegate, Francois Bochud, Wesley Bolch, and John Harrison.

Task Group 113 members

N. Petoussi-Henss (Co-Chair)	K. Jones	D. Satoh
D. Sutton (Co-Chair)	C.H. Kim	H. Schlattl
K. Applegate	P. Kunert	I. Sechopoulos
W.E. Bolch	J. Li	W. Smither
D. Borrego	C. Lee	K. Wunderle
J.W. Choi	Y. Lee	Y.S. Yeom
K. Griffith	S. Mann	M. Zankl
H. Han	E. Marshall	
J.T.M. Jansen	D.L. Miller	

Committee 2 critical reviewers

M. Andersson F. Bochud

Committee 3 critical reviewers

J.C. Ocampo-Ramos G. O'Reilly

Main Commission critical reviewers

D. Laurier W. Rühm

Editorial members

C.H. Clement (Scientific Secretary and *Annals of the ICRP* Editor-in-Chief)
Q. Fan (Assistant Scientific Secretary and *Annals of the ICRP* Associate Editor)

Committee 2 members during preparation of this publication

(2017–2021)

J.D. Harrison (Chair)	D. Jokisch	T. Sato
F. Paquet (Vice-Chair)	C.H. Kim	T. Smith
W.E. Bolch (Secretary)	R. Leggett	A. Ulanowski
V. Berkovski	J. Li	F. Wissmann
E. Blanchardon	M.A. Lopez	
A. Giussani	N. Petoussi-Henss	

(2021–2025)

F. Bochud (Chair)	A. Giussani	J. Li
F. Paquet (Vice-Chair)	D. Jokisch	N. Petoussi-Henss
M.A. Lopez (Secretary)	C.H. Kim	T. Sato
M. Andersson	M.S. Kulkarni	T. Smith
V. Berkovskyy	S. Lamart	A. Ulanowski
D. de Souza Santos	C. Lee	Y.S. Yeom

(2025–2029)

F. Bochud (Chair)	D. de Souza Santos	L. Liu
F. Paquet (Vice-Chair)	J. Eakins	T. Sato
M.A. Lopez (Secretary)	A. Giussani	T. Smith
S. Anand	D. Jokisch	A. Sokolova
M. Andersson	S. Lamart	F. Vanhavere
V. Berkovskyy	C. Lee	Y.S. Yeom

Committee 2 emeritus member

K. Eckerman

Committee 3 members during preparation of this publication

(2017–2021)

K. Applegate (Chair)	S. Demeter	C. Ruebe
C.J. Martin (Vice-Chair)	M. Hosono	W. Small
M. Rehani (Secretary)	K. Kang	D.G. Sutton
J. Alsuwaidi	R. Loose	L. Van Bladel
M. Bourguignon	J. Marti-Climent	
M.C. Cantone	Y. Niu	

(2021–2025)

K. Applegate (Chair)	A. Isambert	C. Ruebe
C.J. Martin (Vice-Chair)	M. Kortesniemi	W. Small
D.G. Sutton (Secretary)	A. Magistrelli	Å. Søvik
M.C. Cantone	M. Mahesh	I. Thierry-Chef
J. Damilakis	J. Marti-Climent	I. Williams
M. Hosono	J.C. Paeng	W. Zhuo

(2025–2029)

D.G. Sutton (Chair)	M. Mahesh	J.C. Paeng
A. Magistrelli (Vice-Chair)	L.G. Marcu	G. Pina
I. Thierry-Chef (Secretary)	L.N Mazzoni	W. Small
J. Damilakis	N. Noramaliza	J. Vassileva
Y. Inoue	J.C. Ocampo-Ramos	I. Williams
M. Kortesniemi	G. O'Reilly	W. Zhuo

Committee 3 emeritus members

S. Mattsson	M.M. Rehani	M. Rosenstein

Main Commission members at the time of approval of this publication

Chair: W. Rühm, *Germany*
Vice-Chair: S. Bouffler, *UK*
Scientific Secretary and CEO: C.H. Clement, *Canada*; sci.sec@icrp.org*

N. Ban, *Japan*	N. Martinez, *USA*	**Emeritus members**
F. Bochud, *Switzerland*	T. Schneider, *France*	C. Cousins, *UK*
K.W. Cho, *Korea*	D. Sutton, *UK*	J. Lochard, *France*
E. Gallego, *Spain*	A. Wojcik, *Sweden*	F.A. Mettler Jr, *USA*
M. Hosono, *Japan*		R.J. Pentreath, *UK*
D. Laurier, *France*		R.J. Preston, *USA*
S. Liu, *China*		C. Streffer, *Germany*
		E. Vañó, *Spain*

*Although formally not a Main Commission member since 1988, the Scientific Secretary is an integral part of the Main Commission.

Finally, thank you very much to all organisations and individuals who took the time to provide comments on the draft of this publication during the consultation process.